RICE UNIVERSITY

High-resolution imaging for cancer detection with a fiber bundle microendoscope

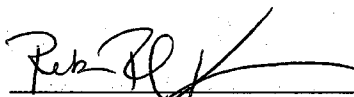By

Timothy J. Muldoon

A THESIS SUBMITTED
IN PARTIAL FULFILLMENT OF THE
REQUIREMENTS FOR THE DEGREE
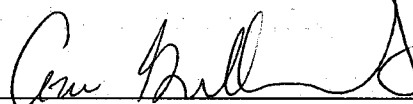
Doctor of Philosophy

APPROVED, THESIS COMMITTEE:

Rebecca Richards-Kortum, Stanley C. Moore
Professor, Department of Bioengineering
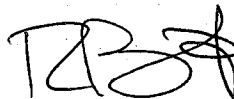
Rebekah A. Drezek, Stanley C. Moore Assistant
Professor, Department of Bioengineering

Ann M. Gillenwater, Associate Professor,
The University of Texas M. D. Anderson Cancer
Center

Richard G. Baraniuk, Victor E. Cameron
Professor, Department of Electrical and Computer
Engineering

HOUSTON, TEXAS
May, 2009

UMI Number: 3362370

INFORMATION TO USERS

The quality of this reproduction is dependent upon the quality of the copy
submitted.   Broken or indistinct print, colored or poor quality illustrations
and photographs, print bleed-through, substandard margins, and improper
alignment can adversely affect reproduction.
In the unlikely event that the author did not send a complete manuscript
and there are missing pages, these will be noted.   Also, if unauthorized
copyright material had to be removed, a note will indicate the deletion.

UMI®

Abstract

High-resolution imaging for cancer detection with a fiber bundle microendoscope

By

Timothy J. Muldoon

Dysplasia and cancer of epithelial tissues, including the oral cavity and esophagus, typically have much higher survival rates if diagnosed at an early stage. Unfortunately, the clinical appearance of lesions in these tissues can be highly variable. To achieve a definitive diagnosis of a suspected lesion at these sites, an excisional biopsy must be examined at high-resolution. These procedures can be costly and time-consuming, and in the case of Barrett's esophagus, surveillance biopsy strategies may not be entirely effective. Optical imaging modalities have the potential to yield qualitative and quantitative high-resolution data at low cost, enabling clinicians to improve early detection rate.

This dissertation presents a low-cost high-resolution microendoscopy system based on a fiber optic bundle image guide. In combination with a topical fluorescent dye, the fiber bundle can be placed into contact with the tissue to be observed. A high-resolution image is then projected onto a CCD camera and stored on a PC. A pilot study was performed on both resected esophageal tissue containing intestinal metaplasia (a condition known as Barrett's esophagus, which can transform to esophageal adenocarcinoma) and resected oral tissue following surgical removal of cancer. Qualitative image analysis demonstrated similar features were visible in both

microendoscope images and standard histology images, and quantitative image processing and analysis yielded an objective classification algorithm.

The classification algorithm was developed to discriminate between neoplastic and non-neoplastic imaging sites. The performance of this algorithm was monitored by comparing the predicted results to the pathology diagnosis at each measurement site. In the oral cancer pilot study, the classifier achieved 85% sensitivity and 78% specificity with 141 independent measurement sites. In the Barrett's metaplasia pilot study, 87% sensitivity and 85% specificity were achieved with 128 independent measurement sites.

The work presented in this dissertation outlines the design, testing, and initial validation of the high-resolution microendoscope system. This microendoscope system has demonstrated potential utility over a wide range of modalities, including small animal imaging, molecular-specific imaging, *ex vivo* and ultimately *in vivo* imaging.

Acknowledgements

Table of Contents

List of Figures

List of Tables

Chapter 1: Introduction

1.1 Motivation

In the United States, cancer is second only to heart disease as the leading cause of death. There will be nearly 1.4 million estimated new cases of cancer diagnosed in 2006, and an estimated 560,000 deaths [1]. Certain types of cancer account for a disproportionately high number of these cases; breast cancer and prostate cancer account for about 30% of all new cancer diagnoses in women and men respectively. However, lung cancer remains the leading cause of cancer mortality.

Early detection of cancer has been shown to generally have a significant effect on survival and quality of life. If cancer can be discovered at an early stage, when the risk for metastasis is low, treatment is generally simpler to perform and with less morbidity, and survival is improved. In the case of oral cancers, early detection is key: 5-year survival for cancers diagnosed as localized to a single area is greater than 80%, while survival for oral cancer presenting with distant metastases at diagnosis falls to 25%. Esophageal follows a similar pattern, 5-year survival with local disease is 34%, falling to just 3% for distant disease. Other types of cancer display a similar trend (Table 1-1) [2].

While the need for early diagnosis is clear, there are often many other factors that can lead to a delay. Usually, the definitive diagnosis for a suspicious lesion is to remove all or part of it for examination by a highly trained pathologist following tissue processing. The biopsy procedure itself takes time, but its invasiveness may lead a patient or their physician to hesitate. Oral cancers, for example, may often appear as benign

lesions to an experienced clinician, and often a patient may not even present a problem to a physician until the cancer has reached an advanced stage. Barrett's metaplasia, a condition caused by chronic reflux and inflammation of the esophagus and characterized by replacement of normal squamous epithelium with glandular epithelium, is another condition where occult cancer may exist. Surveillance requires endoscopic inspection and biopsy of the affected region, usually undersampling the area. Malignant transformation to esophageal adenocarcinoma can occur in such patients even with routine standard-of-care inspection.

Cancer Site	Local	Regional	Distant
Breast	>90%	80%	25%
Oral	>80%	50%	25%
Prostate	~100%	>85%	30%
Esophagus	34%	17%	3%

Table 1-1: Stage at diagnosis and 5-year survival figures

1.2 Specific Aims

The overall focus of this project was to develop and evaluate a robust, portable imaging system capable of distinguishing between neoplastic and non-neoplastic lesions in a variety of epithelial tissues. The following specific aims detail how this project was accomplished

Specific Aim 1:

Develop and characterize a high-resolution microendoscope device, based on a fiber optic image guide. Confocal microscopy has been the gold standard for high-resolution imaging within turbid media, such as tissue, but large bulky optics and expensive electronics have limited its clinical use to tertiary care centers with extensive funding and infrastructure. A fiber optic image guide coupled to a simple fluorescence microscope using an LED as an excitation source was developed to address this issue. By placing the distal tip of the fiber optic image guide in direct contact with tissue, following the application of a fluorescent dye, high-resolution images of the upper surface of tissue were attained. This approach is useful clinically since the fiber optic probe can be extended to any accessible epithelial or lumenal surface in the body, including the oral cavity and esophagus. To characterize the device, a number of in vitro experiments were conducted, using non biologic and biologic models of increased complexity, culminating with resected human tissue specimens.

Specific Aim 2:

We evaluated the performance of the imaging system to discriminate neoplastic from non-neoplastic lesions in resected oral cancer specimens. In normal squamous tissue, cells are regularly spaced, with small nuclei and small nuclear-to-cytoplasmic ratios. In dysplasia and cancer, this architecture changes and becomes more irregular, with significantly larger nuclear-to-cytoplasmic ratios. This hallmark structural change

was visible with the microendoscope device. A pilot study was performed by imaging the epithelium of resected oral cancer specimens. A number of quantitative image features were calculated and used to construct an objective algorithm to classify regions within the resected tissue as neoplastic or non-neoplastic; these results were then compared to histopathology of the same site, and to subjective interpretations of the images by trained and untrained observers. To further explore the effectiveness of the device to detect oral lesions in a clinical setting, widefield images from a multispectral digital microscope were used to guide placement of the microendoscope, and quantitative features from both were combined in a synergistic classification algorithm.

Specific Aim 3:

We evaluated the performance of the imaging device to differentiate between Barrett's metaplasia and clinically significant disease, including Barrett's metaplasia with high grade dysplasia and esophageal adenocarcinoma. Glandular tissue is fundamentally different from the squamous lining of the oral cavity, oropharynx, and esophagus. High resolution imaging shows glandular structures which appear large, uniform and discrete in Barrett's metaplasia, with preservation of nuclear polarity along the base of the glands. High grade dysplasia or adenocarcinoma shows irregular, crowded glands with large nuclei, and loss of nuclear polarity. A pilot study was performed on biopsies and endoscopic mucosal resection specimens from patients undergoing endoscopic evaluation for esophageal neoplasia. We performed quantitative image analysis, as in Aim 2 above, and compared the results to subjective interpretations of the images by expert clinicians.

1.3 Chapter Summary

The following dissertation is organized as follows: Chapter 2 presents relevant background information and cites current literature on the topic. Chapter 3 presents an initial study on the high-resolution microendoscopy system, including in vitro imaging using molecular targeted contrast agents, as well as *ex vivo* imaging on resected human oral tissue. Chapter 4 reports a quantitative analysis of an imaging study that demonstrates the ability of the microendoscope to distinguish between neoplastic and non-neoplastic tissue in human oral squamous epithelium. To demonstrate the ability of the microendoscope system to be integrated with other, wide-field imaging systems, Chapter 5 presents a quantitative analysis of a study using both systems to detect neoplastic lesions in human oral mucosa. Chapter 6 presents a qualitative assessment of the microendoscope's ability to image intestinal metaplasia. Chapter 7 is a quantitative analysis of the system's capability to distinguish between neoplastic and non-neoplastic tissue in a setting of intestinal metaplasia. Chapter 8 summarizes and discusses the important findings and implications of this dissertation.

Chapter 2: Background

2.1 Oncogenesis and the Histology of Cancer

To fully understand how the miniaturized imaging system will work, a discussion on the fundamental changes that occur during the progression to cancer is warranted. Generally speaking, cancer is the result of a continuum of changes that affect the ability of cells to control their division. Typically, damage to genes that either control cell division (oncogenes) or prevent cells from progressing to mitosis when inappropriate (tumor suppressor genes) lead to the possibility of development of cancer [3]. As an individual ages, such mutations become more likely to accumulate in these susceptible locations, accounting for the observation that cancers typically strike the older segment of the population. However, there are certain inherited mutations that can lead to cancers early in life; fortunately, such disorders are relatively rare.

The hallmark of cancer is uncontrolled and unchecked cell replication. Due to abnormal amounts of DNA replication, nuclei of dysplastic cells can appear greatly enlarged, often comprising 90% of the cell's diameter. These nuclei often appear irregular and hyperchromatic due to of this abnormal DNA replication. Additionally, because of the high rate of mitosis, numerous dividing cells may be present in dysplastic tissues. As dysplastic cells divide more frequently, cells will appear crowded and push into locations where they do not normally reside. For example, in normal epithelial tissue, such as skin, there is a clear hierarchy of organization with a basal cell layer that divides to replenish cells above that are sloughed off. A dysplastic lesion in epithelial tissue can be graded based on what fraction of the epithelium has been replaced with the abnormal

cells. Higher grade lesions will involve progressively greater fractions of epithelium. If a lesion encompasses the entire epithelium but does not go beyond the basal layer of cells or past the basement membranes, this condition is termed carcinoma *in situ*. When abnormal cells can be seen to push beyond the basal cell layer and basal membrane and into the connective tissue beneath, malignant transformation is said to have taken place, and treatment for such a lesion will become significantly more aggressive. (Figure 2-1)
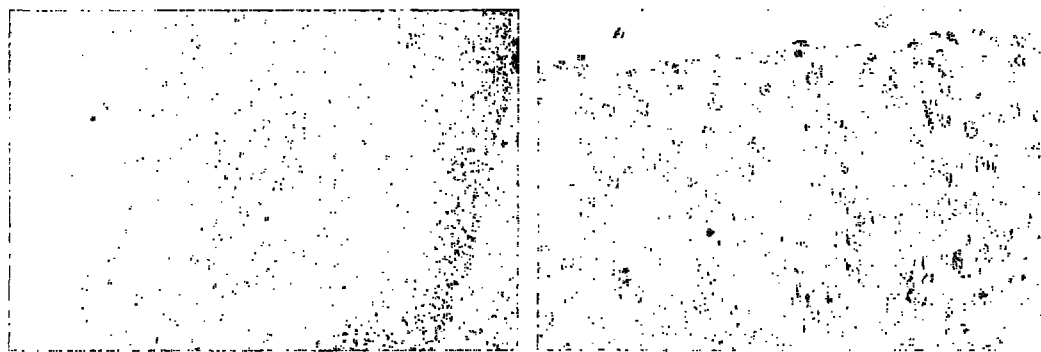
Figure 2-1: H&E Slides showing normal (left) and dysplastic (right) epithelium in the cervix (University of Washington Department of Pathology)

Analysis of the histology of removed tissues by a pathologist is the accepted standard of care for making a definitive diagnosis of cancer. The morphologic clues that can be used to aid the pathologist in making a diagnosis are described above. In recent years, however, additional tools have become available to improve the ability of the physician to make a diagnosis that are based on the molecular and metabolic features some types of cancers. Certain breast carcinomas have been shown to overexpress an extracellular tyrosine kinase receptor known as Her-2/neu. This receptor is involved in an estrogen signaling pathway and has been shown to be important in determining the

sensitivity of the cancer to a specific type of treatment [4]. Through a process known as immunohistochemisty (IHC), antibodies directed against this receptor can be introduced into the tissue, highlighting regions that express the abnormal receptor. Such molecular-based strategies allows for more specific diagnoses and highly directed treatments based on the expression of such markers. In addition to antibodies, aptamers- short sequences of RNA that have been shown to bind proteins- have been used recently as targeting agents directed against certain receptors [5].

In addition to the visible changes that occur in tissues due to dysplasia and cancer, there are numerous molecular and metabolic changes that occur as well. Mitotically active cells require a large amount of resources to be able to maintain such a high rate of replication; as a result, their oxygen and nutrient demands are very high. Bloodflow to fast-growing tumors is often increased, and frequently associated with abnormal angiogenesis. This increased blood flow and altered metabolic activity within cells can be detected using various spectroscopic techniques.

Despite the ability of these techniques to elucidate functional properties of tissues, there exists a need to evaluate tissues at higher resolution. Spectroscopic methods are unable to resolve tissues down to the cellular level and are therefore not able to differentiate between malignant neoplasias and certain other benign conditions- such as inflammation. Short of performing a surgical biopsy, several techniques exist that can examine tissue at high resolutions while being only minimally invasive. Needle biopsy is a common technique that can access virtually all parts of the body. A form of needle biopsy, fine needle aspiration (FNA) involves the insertion of a small hollow needle into a suspicious tissue, guided either by palpation, ultrasound, CT or other imaging

modalities. Suction is applied via negative pressure from a syringe at the opposite end of the needle to remove cells from the tissue undergoing the biopsy. These cells can be fixed immediately and stained to enable a fast diagnosis, and may also be saved for more specific studies to assess the specific nature of any tumor cells found, analogous to IHC as described above. While this procedure does not require general anesthesia and surgical complications are minimal, several passes may be required to attain enough cells for a proper diagnosis [6, 7]. Additionally, since cells removed via FNA are isolated from their surroundings, the architecture of the tissue cannot be visualized- an important aspect in making a pathologic diagnosis.

While techniques that examine the structure of tissues removed from the body will remain the gold standard of pathologic diagnosis for the foreseeable future, rising healthcare costs and limited insurance availability has necessitated the development of less invasive, rapid, and simple tests that still maintain high levels of sensitivity and specificity. The ability to clearly distinguish between normal tissue and abnormal tissue that has either become dysplastic and is at risk for malignant transformation or has already begun to metastasize remains the focus of these newer techniques.

2.2 Contrast Agents

Distinguishing dysplastic tissues from normal tissues through the use of an imaging modality is dependent upon a difference in contrast between the two tissue types. Fortunately, there are native contrast variations that can be visualized with minimal additional processing. As previously mentioned, increased DNA synthesis in the nuclei of dysplastic cells renders their nuclei large, hyperchromatic, and highly reflective [3]. This

increased reflectivity of dysplastic nuclei has been exploited in reflectance-based imaging techniques to highlight suspicious areas in tissues.

Cervical cancer screening has taken advantage of this concept for many years through the use of colposcopy. This imaging technique uses relatively low power microscopy to visualize the epithelium of the cervix. While a dysplastic lesion may not always be readily apparent, a weak solution of acetic acid is commonly applied, which enhances the contrast between normal and abnormal epithelium, a process known as acetowhitening. The mechanism of this reversible process is not well understood, but likely involves the clumping of chromatin, which in turn further enhances the reflectivity of nuclei by increasing the refractive index mismatch between the nuclei and cytoplasm. This leads to an increase in backscattered light from the tissue [8]. This effect causes dysplastic tissue, with its greater chromatin content, to reflect more light than its surroundings, improving the chances that a clinician will be able to observe the lesion and take the appropriate steps to secure an accurate diagnosis.

In addition to acetic acid, other cancer-specific contrast agents have undergone clinical study. One such compound is toluidine blue, a metachromatic dye that can easily be applied to epithelial tissues [9-19]. It has been theorized that this dye binds to negatively-charged chromatin in the nuclei of cells, thereby preferentially staining the nuclei of cells that have become dysplastic. The result is not dissimilar from what is seen with the acetowhitening effect: dysplastic or malignant lesions stand out from the background of normal epithelium, alerting a clinician that further study is required. A visual inspection of the oral cavity using Toluidine blue takes only a few minutes and utilizes reagents that are readily available and inexpensive. Other non-targeted dyes, such

as cresyl violet and rose bengal, has also shown promise as inexpensive markers that may be selective for dysplastic and cancerous tissues. Both of these have the added benefit of being fluorescent, simplifying the design of imaging systems intended to work with these dyes [20-24].

While these techniques are inexpensive and allow for rapid screening, their specificities are not sufficient enough to entirely replace biopsies. Toluidine blue, for example, has been shown to have a high false-positive rate as well [12-15]. These methodologies still need to be able to demonstrate a high degree of sensitivity and specificity. With the advent of molecular targeting strategies, it is possible to achieve acceptable levels of specificities in a number of diagnostic strategies.

Immunohistochemistry (IHC), as discussed previously, has been shown to target with a high degree of specificity abnormal cells that express certain proteins. These proteins can be isolated and antibodies produced that are specific only to these molecules. Examples include cell membrane localized receptors, secretory products like matrix metalloproteinases, abnormal cell signaling proteins, and a host of other classes of intracellular and extracellular proteins [25]. With the use of antibodies, diagnostic tests can be tailor-made to certain types of cancers that express these specific molecules. For diagnostic tests that rely on imaging modalities, the ability to link these highly specific antibodies to markers that enhance the contrast of dysplastic regions is desirable. These markers can be either highly reflective or absorbing for reflectance-based imaging strategies or fluorescent for fluorescent imaging modalities. Gold nanoparticles have shown much promise in reflectance imaging, as they are easily linked to antibodies or

other targeting molecules and exhibit desirable reflectance properties under the appropriate conditions [26].

Fluorescent imaging techniques hold much promise in maximally increasing the contrast between normal and abnormal tissues [27-30]. Fluorescent emission light is easily filtered from background excitation light, resulting in a high signal-to-background ratio when imaging in the proper conditions. Proflavine is an acridine-derived dye that has been postulated to bind to DNA in a reversible and non-covalent manner by intercalating between base pairs. Proflavine and other acridine-derived compounds exhibit anti-bacterial properties as a result of this DNA-binding mechanism, which also makes it well-suited as a nuclear fluorescent contrast agent. This nuclear staining pattern is very useful in cancer imaging applications since it allows for visualization of the overall cellular architecture, nuclear-to-cytoplasmic ratios, and other important metrics with minimal sample preparation or incubation time. Acriflavine hydrochloride is a compound containing both proflavine and euflavine, and has been used in a number of GI imaging studies [31, 32].

Recently, much work has been accomplished in the field of semiconductor nanocrystals, or quantum dots. These are fluorescent crystals that have several highly advantageous properties for biological imaging: a broad excitation profile, a narrow and tunable emission profile, limited photobleaching, and they are able to be passivated and functionalized to accept targeting antibodies on their surfaces. Quantum dots also exhibit a high quantum efficiency and a large Stokes shift, meaning that relatively little excitation light would be required to generate a signal, and this excitation light is easily filtered from the emitted light. Quantum dots and quantum dot-antibody conjugates are of

an ideal size for labeling tissues – usually between 2 to 10 nm [33]. These small sizes allow for the particles to pass through tissues and contact cell membranes, and can even be used to label intracellular targets [34]. Quantum dots have been used extensively in recent years to labels cultures of tumor cells *in vitro* as well in small animal models for cancer imaging related studies [35-39].

Targeting of quantum dot fluorescent markers with the aid of antibodies, aptamers, or other means would allow clinicians to monitor the expression levels of extracellular receptors like Her-2 and EGFR (epidermal growth factor receptor). The newly developed drugs Trastuzumab and Cetuximab block Her-2 and EGFR receptors and have been shown to be beneficial in breast cancers that express those receptors [4, 38, 40]. By directly visualizing these receptors over the course of treatment, it may be possible to track the progression and response of cancers to treatment.

2.3 Imaging Modalities

With recent advances in computing and optical technologies, it has become feasible to develop systems specifically designed to detect neoplasias by imaging tissues in a minimally invasive fashion. Such techniques do not require the removal of tissue from the body; rather, a small optical device is held in direct contact with very close to the tissues to be imaged. Such a procedure can be performed without any of the associated costs or discomforts to the patient a traditional biopsy would present.

Standard microscopy does not work well on *in vivo* tissues because of the inherent turbidity present. Since tissue is highly light scattering, light from outside the focal plane of interest will be present in the image plane of any microscope device. With standard

histopathology, tissue is sliced to form an extremely thin film, whereby essentially all of the material to be observed can be effectively focused. For imaging in live tissues, a technique known as optical sectioning has been shown to provide detailed structural data without needing to physically section tissues.

Confocal microscopy has been used for a number of years for *in vitro* applications, but has recently been shown to be useful for the imaging of *ex vivo* biopsies and *in vivo* tissues[41-43]. A confocal microscope works by focusing the illumination on a small point within the plane of interest. The returning light, which may be either reflected light or fluorescent light, is then focused through a small pinhole at the conjugate image plane. A photodetector placed just behind this pinhole serves to collect this incident light. Light that returns from outside the focal plane of interest is then rejected by the outside of the pinhole, thereby reducing the out-of-focus scattered light that may otherwise be collected. To create a full image, the illumination is scanned across the entire desired X-Y plane of the frame. The final image lacks the color of a histopathology slide, and is dependent upon refractive-index mismatching (in the case of reflectance imaging) to elucidate nuclei from cytoplasm or other structures.

Despite the advantages of confocal imaging, there are significant drawbacks inherent in its design that limits the potential applications. Since illumination must be directed into the tissues and recollected, the penetration depth of confocal microscopy is limited by how deeply the light can pass into tissues. While longer wavelengths of light tend to scatter less and penetrate more deeply into tissues, even near-infrared (NIR) systems can only image to a depth of about 1000 microns effectively[41]. Additionally, while miniaturization of confocal systems in recent years has created progressively

smaller instrumentation, including a confocal endoscope, the optical and mechanical elements of these systems have generally limited the usefulness of this technique to easily accessible regions of the body[32, 44-50].

One technique to overcome these limitations of high-resolution confocal imaging is to deliver the light into the tissue at the site where imaging is to take place. This clearly requires significant miniaturization of optics to accomplish. Through the use of optical fibers, which have been highly developed through the telecommunications and other industries, we are now able to build small, flexible optical devices capable of such tasks. Optical fibers consist of a dielectric core material and a dielectric cladding, which has a slightly lower refractive index. Light then propagates through the fiber through total internal reflection, acting like a light guide[51-55]. For short lengths of these fibers and at visible wavelengths, the amount of signal that is lost through these fibers is minimal[56, 57].

Optical fibers can be bundled together in an array of parallel fibers. This fiber bundle is referred to as an image guide. These image guide bundles are able to transfer a pixellated image from one face of the bundle to the other since each individual pixel element (fiber) is organized and parallel to each other[58]. This type of fiber bundle can be used for biological microscopy applications, since any tissue that is placed upon the distal surface of the bundle will yield an image on the proximal side that can be magnified through the use of more conventional optics. Tissues that are in immediate contact with the fibers at the end of the bundle will be "imaged" onto the other side, since the focal points for each fiber essentially occurs at the fibers' ends[59, 60]. This image can then be focused onto a CCD or other detector for post-processing. The resulting

image consists of the same number of usable pixels as the bundle has individual fibers; therefore, the physical properties of the image guide bundle itself is a major determinant of the performance of the overall system. Clearly, smaller individual fibers in the bundle will yield a higher-resolution image, while a larger diameter image guide will yield a larger field of view. The optics used to magnify the proximal bundle face determines the overall magnification of the system, but this magnification will be limited by the size of the individual fibers in the bundle.

Fiber bundle image guides overcome the limitations of standard confocal imaging by delivering the light and the optics directly to the tissues that are to be imaged. Illumination of the desired tissue can be achieved by passing excitation light directly through the same image guide that receives the image. Fluorescence excitation light can easily be filtered out before the light reaches the detector with a long pass filter. Reflected light imaging requires the removal of the specular reflection from both the proximal and distal ends of the fiber bundle. Using polarized light at the source and an appropriate beam splitter, it is possible to reduce the reflection from the proximal surface of the image guide. Polishing the distal end of the fiber bundle at such an angle that the reflection will be outside the numerical aperture of the fibers reduces the reflection from the distal tip of the fiber bundle. This reduces the overall undesirable background present in the final image.

Fiber optic image guides can be manufactured to extremely small diameters and offer a means to potentially image deep tissues within the body not otherwise easily accessible. Image guides less than approximately half a millimeter (500 microns) are easily passed through the lumen of relatively small 16 to 18 gauge needles, and could

therefore be placed directly into contact with masses or lesions that cannot be interrogated with standard confocal microscopic techniques. Additionally, since the illumination light will pass through the same image guide bundle, there is no concern about the limited transport depth of light in tissue.

Such miniaturized fiber optic bundle microscope systems are ideally suited for oncologic imaging applications. Fine needle aspiration (FNA) is widely performed as a simple outpatient procedure today in order to remove cells from suspicious masses[6, 7]. Two of the most common forms of cancer, breast and prostate, occur at sites that are relatively accessible to a needle biopsy probe, and therefore accessible to an image guide microscope system. An image guide could easily provide on-the-spot histologic information about such a mass with no more pain or discomfort to the patient than an FNA. However, since cells can be viewed in the context of their surroundings- unlike FNA, which removes individual cells at random, image guide microscopy may provide a pathologist with additional useful information. Furthermore, there would be no need to process and fix the cellular material, potentially reducing per-patient operating costs.

2.4 Development and Characterization of an Image Guide Microscope

This section will illustrate the design and performance of the first generation fiber bundle image guide-based microscope system. In order to design such a system, it is necessary to review the desired applications of the device as well as the desired performance characteristics. Since this image guide system is to be used to image tissues that are not necessarily superficial, it is important to determine a means of delivering the distal end of the image guide to the tissue in question. It was determined that a single

hollow 16 to 18 gauge needle could be inserted into the tissues and used as a conduit through which a small fiber bundle image guide could be passed. The lumens of these hollow needles are approximately 500 microns to 1 millimeter in size, placing an upper limit on the outer diameter of the fiber bundle in that range. Also, in order to achieve sufficiently useful resolution, it is important to be able to resolve individual cells; thus, this places a minimum lateral resolution limit of about 5 to10 microns for the microscope system. Since this system is intended to be a low cost / high volume screening tool, selection of the illumination source is critical. Light emitting diodes (LEDs) are currently being produced that have desirable spectral characteristics (small bandwidth, down to 20 nm FWHM) and illumination intensity (hundreds of milliwatts) and cost only dollars per unit. Their ability to function for thousands of hours and their inexpensive replacement costs makes LED's ideally suited for this application. Finally, a CCD camera with extremely high sensitivity would be used to detect the rather weak fluorescent emission light returning from the fiber bundle. It was decided that the ability to integrate frames was a characteristic necessary to achieve the needed sensitivity in this application, although long exposure times would also be acceptable. However, CCD devices that can attain long exposure times require very low-noise circuitry, driving up the costs.

The remainder of the optical train is very similar to that of a standard light microscope mounted on its side. Collimated light exiting the objective lens must be focused onto the plane of the CCD camera. This is accomplished through the use of a "tube" lens, of which the focal length is very important. (Figure 2-2) The focal length of this tube lens is directly proportional to the magnification of the optical setup, which is given by the simple relation: $M = f_{tube\ lens} / f_{objective}$. The focal length of the objective

lens is given by the manufacturer to be 18 millimeters, therefore an appropriate tube lens

focal length was selected to be 250 millimeters to give an overall magnification of about

14X, sufficient to produce an acceptable image scale for the CCD detector. This

theoretical value was confirmed experimentally by measuring the image size of US Air

Force (USAF) resolution target lines that were projected onto the CCD detector. Since

the size of each pixel in the CCD array is known, counting pixels allowed the projected

image size to be evaluated, and confirmed that the system magnification was

approximately 14X.

A novel technique used in this device is the implementation of an LED as its

primary light source. Excitation of quantum dot and other fluorophores was stated as a

a.   b.
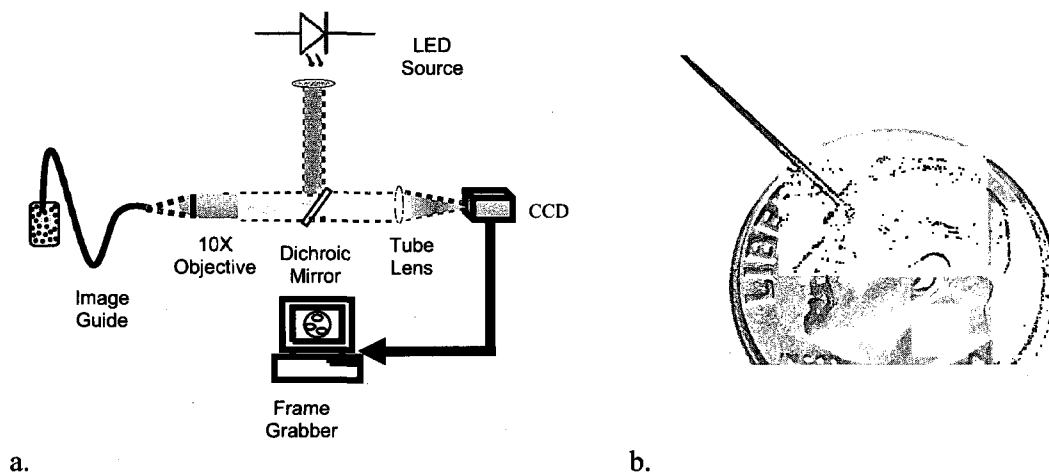
Figure 2-2: Schematic of fiber bundle microscope system (a) and illustration of relative size of fiber optic image guide (b).

major design goal. These quantum dots have desirable absorption cross sections such that

illumination over a broad wavelength range in the blue region of the spectrum would be

sufficient, eliminating the need for a laser or arc lamp, which are the standard methods for excitation of many fluorescent molecules.

The image guide microscope can be used for both fluorescence and reflectance image with minor changes in the optical setup. Fluorescence imaging requires a dichroic mirror in the objective lens pathway and both an exciation and emission edge-pass filter placed in front of the LED and the CCD respectively. This setup effectively illuminates the proximal face of the image guide and eliminates any remaining excitation light before entering the CCD. For reflectance imaging, the edge-pass filters are removed and the dichroic mirror is replaced with a polarizing beam splitter (PBS) cube. This PBS cube splits the incoming unpolarized light to s- and p-polarizations and sends only one type of polarization to the proximal face of the image guide. Specular reflection from this surface will remain polarized in the direction that is unfavorable to be passed through to the camera. In addition, the distal end of the fiber bundle is polished at a 10-degree angle, which reduces the amount of reflected light from this surface by directing it outside the acceptance cone of the individual fibers in the image guide. This acceptance cone is defined by the numerical aperture (NA) of the fibers given in the image guide specifications (NA ~ 0.35).

An alternative means for reflectance imaging has been explored which separates the illumination channel entirely from the imaging arm. In this setup, the LED is used to illuminate two single, 200 micron diameter optical fibers, which are then localized in flanking positions around the image guide. Light then enters the tissue from the side of the image guide and a portion will be backscattered into the acceptance cone of these imaging fibers. Cells on the surface of an epithelium that have been labeled with

absorbing dye or other materials will then appear to be backlit by this backscattered light, forming an image of dark cells in a light background. This application effectively eliminates any unwanted specular reflection from the system.

Chapter 3: Subcellular-resolution molecular imaging within living tissue by fiber microendoscopy[1]

3.1 Abstract

Conventional histopathology involves sampling, sectioning and staining of tissue specimens prior to microscopic evaluation, and provides diagnostic information at a single location and point in time. *In vivo* microscopy and molecular-targeted optical labeling are two rapidly developing fields, which together have the potential to provide anatomical and functional indications of disease by staining and imaging tissue *in situ*. To address the need for high-resolution imaging instrumentation, we have developed a compact, robust, and inexpensive fiber-optic microendoscopy system based around wide-field LED illumination, a flexible 1 mm diameter fiber-optic bundle, and a color CCD camera. We demonstrate the sub-cellular resolution imaging capabilities of the system through a series of experiments, beginning with simultaneous imaging of three different cancer cell lines in culture, each targeted with a distinct fluorescent label. We used the narrow diameter probe to access subcutaneous tumors in an *in vivo* murine model, allowing direct comparison of microendoscopy images with macroscopic images and histopathology. A surgically resected tissue specimen from the human oral cavity was imaged across the clinical margin, demonstrating qualitative and quantitative distinction between normal and cancerous tissue based on sub-cellular image features. Finally, the fiber-optic microendoscope was used on topically-stained normal human oral mucosa

---

in vivo, resolving epithelial cell nuclei and membranes in real-time fluorescence images. Our results demonstrate that this imaging system can potentially complement conventional diagnostic techniques, and support efforts to translate emerging molecular-diagnostic and therapeutic agents into clinical use.

3.2 Introduction

In many clinical situations, visualization of cellular morphology and architecture is mandatory, requiring an excisional biopsy or fine needle aspiration to obtain tissue or cells for histopathology. Such procedures are invasive, sometimes dangerous, expensive, and the results are not immediately available. This clinical need has motivated the development of techniques for imaging tissue *in situ* with cellular resolution, aimed at complementing the pathologist's expertise though biopsy guidance and monitoring of disease progression and treatment. By analogy with chemical staining in histopathology, contrast between tissue components can be obtained *in situ* through topical or intravenous delivery of fluorescent agents. While non-specific dyes have been widely used to generate optical signals for *in vivo* imaging, an expanding array of targeted fluorescent probes are emerging that can provide indicators of disease at the cellular and molecular levels [35, 61-63]. This ability to detect and monitor the presence and activity of disease biomarkers is expected to have considerable impact in fundamental biomedical research, and ultimately on the clinical management and care of patients [64, 65]. As research in the molecular imaging field proceeds through studies in cell culture, animal models, and pre-clinical trials, robust, versatile, high-resolution optical imaging instrumentation is

essential at each stage, and ultimately to accompany molecular imaging into the clinical setting.

Flexible, narrow-diameter optical fibers are well-suited for performing microscopic imaging at sites within the human body [29], and several researchers initially demonstrated the feasibility of using a length of single-mode fiber as a conduit through which confocal microscopy could be performed [66-68]. Such configurations using only a single optical fiber require a means of scanning the emerging optical beam across the specimen in order to build up an image, which to date, still represents the overall limiting factor in system miniaturization. Scanning mechanisms based on miniature mirrors [69-71], piezoelectric actuators [72], spectral encoding [73] and electromagnetic vibration [74] have all been demonstrated, with the latter technique used to construct a scan head integrated into a standard 1.2 cm diameter clinical endoscope, providing access to hollow internal cavities including the gastrointestinal tract and colon [75, 76].

A related approach that eliminates the requirement for a scanning mechanism at the distal (sample) end of a fiber, involves the use of a coherent fiber bundle, comprising thousands of individual optical fibers within a single element of sub-millimeter diameter [59, 77]. The use of a coherent bundle enables the scanning mechanism to be located outside the body at the proximal end of the fiber, with the scan pattern faithfully reproduced at the distal end due to the ordered arrangement of individual fibers. The fiber bundle approach has been used for both reflectance [77, 78] and fluorescence [28, 59, 79, 80] confocal imaging, in both two-dimensional point scanning and one-dimensional line scanning variations [81, 82]. The primary drawback of the fiber bundle approach is the

appearance of the bundle structure superimposed on each image, although this artifact can be reduced by image processing methods [28, 83].

In this article, we present a high-resolution fiber-optic fluorescence imaging system for visualizing sub-cellular detail in living tissue. Based on wide-field imaging through a coherent fiber bundle, all scanning requirements are eliminated, and through the use of LED illumination and CCD imaging, we have developed an inexpensive system that is both simple to implement and robust in use. We demonstrate the capabilities of the system through a series of experimental studies in biological systems, leading to *in vivo* human imaging. First, we performed multiplexed imaging of a cell-culture model containing three cancer cell lines, discriminating between cell type based on the different fluorescent markers targeted to each. We then imaged a murine tumor model *in vivo*, allowing comparison with features evident in standard macroscopic imaging and histopathology sections. Next, a surgically-resected cancerous human tissue specimen was imaged, enabling real-time visualization and quantification of cellular features across the margin between diseased and healthy tissue. Finally, the system was used in a healthy human subject *in vivo*, demonstrating its ability to acquire stable images with sub-cellular resolution, non-invasively and in real-time. Our results indicate that this type of simple and inexpensive fiber-optic imaging platform can extract qualitative and quantitative information with high-resolution from fluorescently labeled cells and tissues. These capabilities can potentially be used in conjunction with existing and emerging molecular-targeted fluorescent probes, in areas ranging from cell culture studies to clinical imaging in human subjects.

3.3 Materials and methods

3.3.1 Fiber-optic microendoscopy system

The primary components of the imaging system are a light source, a fiber-optic bundle, a microscope objective lens, and a CCD camera (Figure 3-1). The LED light source (Luxeon) produces an optical spectrum centered at 455 nm (20 nm FWHM), and costs less than $5 per unit. A collimator directs light from the LED to the back aperture of a 10x / 0.25 NA infinity-corrected objective lens (Olympus), via a 475 nm cut-off dichroic mirror (Chroma Technology Corp.). Excitation light illuminating the proximal end of a flexible fiber-optic bundle (Sumitomo, IGN-08/30) is transferred coherently to the distal end. The distal tip of the bundle (Figure 3-1) is placed in direct contact with the sample, delivering 1 mW excitation power. Fluorescence emission from the sample is collected by the bundle, transmitted through the dichroic mirror and imaged onto a CCD camera by a tube lens with magnification factor, M. This factor is chosen to balance the conflicting requirements of sampling individual fibers with a sufficient number of pixels at the CCD, whilst confining the magnified image of the bundle to the area of the CCD array. Since the physical size of the bundle determines the field-of-view, the maximum achievable FOV is related to the CCD and bundle properties according to Eq. (1), where w_{CCD} is the CCD size, w_p the pixel size, ϕ_c the fiber core diameter, and n the desired number of samples (pixels) per fiber:

$$FOV_{max} = \frac{w_{CCD}}{w_p} \frac{\phi_c}{n} \qquad (1)$$

Two different CCD cameras were evaluated in this work; the results shown in Figures 3-4 and 3-5(a) were acquired by a scientific-grade color CCD camera (Retiga

EXi, QImaging, Inc.), using IEEE 1394 (Firewire) output to directly send continuous image data to a computer. The results shown in Figures 3-2, 3-3, and 3-5(b) were acquired by a standard analog CCD camera (CV-S3200N, JAI, Inc.), with image acquisition card (National Instruments). Using Eq. (1), the maximum field-of-view at the Nyquist limit ($n = 2$) is 1416 μm and 539 μm for the Retiga and JAI cameras, respectively. Both cameras use a Bayer mask for color imaging and were digitized at 8-bit resolution. Relevant experimental parameters are summarized in Table 3-1.

	JAI	Retiga
Array size	6.6 x 4.8 mm	10.2 x 8.3 mm
Pixel size	8.4 x 9.8 μm	6.45 x 6.45 μm
Number of pixels	768 x 494	1392 x 1040
Relay magnification, M	7x	10x
Pixels per fiber at CCD	1.6	3.4
Dynamic range	50 dB	67 dB
Least significant bit at 8-bit A/D*	$1.2\sigma_{read}$	$8.8\sigma_{read}$

* Read noise, σ_{read}

Table 3-1: Experimental parameters of each CCD camera

The total cost of the fiber microendoscopy system was $2500 with the standard CCD camera, and $11,000 with the scientific-grade unit.
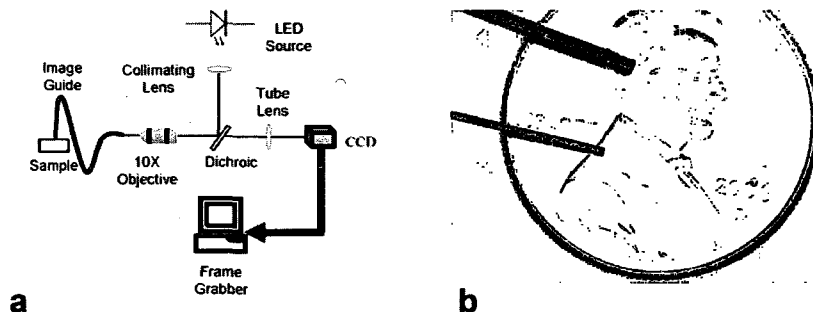
Figure 3-1: Fiber-optic microendoscopy system. (a) Schematic diagram. (b) Photograph of fiber-optic bundles on a US penny. Bundles 1 and 2 have outer diameters of 1.0 mm and 0.5 mm respectively.

3.3.2 3-D cell culture and labeling

Two tyrosine-kinase receptors shown to be overexpressed in epithelial cancers, Her-2 and EGFR, were selected as the antibody targets. Labeling of these extracellular receptors was accomplished using a biotin-antibody conjugate (Neomarkers) and a commercially-available quantum dot-strepatavidin conjugate (Invitrogen).Multiplexed labeling was performed using the two extracellular targets (Her-2 and EGFR) and a green nucleic-acid specific cell dye (SYTO 45, Invitrogen). EGFR was targeted with a red Qdot 655 / streptavidin conjugate, while Her-2 was labeled with a yellow Qdot 585 / streptavidin conjugate. Following labeling, equal numbers of each of these cell types were suspended in collagen. All three fluorophores have spectrally distinct emission

spectra but similar absorption spectra, permitting all to be excited with the LED's emission centered at 455 nm. Images of the tri-color fluorescent collagen construct were taking using a 500 nm long-pass filter (Thorlabs) for the green nuclear stain, a 20 nm FWHM bandpass filter centered at 585 nm for the Her-2 fluorophore, and a 20 nm FWHM bandpass filter centered at 655 nm for the EGFR fluorophore (Chroma Technology Corp.). These individual frames were then uniformly processed by enhancing contrast and applying a false color (ImageJ). Additionally, a fully-multiplexed imaging mode is achieved by using the camera's color imaging capability. A single 500 nm long-pass emission filter was used, with the CCD camera's Bayer mask used to distinguish between each fluorescent cell species.

3.3.3 Murine tumor model and macroscopic imaging

1483 cells (provided by Dr. P. G. Sacks, New York University College of Dentistry, New York, NY), derived from a human oropharyngeal squamous carcinoma, were injected into the subcutaneous tissue of athymic nude mice. The tumors were grown for approximately 2 to 3 weeks, until they were greater than 5 mm in size, in accordance with a protocol approved by the Institutional Animal Care and Use Committee at Rice University. To visualize the tumor at low resolution within the context of the whole animal, macroscopic imaging was performed using a small animal imaging system (CRI Maestro). To enhance visualization of the tumor in both whole animal imaging and during fiber microendoscopy, the tumor was directly injected with 0.05% acriflavine hydrochloride in PBS. Acriflavine is a non-DNA binding fluorescent molecule that associates with the negatively charged nucleus allowing for optimal visualization of

overall tissue architecture. Following a 20 minute incubation period, the skin of the animal was pierced with a 16-gauge needle, and the 1 mm diameter fiber-optic bundle inserted into the tumor. Images and video were acquired while the animal remained under anesthesia. On completion of the microendoscopy imaging, the tumor was removed and subject to routine histologic processing with H&E staining.

3.3.4 Surgical specimen acquisition and imaging

Through a study protocol approved by both the Rice University and University of Texas M.D. Anderson Institutional Review Boards and following informed consent by the patient, a surgical specimen containing an oral squamous carcinoma located in the buccal mucosa and retromolar trigone was obtained immediately after surgical resection. Acriflavine solution (0.05% in saline) was applied to the mucosa of the specimen, and imaging with the microendoscope followed immediately thereafter. The specimen was subsequently sent for routine histologic processing, which generated H&E stained sections from locations closely corresponding to those imaged with the fiber microendoscope.

3.4 Results

3.4.1 System characterization

The spatial resolution of the imaging system is governed by the size and spacing of individual fibers in the coherent bundle. In the system presented here, the fiber core size is 2.2 μm, with a center-to-center spacing of < 4 μm. An image of a standard

resolution target demonstrates the system's ability to resolve lines that are 4.4 μm in width (Figure 3-2(a)). The field-of-view simply corresponds to the active area of the fiber bundle, which is 350 μm in diameter with the fiber bundle used here and 750 μm in the remaining figures in the text.

a   b   c
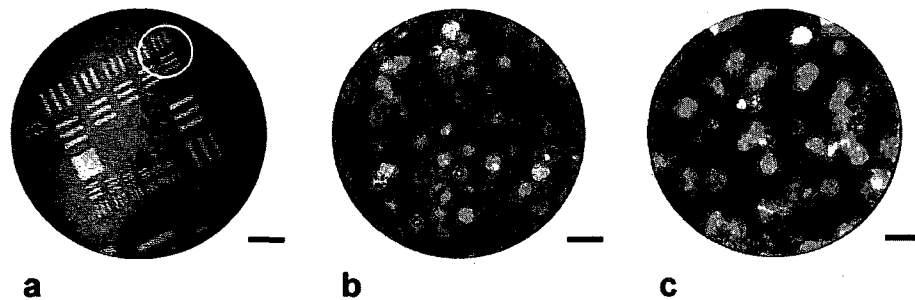
Figure 3-2: System resolution and multiplexed cell culture imaging. (a) Image of a standard US Air Force resolution target, demonstrating resolution of the 4.4 micron-wide bars in group 6, element 6 (circled). (b) False-color composite image of a 3-D collagen construct containing 1483 oral squamous cell carcinoma cells (red), SK-BR-3 breast cancer cells (green), and SiHa cervical cancer cells (blue), with each cell type stained with a spectrally-distinct fluorophore. (c) Single frame image of the same tissue construct acquired in real-time with a single long-pass emission filter. 1483 cells appear red, SK-BR-3 cells yellow, and SiHa cells appear light green. All scale bars represent 50 microns.

3.4.2 Multiplexed imaging

Histopathology typically involves the addition of different chemical stains to individual tissue sections, to generate contrast between tissue components or assess molecular activity under light microscopy. A fundamental goal of *in vivo* molecular imaging is to achieve analogous staining *in situ*, through the use of molecular-targeted fluorophores. The fiber microendoscope can image and distinguish between cells stained with spectrally-distinct fluorescent labels within a single sample. We demonstrated this ability in an *in vitro* system, consisting of three different cancer cell lines, each labeled with a different fluorophore and suspended in a three-dimensional collagen construct. All three fluorophores were excited by the same LED light source, and individual images were acquired sequentially with three separate emission filters. Following background subtraction, contrast enhancement and false coloring, a composite image was formed, with 1483 cells appearing red, SK-BR-3 cells green, and SiHa cells blue (Figure 3-2(b)). To distinguish different fluorescent labels simultaneously, the CCD camera's Bayer mask can be used, eliminating the need to exchange separate emission filters and providing real-time multiplexed imaging. This technique is subject to cross-talk due to spectral overlap between the three Bayer mask elements, but the effect can be minimized by use of fluorophores that are as spectrally distinct as possible. The peak wavelengths of the three fluorophores used in this experiment were isolated by at least 50 nm. A single image of the same triple-labeled cell construct was taken with a 500 nm long-pass emission filter (Figure 3-2(c)). The three cancer cell types can again be differentiated, this time based on correspondence between individual fluorescent emission spectra and

the spectral transmission curves for each channel (red, green, and blue) of the Bayer mask.

3.4.3 *In vivo* tumor imaging

Clinical diagnosis of suspected tumors requires collection of tissue samples for histopathology, an invasive process which must be iteratively repeated when multiple suspicious lesions are present or margin determination is required. Each sample provides information at only one location and at one point in time, leading to sampling error and the need for multiple biopsies at initial and follow-up clinical visits. The flexible, narrow-diameter fiber microendoscope can repeatedly access internal and sub-surface tissue sites in a minimally-invasive fashion. We imaged established subcutaneous tumor xenografts in athymic nude mice after fluorescence labeling, first with a macroscopic imaging system (CRI Maestro), and then with the fiber-optic microendoscope (Figure 3-3). Prior to imaging, the tumor was directly injected with acriflavine hydrochloride, a nuclear-associating green fluorescent stain originally used as a topical antiseptic [84], and since as a source of contrast in confocal microscopy [75, 76]. The tumor mass was clearly visible with the macroscopic imager (Figure 3-3(b)). The fiber microendoscope was then introduced into the tumor through the lumen of a 16-gauge needle. As the microendoscope was advanced through the tissue, cellular architecture and morphology could be visualized in real-time. Nuclei appear as discrete green dots, with continuous green fluorescent regions likely arising from acriflavine uptake in desmoplastic tissue containing fibroblasts within the tumor mass (Figure 3-3(c)). For direct comparison, an H&E stained histological section (Figure 3-3(d)) is shown alongside a fiber

microendoscope image at the same scale, indicating invasive moderately-differentiated squamous carcinoma cells (dark blue-stained) and reactive desmoplastic (fibrous) tissue from the host response (appearing pink-stained).
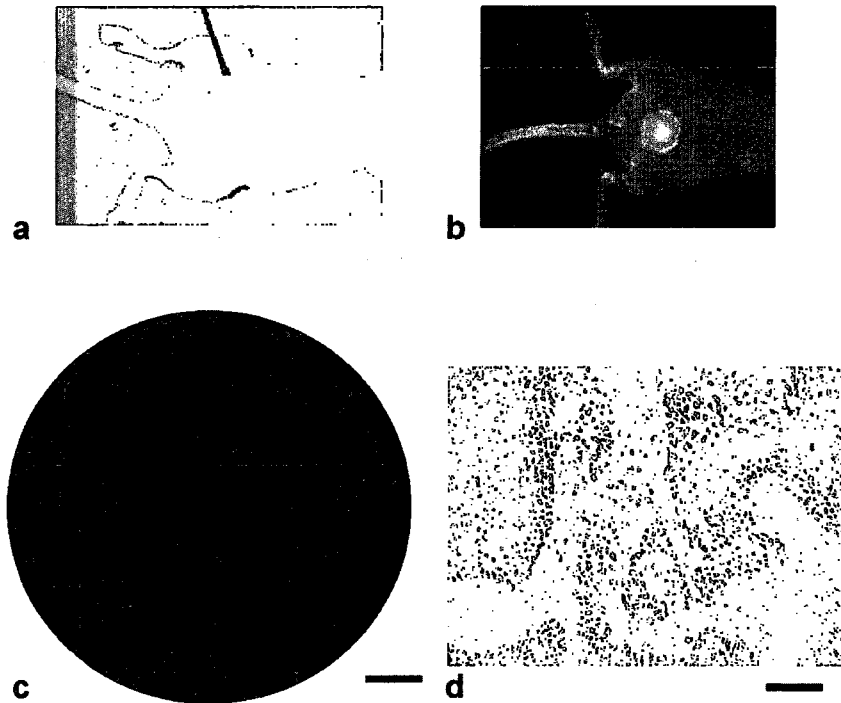
Figure 3-3: Murine tumor model imaging. (a) Photograph of an athymic nude mouse showing the fiber microendoscope and subcutaneous tumor. (b) Macroscopic fluorescence image (CRI Maestro) acquired following direct injection of fluorescent contrast agent at the tumor site. (c) Image acquired by the fiber microendoscope in the living mouse, as the fiber is advanced through the tumor within the lumen of a 16-gauge needle. Tumor cell nuclei appear as bright green dots, with connective tissue within the tumor mass. (d) Corresponding histology section following tumor excision. Scale bars represent 100 microns.

3.4.4 *Ex vivo* human specimen imaging

Histopathologic processing and inspection by an experienced pathologist remains

the gold-standard for diagnosis and classification of disease, but there are opportunities

for optical imaging to complement established practice in areas such as biopsy guidance

and surgical margin detection. In order to demonstrate the ability of the microendoscope

system to discriminate and quantify changes associated with cancer, the device was used

to image a surgical specimen containing an oral squamous carcinoma located in the

buccal mucosa and retromolar trigone. With the fiber microendoscope tip placed in

contact with the specimen at a clinically-normal region, bright, sparsely distributed nuclei

are visible (Figure 3-4(a)). In contrast, as the fiber probe was moved to the region

clinically-determined to contain the tumor (Figure 3-4(b)), nuclei qualitatively exhibited

the characteristic increase in density and disorganization associated with cancer [85].

Corresponding histopathology sections are also presented and were reviewed by a board-

certified pathologist (MDW). The histology in Figure 3-4(a) demonstrates normal

epithelium with some inflammation, while Figure 3-4(b) indicates the presence of

squamous carcinoma cells extending to the tissue surface. The sub-cellular features which

were qualitatively visualized in real-time using the fiber microendoscope were further

evaluated by quantitative determination of nuclear-to-cytoplasmic (N/C) ratio, a

recognized indicator of cancer and pre-cancer development. The images shown in Figure

3-4 were visually inspected, with nuclei outlined manually using image processing

software. Pixels in each nuclear region were then assigned a value of 1, with the

remainder of the image (corresponding to cytoplasmic area) assigned a value of zero,

producing binary images for each sample. Nuclear-to-cytoplasmic ratios were then calculated from the numbers of pixels in each group. Automated image processing techniques may allow for a more rapid and less labor-intensive means of isolating cell nuclei, but for this example, visual identification of nuclei was used to ensure identification of nuclei that were clustered, or in relatively low-contrast regions. The use of the scientific-grade camera, with its improved image contrast, greatly facilitated this process. Images acquired in the tumor region demonstrated a marked increase in N/C ratio compared to the clinically normal region (Figure 3-4(c)). The dashed line represents an N/C ratio of 0.08, a threshold value determined by Collier *et al.* for discrimination between normal and cervical intraepithelial neoplasia (CIN) 2/3 in cervical biopsy specimens, through the use of reflectance confocal techniques [85].
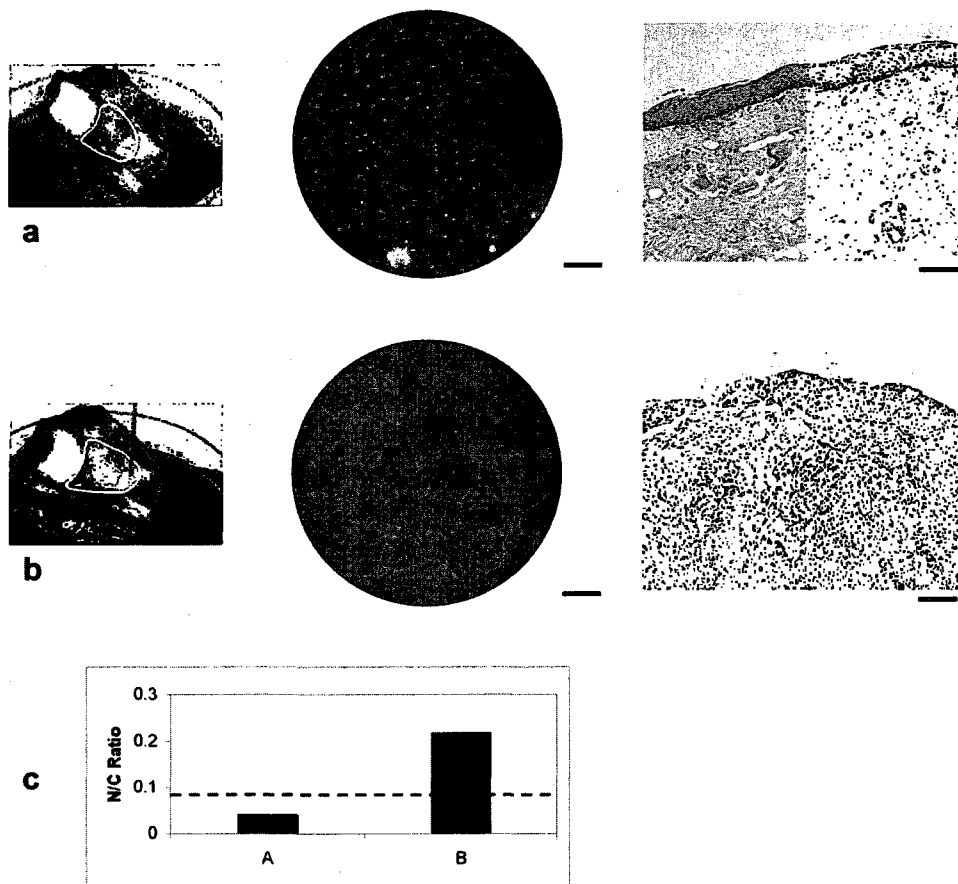
Figure 3-4: Surgical specimen imaging. (a) Normal epithelium. Left; photograph of fiber probe in contact with excised tumor tissue. Yellow border represents the clinically-abnormal region identified by the surgeon (AG). Center; microendoscopy image of tissue with probe at location indicated in photograph. Right; corresponding transverse histopathology section from the imaged region. (b) Tumor region. Microendoscopy image (center) and histology (right) demonstrate squamous carcinoma throughout the entire epithelium. Scale bars represent 100 μm. (c) Graph of calculated nuclear to cytoplasmic ratio for microendoscopy images in (a,b). The dashed line represents an N/C ratio of 0.08.

3.4.5 *In vivo* human subject imaging

A growing number of targeted optical contrast agents are gaining approval for human use, raising the prospect of combining molecular-specific fluorescent staining with fiber-optic imaging to perform an optical biopsy in living tissue. We used the fiber microendoscope system to image human tissue *in vivo* in accordance with a protocol approved by the Rice University Institutional Review Board. Following topical application of medical-grade acriflavine (0.05% in saline), the distal tip of the fiber-optic bundle was placed in contact with the normal oral mucosa of a human volunteer. Strong uptake of the fluorescent label is indicated in images by the bright appearance of nuclei and visibility of cell membranes (Figure 3-5(a)). While this image and those shown in Figure 3-4 were acquired with a scientific-grade CCD camera, we also demonstrated the ability of the system to obtain high-resolution images using a low-cost, standard CCD camera. An image of the same *in vivo* tissue is shown in Figure 3-5(b), with cell nuclei still apparent.
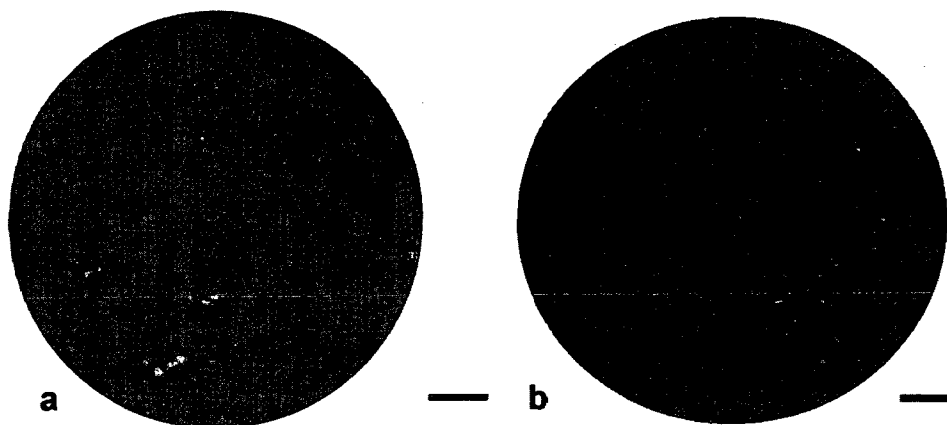
Figure 3-5: *In vivo* human tissue imaging. (a) Fiber microendoscopy imaging of normal human oral mucosa *in vivo*, following topical application of fluorescent acriflavine neutral (0.05% in saline). This image was acquired with a scientific-grade CCD camera. (b) Image of the same tissue acquired with a standard CCD camera. In both images, cell nuclei appear bright surrounded by dark cytoplasm. Scale bars represent 100 μm.

3.5 Discussion

As optical contrast agents capable of indicating the onset of disease at the molecular level transition to pre-clinical and clinical use, techniques for imaging tissue at the sub-cellular level *in vivo* become increasingly relevant. We have developed a fiber-optic microendoscopy system, based around a flexible, 1 mm diameter fiber bundle which can either be placed in direct contact with the site to be imaged, or introduced through a 16-gauge needle for insertion into tissue. The field-of-view and spatial resolution are limited by the physical properties of the fiber bundle; namely the diameter

and fiber-to-fiber spacing, which for the system presented here are 750 μm and < 4 μm

respectively. For a particular bundle, field-of-view and spatial resolution can be traded-

off against each other through the use of additional magnifying lens elements at the distal

tip [80, 86, 87]. This system uses a single LED for fluorescence excitation, and a color

CCD camera for image acquisition, enabling multiple fluorescent labels to be visualized

in real-time. The utility of imaging with multiple spectral channels was previously

demonstrated in fiber bundle confocal imaging of cells labeled with nuclear and

cytoplasm-specific fluorophores [80, 82]. Here, we used the CCD's built-in Bayer mask

to efficiently image three spectral channels simultaneously with a single camera.

Two cameras were evaluated in this study; a scientific-grade cooled CCD

(Retiga), and a standard analog CCD (JAI). Both cameras were shown to be capable of

sub-cellular resolution imaging, but the direct comparison shown in Figure 3-5 reveals

differences in image appearance that can be related to camera specifications and the

experimental configuration. Sampling at the tissue specimen is determined by the

physical spacing of individual fibers in the bundle for direct contact imaging, or the

demagnified spacing of these same fibers when an additional objective lens is used at the

distal tip. The image appearing at the proximal end of the bundle is then relayed to the

CCD camera with magnification factor M set by the objective – tube lens combination.

For a particular bundle, the number of camera pixels sampling each fiber depends on both

the CCD pixel size, and relay magnification, M. We summarized these spatial parameters

in Table 3-1. With the JAI camera, the image of each fiber in the bundle spans 1.6 pixels

at the CCD sensor, compared to 3.4 pixels per fiber with the Retiga device. So while

sampling at the specimen is identical for each camera, the spatial sampling frequency for

the intermediate image (at the proximal end of the bundle) is over a factor of two higher with the Retiga CCD and above the Nyquist requirement, resulting in image resolution limited by optical rather than sampling conditions. Intensity resolution is the second factor expected to influence image contrast. While both CCDs were digitized at 8-bit resolution, the higher dynamic range and lower noise figure for the scientific-grade camera results in the least significant bit corresponding to a level times 8.8 times higher than the read noise in the Retiga CCD, compared to only 1.2 times for the JAI camera.

Wide-field fluorescence imaging through a fiber bundle or "image conduit" has been reported previously [47, 50, 79], with the reduction in optical sectioning strength shown to result in increased collection of background light and reduced image contrast, in comparison with truly confocal techniques [79]. Preliminary tests using a planar fluorescent sample indicated that the fluorescent signal for our system is predominantly collected from a depth of some tens of microns, corresponding to a few cell layers of thickness. However, we have shown here that high-quality images with sub-cellular resolution can nevertheless be obtained with a system that is simple and relatively inexpensive to construct, and robust in operation. Two factors appear to be largely responsible for the high image quality. First, contact imaging inherently eliminates background light that would be generated between the sample surface and the object plane in confocal imaging, and second, use of highly specific, bright fluorophores enables the necessary contrast to be generated between cellular components.

3.6 Conclusion

We have presented a high-resolution, wide-field fluorescence imaging system based on LED illumination, CCD camera detection, and a 1 mm diameter, flexible fiber-optic bundle. The sub-cellular resolution color imaging capabilities were demonstrated in a series of experiments intended to highlight potential application areas in current clinical practice, and in future applications involving molecular-targeted optical contrast agents. The ability to obtain information from multiple tissue sites over an extended period of time may reduce the inherent uncertainties in point sampling associated with histopathology, and provide additional information on specific molecular expression and activity, biological processes, and an individual's response to treatment. The instrument retains several of the advantageous features of confocal microscopy, including fiber-optic delivery, real-time image acquisition, and color multiplexing capabilities. In addition, due to its relative simplicity, the instrument is compact, robust, and inexpensive, features which are increasingly valuable in both the research laboratory and clinical setting.

Chapter 4: Detection of oral squamous neoplasia with a high-resolution fiber optic microendoscope[2]

4.1 Abstract

Purpose: The development of oral neoplasia is associated with changes in epithelial cell morphology and architecture, which are usually documented by histologic assessment of mucosal biopsy. The goal of this study was to evaluate the ability of high-resolution optical microscopy to image and quantify the cellular and architectural features of oral neoplasia without the need for biopsy.

Experimental Design: A high-resolution microendoscope (HRME) was used to image intact, resected oral squamous carcinoma specimens following topical application of a fluorescent contrast agent. HRME images were reviewed and classified as non-neoplastic (normal squamous epithelium and mild dysplasia) or neoplastic (moderate dysplasia, severe dysplasia, and invasive squamous carcinoma) by expert clinicians and untrained observers. In addition, quantitative features were calculated from each image and used to classify images. Results of both visual image interpretation and objective classification were compared to the gold standard of histopathologic diagnosis.

Results: HRME images were obtained from 141 sites in resected specimens from 13 patients. Subjective image interpretation yielded sensitivity and specificity of approximately 85 to 90% and 80 to 85%, respectively, with expert observers demonstrating improved specificity compared to untrained observers. The objective

---

classification algorithm achieved sensitivity and specificity of 85% and 78% respectively; the area under the receiver-operator characteristic curve was 0.88.

Conclusions: High resolution optical imaging can image histologic features of oral neoplasia without the need for biopsy; both subjective image interpretation and objective image analysis yield information useful for classifying oral neoplastic lesions.

4.2 Introduction

In the U.S., the overall five-year-survival rate for patients with squamous carcinoma of the oral cancer is only 54%, one of the lowest rates of all major cancers; in developing countries survival rates drop below 30% [88, 89]. Patients with early lesions have better chances for cure and less treatment-associated morbidity, yet despite the easy accessibility of the mouth, most patients present with advanced tumors, when treatment is more difficult, more expensive and less successful compared to earlier interventions [90]. Improved screening and early diagnosis of oral cancer could benefit the global population substantially.

Optical imaging technologies have the potential to improve early detection of oral neoplasia; optical technologies can non-invasively assess the morphologic and biochemical changes associated with the development of precancer and cancer in real time at the point-of-care [91, 92]. Widefield optical imaging of broad areas of oral mucosa could enable clinicians to determine optimal sites for pinpoint probe interrogation and/or biopsy, reducing the chance of sampling error [93, 94]. High resolution optical imaging can be used to directly visualize changes in epithelial morphology in suspicious regions of tissue [42, 95]. Driven by advances in consumer

electronics, high quality optical images can now be obtained with low cost devices; tandem advances in digital signal processing provide the ability to automate image analysis. These advantages have the potential to improve screening, in settings ranging from tertiary care centers to regions with limited personnel and infrastructure.

A number of studies have explored the use of high resolution optical imaging for improved detection of oral neoplasia [96, 97]. Reflectance confocal microscopy has been used to image changes in cell and nuclear morphology, nuclear to cytoplasmic ratio, and epithelial architecture associated with early oral neoplasia [98]. A fiber optic reflectance confocal microscope, comprising a single optical fiber and a resonating tuning fork at the distal tip, has been integrated into an endomicroscope platform to enable high resolution fluorescence imaging of suspicious lesions in the oral cavity [99]. Fiber optic systems have also been developed to perform *in vivo* confocal fluorescence microscopy imaging. One such device, the cellVizio (Mauna Kea Technologies, Paris, France) uses a galvanometric scanner to raster scan laser light across the proximal tip of a coherent fiber bundle to enable confocal fluorescence imaging of tissue at the distal tip of the device. This technique has been used successfully to image gastrointestinal and respiratory epithelium and other tissues *in vivo* [100, 101]. While these fiber optic confocal microscopes can obtain high resolution images of tissue in real time, they are technically complex and expensive.

An alternative to confocal microscopy is high resolution microendoscopy [29, 73]. The high-resolution micoendoscope (HRME) uses a coherent fiber bundle to obtain high resolution fluorescence images of the tissue in contact with the distal tip of the

device without the need for complex mechanical scanning systems and associated control electronics [102, 103]. The system uses a low-cost LED to provide illumination and a consumer-grade CCD camera to capture high resolution digital images on a laptop computer.

A topically applied fluorescent dye, proflavine, is used to preferentially stain cell nuclei. Proflavine is an acridine-derived dye which binds to DNA in a reversible and non-covalent manner by intercalating between base pairs [104, 105]. Proflavine has been safely used for years as one of the main component of triple dye, applied to the umbilicus of newborns to prevent infection [106]. In addition, a number of *in vivo* imaging studies have been performed using topically delivered proflavine as a contrast agent [44, 107]. The ability to stain epithelial cell nuclei is useful for precancer and cancer imaging applications since it allows for visualization of features such as nuclear-to-cytoplasmic ratio. Because digital images are acquired, quantitative analysis of this and other image metrics can be easily performed to aid in image analysis [85].

The goal of this study was to evaluate the ability of high resolution microendoscopy to detect oral neoplasia. HRME images from each site were analyzed qualitatively by visual inspection and quantitatively using digital image analysis algorithms to determine whether the imaged site contained neoplastic tissue. Results of image analysis were compared to the gold standard of histopathology to assess the ability of HRME to correctly identify the presence of neoplasia.

4.3 Methods

4.3.1 Patients and data collection

Patients over 18 years of age scheduled for surgery to remove a previously diagnosed oral squamous carcinoma or dysplasia were eligible to participate in the study. Informed consent was obtained from all study participants, and the study was reviewed and approved by the Institutional Review Boards at the University of Texas M. D. Anderson Cancer Center and Rice University. Subjects underwent standard-of-care surgery to remove neoplastic oral lesions and associated margins. Following surgical resection, the tumor specimen was taken to the lab for imaging.

A solution of Proflavine (Sigma-Aldrich) dissolved in water at a concentration of 0.01% (w/v) was prepared prior to performing imaging. The contrast agent solution was directly applied to the epithelial surface of the resected tissue with a cotton tipped swab, and imaging with the HRME device was performed immediately. The application of proflavine does not discolor the tissue surface, and is not detectable in tissue slides prepared using standard histopathology processing and H&E staining (Figure 4-1).

After imaging, the tissue was returned for standard histopathology processing, and slides were later reviewed by a board-certified pathologist (M.D.W.). Photographs of the gross specimens were obtained before and after placement into individual specimen cassettes and were used to obtain histopathologic diagnoses for each of the sites imaged with the HRME. At each site imaged, the pathologic diagnosis was determined, using five diagnostic categories (normal, mild dysplasia, moderate dysplasia, severe dysplasia, and cancer).

4.3.2 HRME System

The HRME device has been previously described in detail [102]. Briefly, images are acquired with this device by placing the tip of the fiber bundle into direct contact with the epithelial surface of the tissue. Excitation light from a blue LED with a center wavelength of 455 nm is delivered through the fiber bundle. The fluorescence emission from the topically applied proflavine is collected through the fiber bundle, focused onto a CCD camera, and a digital image is stored for future processing and analysis. The HRME system has a circular field of view with a diameter of 750 microns; the lateral spatial resolution of the system is approximately 4 microns.

4.3.3 HRME Image Analysis

HRME images were reviewed to determine whether the endoscope tip was in contact with the tissue surface or whether the probe tip moved during image acquisition. Images showing such artifacts were discarded and not used in subsequent analyses.

HRME images passing quality control were reviewed by a group of three expert and two non-expert observers. Expert observers included Head and Neck Pathology Fellows from the University of Texas M.D. Anderson Cancer Center, while non-expert reviewers included graduate students from the Department of Bioengineering at Rice University. Reviewers were first shown a small number of HRME images of the oral cavity acquired previously from sites with known histopathology; this training set consisted of images from 5 pathologically normal and 5 pathologically neoplastic measurement sites. Reviewers were subsequently asked to rate HRME images from all study sites; for each measurement, the observer was asked to rate the image on a five-

point scale, with 1 being "definitely non-neoplastic," 2 being "probably non-neoplastic," 3 being "unknown," 4 being "probably neoplastic," and 5 being "definitely neoplastic." The analysis of the subjective scoring was performed identically and separately for results from each of the two groups of observers.

To evaluate the accuracy of qualitative image interpretation, a 5-point receiver-operator characteristic (ROC) curve was calculated, comparing the results of HRME image analysis to that of the gold standard of histopathology. To construct the ROC curve, the threshold for qualitative image analysis to be considered abnormal was varied from 1 to 5. The subjective rating at each measurement site was compared to this threshold; if the subjective rating was greater than or equal to the threshold, the image interpretation was considered "neoplastic." Otherwise, the image interpretation for the measurement was considered "non-neoplastic." This result was compared to the histopathology-confirmed diagnosis, sensitivity and specificity were calculated, and a five point ROC curve was constructed for each observer. Sites with a pathologic diagnosis of normal or mild dysplasia were considered to be non-neoplastic, while sites with a pathologic diagnosis of moderate dysplasia, severe dysplasia or cancer were considered to be neoplastic.

To pool the results of the non-expert group, a majority voting scheme was used to construct a single ROC curve. For a given threshold, the "non-neoplastic" or "neoplastic" image interpretation was noted for each observer at each site. Since there were an odd number of observers in the non-expert group, the pooled interpretation was considered to be the most frequent interpretation. This result was compared to the

histopathology-confirmed diagnosis, sensitivity and specificity were calculated, and a pooled, five-point ROC curve was constructed.

We explored the diagnostic ability of quantitative image analysis. A rectangular region of interest (ROI) was selected from the image of each independent site; ROIs were chosen from areas of the image illustrating cellular detail, when present. The ROIs from each image were then used in the following quantitative analysis. Fifty-nine distinct features were computed for each ROI (Table 4-1). First-order statistical features (variance, entropy, etc.) were calculated directly from the grayscale pixel values. A gray-level co-occurrence matrix (GLCM) with pixel offsets from 1 to 10 was used to calculate additional textural feature groups (correlation, contrast, homogeneity, and energy) [108]. Each GLCM feature group contained 10 distinct features, for each pixel offset within the GLCM. To detect nuclear features, an extended regional maximum transform was applied to the image. Voronoi tessellations were calculated from the centroids of the nuclear features to calculate internuclear distances [85]. A Fourier transform was applied to the ROI to calculate the power spectrum of the image; this was divided into 10 units to represent the frequency components of the image [109, 110].

A diagnostic algorithm was used to classify each ROI as non-neoplastic or neoplastic based on these image features. Histopathology was used as the gold standard; sites with a pathologic diagnosis of normal or mild dysplasia were considered to be non-neoplastic, while sites with a pathologic diagnosis of moderate dysplasia, severe dysplasia or cancer were considered to be neoplastic. The classifier was based on two-class, linear discriminant analysis; a sequential forward feature-selection algorithm initially was used to select the best performing subset of up to 10 image features to

classify the data. Initially, the best performing single feature was identified, and then subsequent features were selected which gave maximum performance when combined with previously selected features. The algorithm was developed using five-fold cross-validation; each measurement site was initially randomly assigned to one of five groups. Four-fifths of the data were then used to train the linear classification algorithm and the remaining one fifth of the data were used to test the algorithm. This cycle was repeated four additional times so that the algorithm was tested using data from each site. Performance was monitored by calculating the area under the curve (AUC) of the classifier.

Alternatively, three-class diagnostic algorithms were developed to classify each RO1 as: (1) normal or mild dysplasia, (2) moderate or severe dysplasia, and (3) cancer. Both linear discriminant analysis and a categorical tree-based classifier were used [111, 112]. The linear discriminant algorithm was trained using five-fold cross validation,as described above. Sequential feature selection was performed in each training fold, choosing the best performing pair of features. A categorical tree classifier was also allowed to choose among the entire feature set. The tree classifier was directed to choose the top performing two-feature feature subset while performing classification on the entire data set, and was pruned to three terminal nodes to avoid overtraining. The predicted classification results from each classifier were then compared to the histopathology for each site.

4.4 Results

4.4.1 Patients and Sites:

Thirteen subjects enrolled in the study. Images were obtained from 150 unique sites; images from 141 of these sites passed the QC review and were used for further analysis. Of these 141 sites, 40 were histologically confirmed to be normal squamous, 11 were mild dysplasia, 11 were moderate dysplasia, 12 were severe dysplasia, and 67 were invasive squamous carcinoma. Figure 1 shows representative HRME images (top row) of
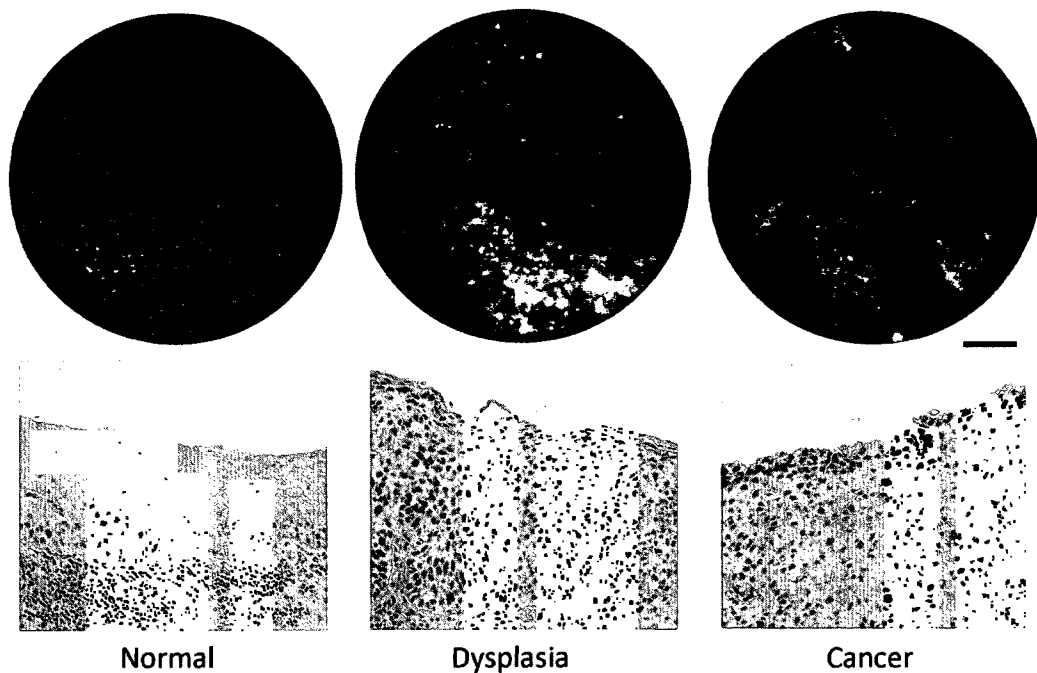
Figure 4-1: Illustration of HRME images (top row) compared to H&E images (bottom row). From right to left, diagnostic categories are: normal squamous mucosa, moderate dysplasia, and invasive squamous carcinoma. All images are sized to the same scale; scale bar represents 100 μm.

non-neoplastic, moderate dysplasia, and invasive cancer, respectively. Histopathology images can be seen below. All images are at the same scale for comparison. The HRME image of normal squamous epithelium shows small, bright nuclei with dark cytoplasm and relatively large internuclear separation. The image of dysplastic epithelium shows a marked increase in nuclear-to-cytoplasmic ratio, and the image from invasive carcinoma shows a distinct loss of cellular organization and internuclear separation.

Feature	Explanation
Entropy	Statistical measurement of randomness of grayscale values
Correlation (10)	Pixel neighbor correlation over the entire image
Variance	Variance of pixel grayscale values
Standard Deviation	Standard deviation of grayscale values
Energy (10)	Sum of squares in gray-level co-occurrence matrix (GLCM)
Kurtosis	Measure of the flatness of the pixel value distributions
Homogeneity (10)	Closeness of the distribution of the GLCM elements to the diagonal
Skewness	Measure of the symmetry of the pixel value distribution
Contrast (10)	Measure of pixel intensity compared to its neighbors over the entire image
Std. Dev. Nuclear Separation Distance	Standard deviation of nuclear separation as calculated by Voronoi tessellation
Frequency (10)	Frequency distribution of pixel values
Mean Nuclear Separation Distance	Mean nuclear separation as calculated by Voronoi tessellation
Mean Minimum Nuclear Separation Distance	Average minimum nuclear separation as calculated by Voronoi tessellation
Nuclei Per Unit Area	Number of nuclei detected divided by area of region of interest

Table 4-1: Quantitative image features. The table is in order of performance as roughly estimated by a linear discriminant analysis using the entire data set for training and testing.

4.4.2 Subjective image interpretation:

Figure 2(a) shows the ROC curve for each of the non-expert observers and for the pooled non-expert group. Performance was improved when scores were combined using a voting scheme. Figure 2(b) shows the ROC curve for each of the expert observers and for the pooled expert group. The performance of both groups is qualitatively similar, but expert clinicians outperformed the untrained observers. In particular, expert clinicians appeared to have better sensitivity at distinguishing normal from abnormal groups than untrained observers.
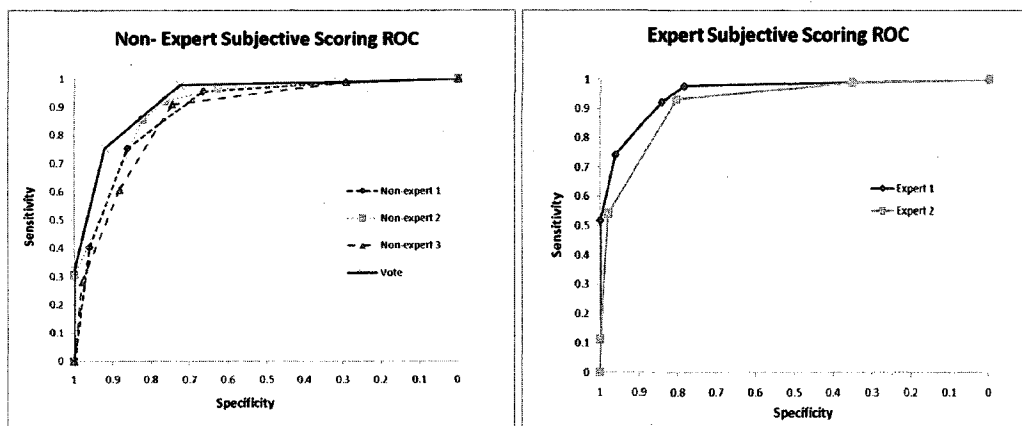
Figure 4-2: Subjective image analysis receiver-operator characteristic (ROC) curves. Left, non expert individual and pooled results (solid line). Right, expert individual results.

4.4.3 Quantitative image feature calculation

A representative image showing the rectangular region of interest (ROI) selected from the HRME image from a site with a pathologic diagnosis of invasive carcinoma is shown in Figure 4-3a; the ROI was selected from the region of the image with easily recognized cell nuclei. Quantitative image features calculated from the ROI from each site were ranked according to their diagnostic ability. Image features in Table 4-1 are listed in order of descending area under the ROC curve for the single-feature, two-class linear discriminant analysis classifier. The single best performing feature was found to
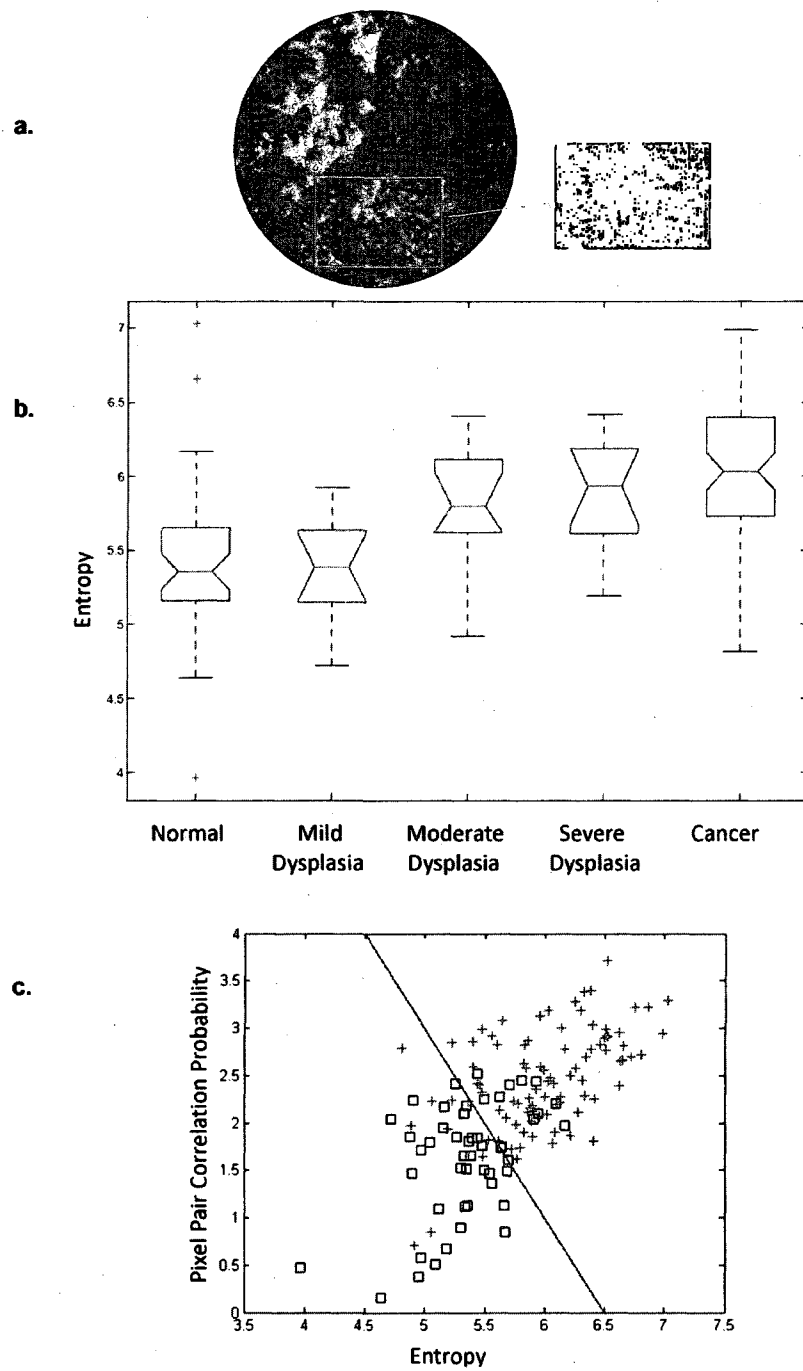
Figure 4-3: Quantitative analysis. 4-3a. Illustration of ROI selection; note region containing visible cell nuclei selected by the observer. 4-3b. Box

plot showing the classification utility of entropy as a single feature. Note the separation between normal squamous and mild dysplasia compared to moderate and severe dysplasia and cancer. 4-3c. Measurement sites plotted using two features. Non-neoplastic sites are plotted as blue squares, neoplastic sites are plotted as red crosses. The decision line is shown.

be the entropy value of the ROI. Figure 4-3b shows a box plot representing the entropy, averaged for each of the five histopathologic categories. On average, the entropy is higher for sites with moderate dysplasia, severe dysplasia and cancer than for normal sites or sites with mild dysplasia.

The top performing combination of two features was found to be entropy and the pixel pair correlation probability. Figure 4-3c shows a scatter plot of these two features for each of the 141 sites in the dataset. Samples with a pathologic diagnosis of normal or mild dysplasia are shown as blue squares, while samples with a pathologic diagnosis of moderate dysplasia, severe dysplasia or cancer are shown as red crosses.

Figure 4-4a shows the AUC as a function of the number of image features selected in the linear discriminant algorithm. AUC increases from one to two features, but is not improved by addition of more features. Therefore, only two features were used to train the linear classification algorithm. Figure 4-4b shows a scatter plot of the posterior probability that each site is neoplastic as calculated by the linear classifier; samples are grouped by histopathologic diagnosis. Figure 4-4c shows the ROC curve for

the linear discriminant classifier based on these two features. The AUC is 0.88 and the

sensitivity and specificity at the Q-point are 85% and 78%, respectively.
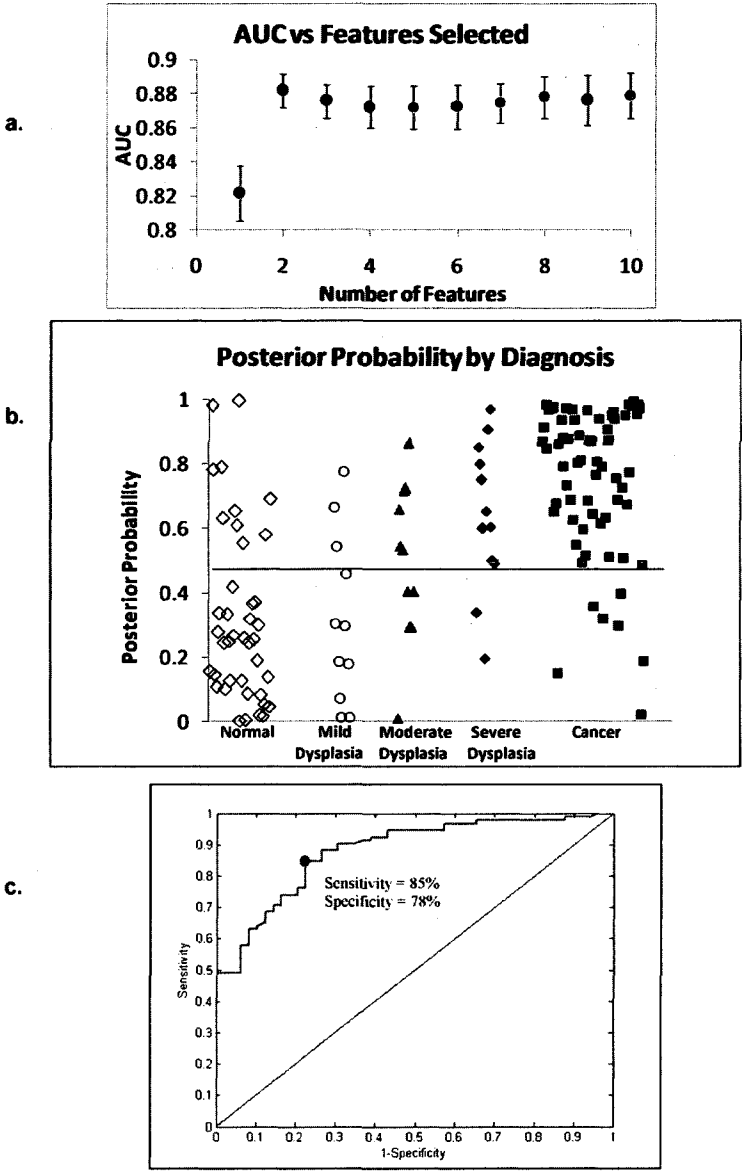
Figure 4-4: Classification performance. 4-4a. Calculated classification

performance versus number of features used; note the plateau at two features.

4-4b. Scatter plot of calculated posterior probability generated by a two-feature linear discriminant analysis (LDA) algorithm. The decision is shown at 0.46. 4-4c. ROC curve of calculated classification performance using the two-class, two-feature LDA. The Q-point is shown corresponding to a sensitivity of 85% and a specificity of 78%.

	Linear Classifier				Tree-based Classifier		
	Normal (true)	Dysplasia (true)	Cancer (true)		Normal (true)	Dysplasia (true)	Cancer (true)
Normal (predicted)	67	9	13	Normal (predicted)	67	13	3
Dysplasia (predicted)	16	68	24	Dysplasia (predicted)	6	30	6
Cancer (predicted)	17	23	63	Cancer (predicted)	27	57	91

Table 4-2: Three-class algorithm results.

Table 4-2 summarizes the performance of both three-class algorithms. The tree-based classification algorithm selected pixel correlation and entropy as features; pixel correlation was used to separate cancer from normal and dysplasia, while entropy was used to separate normal and mild dysplasia from moderate and severe dysplasia. The same features were selected for the linear three-class classifier. The linear classifier correctly predicted the class for 67% (normal), 68% (dysplasia), or 63% (cancer) of the measurement sites. In comparison, the tree-based classifier had the same performance for discriminating normal measurements, but had a high false-positive rate for classifying

dysplasia (incorrectly predicting 57% of dysplasia sites to be cancer). The tree-based classifier performed well when discriminating cancer measurement sites (91% correct).

4.5 Discussion

This study demonstrates the use of a robust, high-resolution microendoscope to image cellular and architectural features of oral neoplasia. Both subjective visual interpretation of images and objective analysis of digital images can differentiate non-neoplastic and neoplastic oral mucosa with high sensitivity and specificity relative to the gold standard of histopathology.

While these results are encouraging, there are a number of limitations associated with HRME imaging. The surface imaging strategy employed by this device cannot image submucosal tumors. In addition, significant hyperkeratosis or superficial necrotic debris may also preclude visualization of the cell layers that lie beneath. These limitations can potentially be overcome by one of two strategies: optical sectioning or mechanical penetration into deeper tissue. Optical sectioning, as used in confocal microscopy, enables an optical device to collect high-quality images from several hundred microns below the tissue surface [99, 113, 114]. Alternatively, the fiber optic bundle used in the HRME is less than 1 millimeter in diameter, and can be inserted through the lumen of a 16 gauge hypodermic needle. In this fashion, the tip of the image guide can be directly inserted into deeper tissue, avoiding any keratin or debris layer at the surface. Such a technique has been previously demonstrated in an *in vivo* imaging study of a subcutaneous oral squamous carcinoma xenograft tumor [102].

The ability of the HRME to image subcellular features of neoplasia could have a number of clinical applications. Tumor margin detection during surgical removal is essential to minimize the chances of recurrence [115, 116]. HRME imaging could be used to provide high-resolution information of the tissue margins to the surgeon as the procedure is taking place. Nearly-instantaneous return of high-resolution information can be clinically significant for both screening and margin-detection in the operating room, and could be used as a complement to current frozen section histopathology [117]. Mapping the extent of a tumor while performing the surgical removal of a tumor could be of great benefit in assuring that no abnormal tissue remains.

In addition to being well-suited as an intra-operative margin detection tool, the HRME shows potential as an oral cancer screening tool, particularly in combination with other widefield imaging techniques. One of the limitations of the HRME is that only a small FOV can be sampled at a time. By combining this technology with a widefield imaging device, which can quickly collect data from the entire oral mucosa, the potential exists to increase the sensitivity and specificity obtained with either device alone. Suspicious lesions exhibiting a loss of autofluorescence signal strongly correlate with dysplasia and cancer with high sensitivity and specificity. This loss of fluorescence in wide field imaging has been postulated to be due to a loss of collagen crosslink fluorescence [118]. It is currently unclear whether a significant loss of fluorescence can also occur in the presence of benign conditions such as inflammation. A small, flexible point probe imaging system would be an asset in distinguishing the difference between benign and malignant lesions and help guide further diagnostic workups. Any lesion exhibiting a loss of autofluorescence as seen with a wide field imaging modality could be

quickly inspected with the HRME probe. Instantaneous feedback to the surgeon would then guide further workup for the patient.

The HRME represents a low-cost and more robust alternative to confocal imaging systems, ideally suited to a region where high turnover and poor patient follow-up occurs. In addition, by using a quantitative algorithm to aid in discriminating between different tissue types, the need for highly trained expert operators is reduced. This device is well suited as a complement to other widefield imaging techniques for early detection of cancer in the oral cavity. Collecting such instantaneous high-resolution image data of suspicious lesions can speed the diagnosis of malignant or premalignant lesions that can are candidates for surgical resection.

Chapter 5: Widefield multispectral imaging and high-resolution microendoscope imaging for detection of oral neoplasia[3]

5.1 Introduction

Squamous carcinoma of the head and neck is associated with poor five-year survival, usually a consequence of late-stage disease at diagnosis [119]. Treatment of oral cancer is associated with severe morbidity; surgical removal of oral tissue often results in disfigurement and impairs speech and the ability to swallow. Diagnosis of head and neck cancers at an earlier stage can improve reduce morbidity and improve efficacy of therapy, leading to improved patient survival and quality of life.

The current standard-of-care to screen for oral cancer is white light inspection of the oral cavity by an expert clinician, followed by biopsy and histologic analysis of suspicious lesions. Subjective visual examination requires adequately trained personnel, as well as the availability of histopathology labs to analyze biopsy specimens of suspicious lesions. Even in developed nations, lesions are commonly not discovered until a late stage because of the relative lack of screening.

Optical methods offer a means to improve screening for oral neoplasia at the point of care without the need for extensive infrastructure. Autofluorescence visualization is a promising tool to detect early neoplastic changes in the oral epithelium. The Velscope is a commercial system that uses blue light to excite autofluorescence in the oral mucosa; a

clinician can then visually inspect the mucosa and identify suspicious areas based on loss of autofluorescence [93, 120]. It has been demonstrated that precancer and cancer are associated with loss of stromal collagen fluorescence [121].

Computer-aided tools and quantitative classification algorithms can be used to further improve the screening process and provide an objective diagnosis. Digital imaging of the autofluorescence signal from the oral mucosa allows quantifiable image parameters to be calculated; the red-to-green pixel intensity ratio has been of particular importance in distinguishing between neoplastic and non-neoplastic sites. A recent study by our group using this technique achieved a sensitivity of 100% and specificity of 91.4% in an independent validation data set [122].

A potential limitation of widefield imaging and analysis of the bulk tissue autofluorescence signal is that this modality does not directly sample some of important pathologic features, such as changes in cellular and nuclear morphology. High-resolution imaging may be used to complement the diagnostic capability of widefield imaging. High-resolution imaging can be used to directly observe changes in epithelial cell morphology and epithelial architecture over small fields-of-view. These changes include increased nuclear-to-cytoplasmic ratios, pleomorphism, and alterations in the gradation of cellular differentiation throughout the epithelium. A variety of high resolution optical imaging modalities are available to sample these morphologic and architectural changes, including confocal micrscopy, optical coherence microscopy and high resolution microendoscopy [82, 114, 123].

Multimodal imaging approaches which combine images from wide field and high-resolution modalities have the potential to improve early detection of neoplastic changes.

Wide field imaging allows for rapid inspection of nearly the entire oral cavity, while high-resolution imaging can be used to interrogate suspicious regions with higher spatial resolution.

The goal of this study was to explore the complementary diagnostic ability of widefield autofluorescence imaging ad high resolution microendoscopy for early detection of oral neoplasia. Widefield autofluorescence images were obtained from resected oral tumors; high resolution images were then obtained following topical application of a fluorescent contrast agent to visualize changes in nuclear morphometric and density. The ability to classify oral tissue as normal or neoplastic was explored using data from widefield imaging along, high resolution imaging alone and the combination of the two modalities. Multimodal approaches yielded the greatest sensitivity and specificity relative to the gold standard of histopathology, supporting the complementary role of these two imaging approaches.

5.2 Methods

5.2.1 Data Acquisition and Instrumentation

Data was collected under a clinical protocol approved by the Institutional Review Boards at the University of Texas MD Anderson Cancer Center and Rice University. All participating subjects gave written informed consent. Patients were eligible if they were 18 years old or older and were scheduled for surgical resection of a known precancerous or cancerous lesion in the oral cavity.

Following resection, tissue was imaged in the laboratory using first a widefield multispectral digital microscope (MDM) and then a high resolution microendoscope

(HRME) system. The MDM is described in detail elsewhere [94]. Briefly, the MDM system is a modified clinical microscope which collects digital images with an approximate 5 cm by 7 cm field of view (FOV). The system is capable of collecting data in several different imaging modalities but for this study only white light reflectance and autofluorescence images at 405 nm excitation were utilized. The entire mucosal surface of the resected tissue was imaged using the MDM.

The HRME system is described in detail elsewhere [103]. Briefly, the system can image cellular detail of the upper epithelium by placing a fiber optic image guide guide into direct contact with the tissue. Contrast is achieved by applying a topical solution of proflavine (0.01% in water) with a cotton swab immediately before imaging. Proflavine is a fluorescent agent that binds to DNA, yielding bright nuclei surrounded by dark cytoplasm. The HRME system uses an LED with a center wavelength of 455 nm as an excitation source; this is directed through an objective lens and coupled to the fiber optic image guide, which delivers it to the tissue surface. Fluorescence emission light travels back though the image guide, is magnified by the objective lens, and is imaged to a CCD camera, where it is digitally stored and sent to a PC. The HRME system has a circular field of view with a diameter of 750 microns, and collects image data at 4 frames per second.

Both clinically normal and suspicious areas were measured with both the MDM system and the HRME system. Several suspected non-neoplastic and neoplastic sites were imaged on each resected specimen. HRME images were qualitatively assessed by the authors (TJM and DMR) for the presence of nuclear detail. Only HRME images which revealed nuclear detail were included in this study. For each interrogated tissue

site, one or more HRME images were collected inside a small, approximately 2 millimeter diameter area.

Histopathology diagnosis was obtained from the sites imaged with the MDM and HRME. The locations of regions imaged with the HRME were recorded using digital photography, and these locations were tracked throughout histopathology processing. The resected tissue was sectioned and stained according to standard histopathology practice and diagnosis was obtained from prepared slides by an expert Head and Neck pathologist (M.D.W.).

5.2.2 Computer Aided Diagnostics

Image data obtained with both the MDM and HRME were used to develop objective classifiers to identify neoplastic tissue. Images from each device were first processed and used to train a linear discriminant classifier based on a single imaging modality. MDM and HRME results were then combined using multiple hybrid consensus techniques to train multimodal classifiers. Tissue sites imaged with both the MDM and HRME and with a corresponding pathologic diagnosis were included in this analysis.

For analysis of MDM data, circular regions of interest (ROIs) with a 20 pixel diameter, which correspond to an approximate 1mm diameter circular region of tissue, were selected from MDM images at sites imaged by the HRME. In addition, a normalization ROI was identified in each specimen from a pathologically normal area, distant from any lesion. Features obtained from the pixel values inside these regions were then extracted. Previous *in vivo* studies have shown that the mean ratio of red to

green autofluorescence at 405 nm excitation, normalized to a known non-neoplastic

region, provides a high degree of discrimination between non-neoplastic and neoplastic

tissue [122, 124]. This feature was extracted from the ROIs of MDM images collected in

this study; these values were normalized by the mean red to green autofluorescence ratio

from the normalization ROIs.

This feature was used as input to a 2-class linear classifier based on Bayesian

parameter estimation in order to obtain a predicted diagnosis of either non-neoplastic or

neoplastic. The neoplastic class includes ROIs with diagnoses of mild, moderate, and

severe dysplasia as well as carcinoma in situ and invasive carcinoma. The non-neoplastic

class included epithelial tissue which was histopathologically normal with or without

hyperplasia, hyperkeratosis, or inflammation. Leave-one- patient-out cross-validation

was used avoid overtraining the algorithm [125]. A posterior probability was obtained

for each site which is the predicted probability that the site is in the neoplastic class. A

receiver-operating-characteristic (ROC) curve was generated by changing the threshold

of the posterior probability value used to determine if a measurement was in the first or

second class, and then plotting 1-specificity versus sensitivity at each threshold value or

operating point. The area under the curve (AUC) of the ROC plot was used as a figure-

of-merit (FOM) to determine classification performance. Sensitivity, specificity, positive

predictive value, and negative predictive value were also determined at the operating

point which maximized the sum of sensitivity and specificity and reported.

A variety of features were extracted from the HRME images at each site and used

as input to a linear classifier. Regions of interest were manually selected from each

HRME image, corresponding to regions subjectively showing the most nuclear detail. In

addition, this ROI selection was done to eliminate the boundaries of the images, which did not contain any information. Features were extracted from these rectangular ROIs. In the cases where there was more than one HRME image collected from a site, the mean of these feature values was used for classification. First order statistical features such as the mean, standard deviation, and entropy of pixel values were extracted from the ROIs. Textural features obtained from gray-level co-occurrence matrices with pixel offsets from 1 to 10 pixels were also obtained. Spatial frequency content features were extracted by performing a 2-D Fourier transform on the image data inside the ROIs. Further detail about these features is provided in [124].

In order to select the most diagnostically valuable features from the HRME data, a forward sequential feature selection algorithm was implemented [125]. This algorithm tested each feature separately and then in combination using the linear classifier to determine the two features which classified the data most accurately based on maximal area under the ROC curve. Two features were chosen because adding additional feature did not statistically improve classification performance. The HRME data were classified using the linear classifier with the two selected features using leave-one-out cross-validation. Again, a posterior probability was obtained for each site An ROC plot, AUC, sensitivity, specificity, positive predictive value, and negative predictive value were obtained.

5.2.3 Combinatorial methods

Two separate strategies were implemented to combine data from both imaging modalities to yield a single diagnosis. The first approach used was to develop a classifier

using input from both imaging modalities to obtain a single diagnosis. We refer to this technique as the Nondirected Combinatorial Technique. The second strategy, referred to as the Directed Combinatorial Technique, used data from the MDM to first identify potentially neoplastic sites. At these sites, data from both the MDM and HRME modalities were used to classify the site as neoplastic or non-neoplastic. The Directed Combinatorial Technique was implemented by first using data from the MDM to train and test a linear classifier using input from all of the measurement sites. The operating point for this classifier was selected such that a sensitivity of 90% was achieved. Sites classified as non-neoplastic by this algorithm were not analyzed further. Sites classified as potentially neoplastic by this algorithm were analyzed further. A second algorithm was developed using both MDM and HRME data from these sites.

For both the Directed and Nondirected Combinatrorial Techniques, we explored eleven different methods to combine the results from two devices. Eight of these methods rely on combining the posterior probabilities obtained from each device for each site to produce a new metric which can be used to discriminate the classes. Many of these methods are described by Bendiktsson et al. [126]. The other three methods explored involve utilizing one or more classifiers in a different way, as described below.

The posterior probabilities (pp) per site were combined from the two devices in the following eight ways:

1. The maximum of the two pp's was used,

2. The minimum of the two pp's was used,

3. The mean of the two pp's was used,

4. The weighted sum of the two pp's was used where the weights were determined heuristically by the relative performance of each device. We have used the AUC obtained from each device as the FOM to determine the weights. This method is called Linear Opinion Pool (LOP).

5. The weighted sum of the two pp's (LOP) was used where the weights were determined by a search of different weights. The weights of each device were between 0 and 1 and the weight from the second device w_2, was equal to 1- w_1, where w_1 is the weight for the first device. Weights were tested in .01 increments.

6. The product of the two pp's was used. This method is called Logarithmic Opinion Pool (LOGP).

7. The weighted product of the two pp's (LOGP) was used where the weights were determined by a search. The weights were applied as exponents for the pp's.

8. The weighted sum of the two pp's (LOP) was used where weights were determined both per device and per class. This method is described in reference [126].

In addition to these methods, three other methods were used to synthesize the data. The pp from the MDM was used as the prior probability for the HRME linear classifier; extracted features from both devices were used in a single linear classifier; and the pp from the MDM was used as an additional feature for the HRME linear classifier.

5.3 Results

In total, resected specimens were obtained from 14 patients. Six of the resected specimens primarily involved the tongue, three primarily involved the floor of mouth, two primarily involved the buccal mucosa, one primarily involved the retromolar trigone, one involved the tongue and floor of mouth and one involved the gingiva and floor of mouth. From these specimens, 69 unique measurement sites were matched to a corresponding pathology diagnosis. These sites included 26 sites with a diagnosis of non-neoplastic, 3 sites with mild dysplasia, 4 sites with moderate dysplasia, 13 sites with severe dysplasia or carcinoma in situ, and 23 sites with invasive squamous cell carcinoma. When divided into two classes: the non-neoplastic class contains 26 sites and the neoplastic class contains 43 sites.

A ROI from the MDM autofluorescence images was selected at the each of the 69 sites. A normalization ROI was chosen for each patient and corresponded to a histopathologically normal area. 126 HRME ROIs were obtained from the 69 sites; when multiple ROIs were available, the features were averaged together.

Figure 5-1a shows a representative MDM autofluorescence image at 405 nm excitation collected from resected tissue from the floor of mouth. MDM ROIs are indicated from a site with squamous cell carcinoma (red circle) and a site which is non-neoplastic (blue circle). Note the relative decrease in autofluorescence at the carcinoma site. Figure 5-1b shows an HRME image collected at the carcinoma site. Figure 5-1c shows an HRME image for the non-neoplastic site. Note the nuclear crowding and disorganized architecture in 5-1b compared to 5-1c.
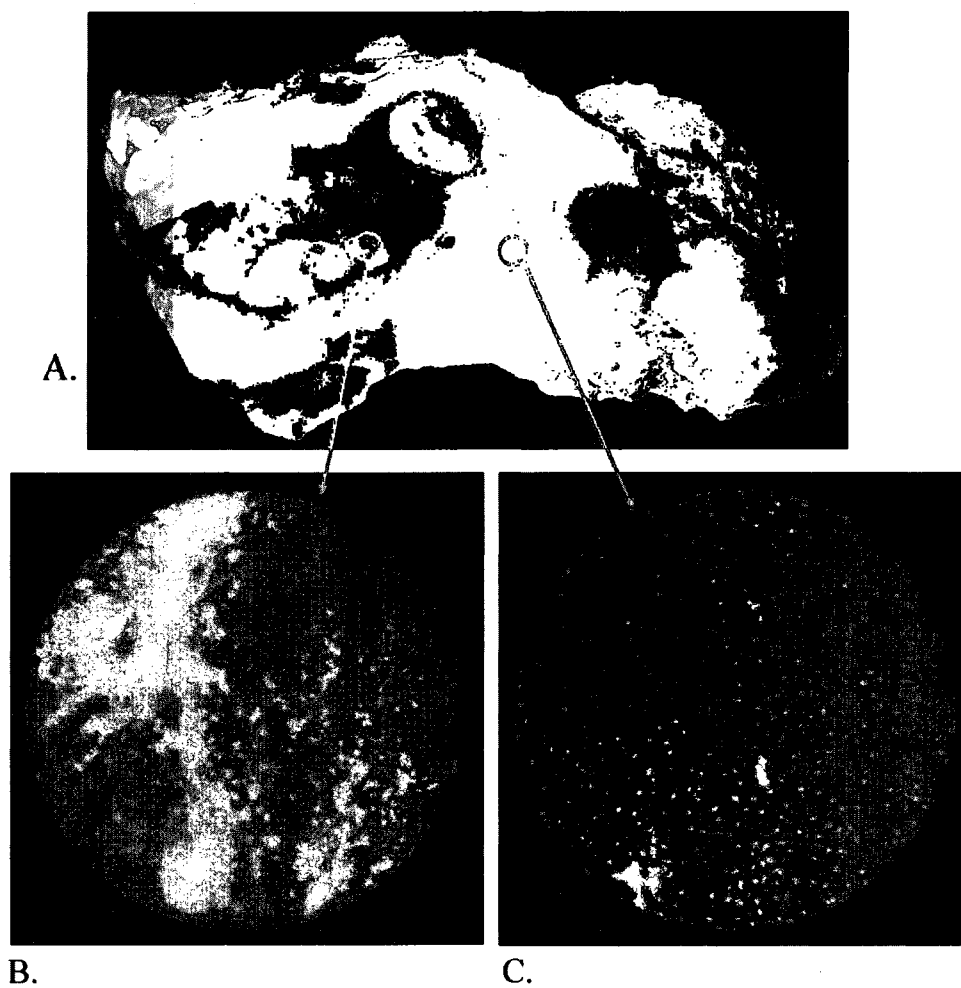
Figure 5-1: 5-1a. MDM Autofluorescence image at 405 nm excitation from resected tissue from the floor of mouth. MDM ROIs from a squamous cell carcinoma (SCC) site and a non-neopalstic site are indicated. 5-1b. HRME image collected from the SCC site. 5-1c. HRME image collected from the non-neoplastic site.

Figure 5-2 shows results from the Nondirected Combinatorial Technique where data from both devices was used from all measurement sites. Figure 5-2a is a scatter plot of normalized red to green ratio per measurement site calculated from MDM images. The indicated discrimination line yields a sensitivity of 79.1% and a specificity of 69.2%. Figure 5-2b is the ROC curve produced by the linear classifier using this feature alone. The indicated operating point corresponds to the discrimination line in Figure 5-2a and is located at the Qpoint, the point on the ROC curve which is the minimum distance from the upper left hand corner of the plot. Figure 5-2c is the scatter plot of the two selected feature values from the HRME. The two features chosen by the sequential feature selection algorithm were pixel grayscale variance (a first-order feature) and the pixel pair correlation value calculated from the gray level co-occurrence matrix at an offset of 1. The indicated discrimination line yields a sensitivity of 69.8% and a specificity of 80.8%. Figure 5-2d is the ROC curve produced by the linear classifier using these features. The indicated operating point corresponds to the discrimination line in 5-2c and is also at the Qpoint.

Table 5-1 indicates the AUC achieved using each of the 11 methods to combine data from the two modalities. Table 5-1 also summarizes the change in AUC for the combined modalities relative to the AUC achieved using each device by itself. Method 5 produces the highest AUC of all of the combination methods. This method highly favors the MDM posterior probabilities by a factor of 8. Figure 5-2e shows the ROC curve produced using Method 5, the weighted linear opinion pool of posteriors probabilities from each device. This combined method produced an AUC of .875, a sensitivity of 74.4% and a specificity of 87.5%. This AUC is a 10.9% increase of the MDM alone and

a 16.4% increase over the HRME alone. The second highest AUC (.824) was produced

by method 2 where the lower posterior probability was chosen from the devices for each

measurement site. The third highest AUC (.819) was produced by the weighted product

of posterior probabilities where the MDM was again weighted highly favorably.

Combination Method	AUC	% increase over MDM	% increase over HRME
1. Maximum posterior probability.	.794	.68	5.6
2. Minimum posterior probability.	.824	4.4	9.6
3. Mean posterior probability.	.810	2.7	7.8
4. LOP, Weighted sum of posterior probabilities, weights determined from individual AUC for devices.	.772	-2.2	2.6
5. LOP, Weighted sum of posterior probabilities, weights determined from search. $W_{MDM}=.89, W_{HRME}=.11$	.875	10.9	16.4
6. LOGP, Product of posterior probabilities.	.811	2.8	7.9
7. LOGP, Weighted Product of posterior probabilities, weights determined from search. $W_{MDM}=.87, W_{HRME}=.13$	.819	3.9	9.0
8. Weights determined for device and class.	.789	-.06	4.9
9. MDM posterior probability used as HRME prior probability.	.817	3.5	8.6
10. MDM posterior probability used as feature in HRME classifier.	.784	-.68	4.2
11. One classifier using features from both devices.	.790	.11	5.1

Table 5-1: Combinatorial methods and the AUC achieved. Both devices

were used to measure all measurement sites. The percent increase in AUC

values over each device alone is shown. Method 5 produced the highest

AUC.
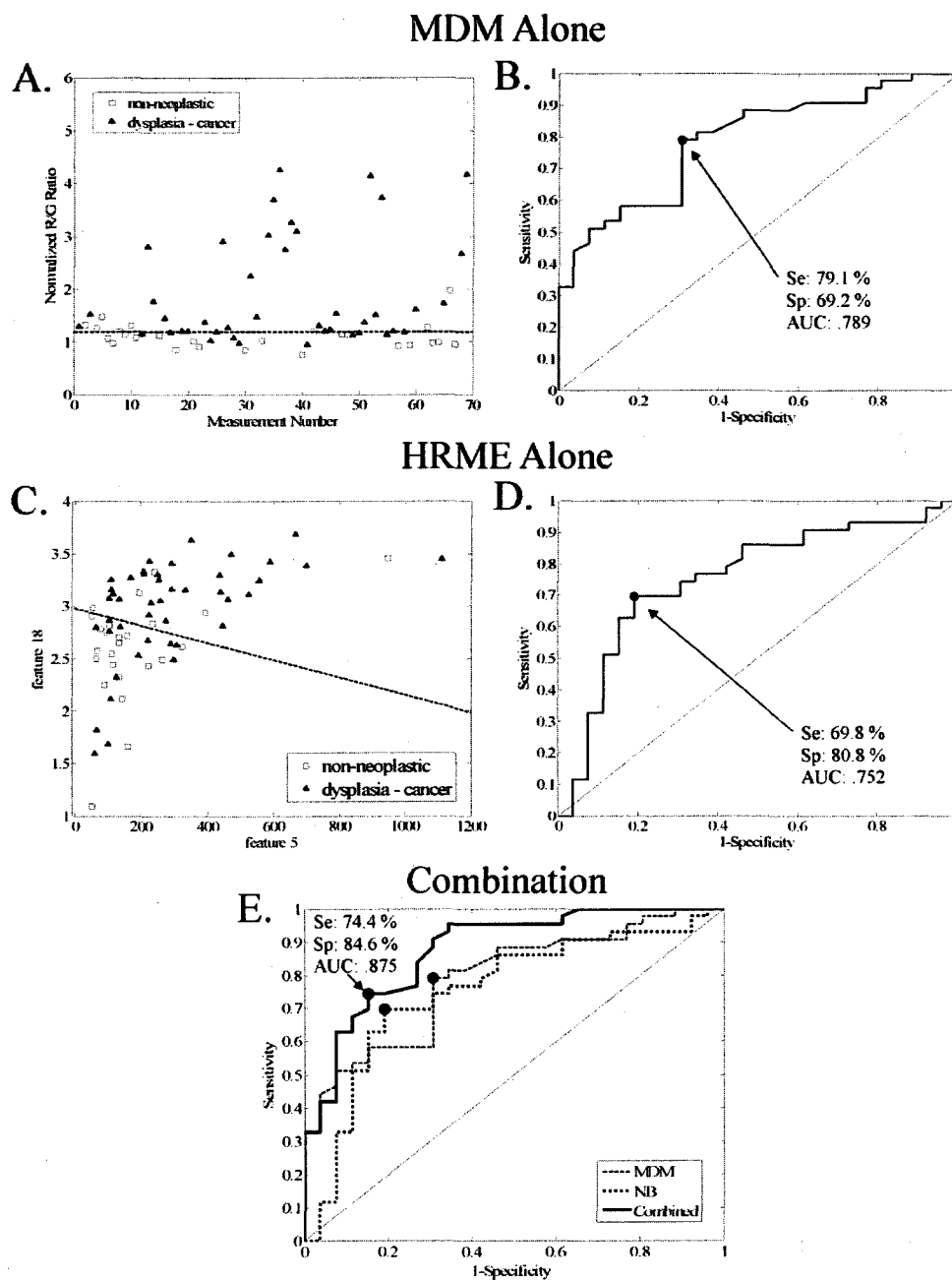
Figure 5-2: Results from the Nondirected Combinatorial Technique. Each

device was used to measure all of the measurement sites. 5-2a. Scatterplot

of normalized red to green ratio per measurement site calculated from

MDM images. The indicated discrimination line yields a sensitivity of 79.1% and a specificity of 69.2%. 5-2b. ROC curve produced by the linear classifier using this feature. The indicated operating point corresponds to the discrimination line in 5-2a. 5-2c. Scatter plot of the two selected features from the HRME. The indicated discrimination line yields a sensitivity of 69.8% and a specificity of 80.8%. 5-2d. ROC curve produced by the linear classifier using these features. The indicated operating point corresponds to the discrimination line in 5-2c. 5-2e. The ROC curves in 5-2b. and 5-2d. with the ROC curve produced by combination method 5 in table 5-1: the weighted linear opinion pool of posteriors probabilities from each device.

Figure 5-3 and Table 5-2 show results from the Directed Combinatorial Technique. The MDM was first used to identify measurement sites with a sensitivity of 90.0%. For this analysis however, the closest operating point available from the linear classifier trained on the MDM data was at 90.7% sensitivity. The HRME data was then used to aid in diagnosis of only these measurement sites. Figure 5-3a is a scatter plot of posterior probabilities per measurement site produced from data only from the MDM. The indicated discrimination line yields a sensitivity of 90.7% and a specificity of 38.5%. Measurements below this line are assumed non-neoplastic. There are 14 measurement sites below the threshold, 10 sites are non-neoplastic and 4 are neoplastic confirmed by histopathology. HRME data is utilized in the combination methods with measurements

above this line. ROC curves and performance metrics were computed from the

combination of posterior probabilities from all measurement sites.

Combination Method	AUC	% inc. over MDM	Se	% inc over MDM	Sp	% inc. over MDM
1. Maximum posterior probability.	.830	+5.16	76.7	-14.7	84.6	+119.8
2. Minimum posterior probability.	.828	+4.99	76.7	-14.7	88.5	+129.8
3. Mean posterior probability.	.832	+5.44	76.7	-14.7	84.6	+119.8
4. LOP. Weighted sum of posterior probabilities, weights determined from individual AUC for devices.	.832	+5.50	76.7	-14.7	84.6	+119.8
5. LOP. Weighted sum of posterior probabilities, weights determined from search. $W_{MDM}=.89$, $W_{HRME}=.11$	.847	+7.37	86.1	-4.4	80.8	+109.8
6. LOGP. Product of posterior probabilities.	.830	+5.22	76.7	-14.7	84.6	+119.8
7. LOGP. Weighted Product of posterior probabilities, weights determined from search. $W_{MDM}=.87$, $W_{HRME}=.13$	.833	+5.56	83.7	-6.98	80.8	+109.8
8. Weights determined for device and class.	.827	+4.82	76.7	-14.7	84.6	+119.8
9. MDM posterior probability used as HRME prior probability.	.827	+4.88	76.7	-14.7	84.6	+119.8
10. MDM posterior probability used as feature in HRME classifier.	.809	+2.58	84.6	-5.98	75.0	+94.8
11. One classifier using features from both devices.	.818	+3.74	74.4	-17.3	84.6	+119.8

Table 5-2 : The combinatorial methods and the performance achieved. The MDM was used to identify measurement sites with a greater than 90.7% probability of being neoplastic and the HRME was used to measure only these sites. The percent increase in AUC, sensitivity, and specificity values over the MDM alone are shown. The sensitivity of the MDM by itself was 90.7%, the specificity was 38.5%, and the AUC was .789. Method 5 produced the highest increase in AUC.
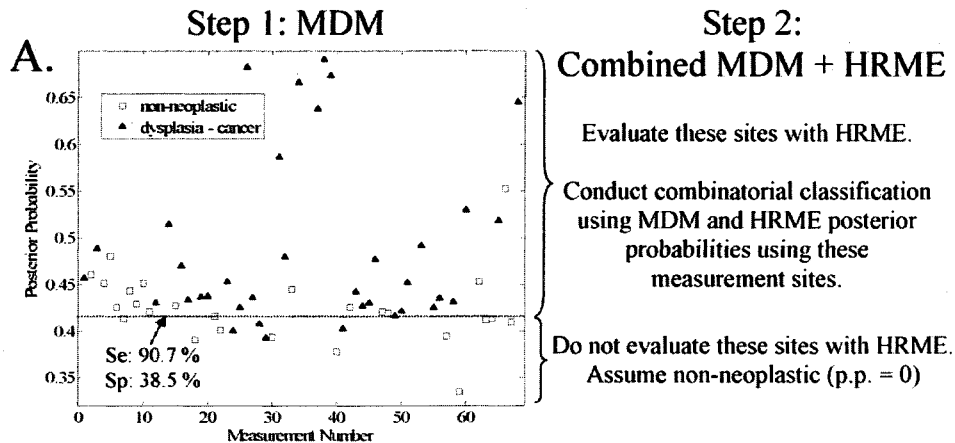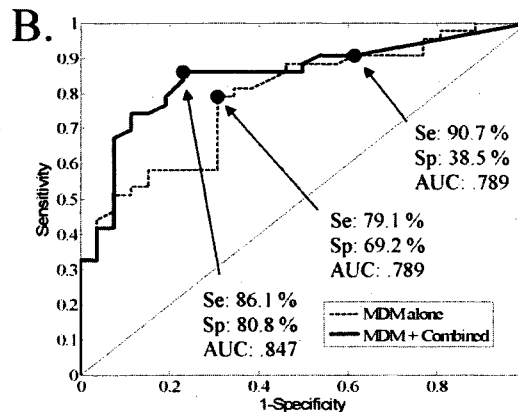
Figure 5-3: Results from the Directed Combinatorial Technique: when the MDM is first used to identify measurement sites with a sensitivity of 90%, and then the HRME is used to aid diagnosis of these measurement sites. 5-3a. Scatterplot of posterior probabilities per measurement site produced from data only from the MDM. The indicated discrimination line yields a sensitivity of 90.7% and a specificity of 38.5%. Measurements above this line are tested using the HRME. Measurements below this line are assumed non-neoplastic and assigned a posterior probability of 0. 5-3b.

ROC curves produced by the MDM alone and from the 2 step method described. The AUC increases from .789 to .847 using this two step method. The qpoint is indicated on both ROC curves. The operating point yielding 90.7% sensitivity is also shown on the ROC produced from the MDM alone.

The highest AUC from the Directed Combinatorial Technique was achieved using the weighted linear opinion pool of posteriors probabilities from each device (Table 5-2). The same weights used for both the Directed and Nondirected Combinatorial Techniques. Figure 3B shows the ROC curves produced by the MDM alone and from the Directed Combinatorial Technique. The AUC increases from .789 to .847 using this method. The sensitivity drops from 90.7% to 86.1%. The specificity increases from 36.5% to 80.8%. The qpoint is indicated on both ROC curves. The operating point yielding 90.7% sensitivity is also shown on the ROC produced from the MDM alone.

The highest AUC produced from the Nondirected Combinatorial Technique was .875 whereas the highest AUC achieved from the Directed Combinatorial Technique was .847. Data from 14 (20.3%) fewer measurements sites were required from the HRME for the Directed Combinatorial Technique.

5.4 Discussion

In this study, image data from two optical imaging devices were combined to make a quantitative, objective classification algorithm to distinguish between neoplastic and non-neoplastic oral mucosa. Both of the combination strategies improved

classification performance over either device alone. The non-directed combinatorial technique yielded a 10.9% increase in AUC over the MDM alone and a 16.4% increase over the HRME alone. In addition to the combination of physically different measurement data provided by two different imaging modalities, independent imaging systems allow for the development of classification algorithms tailored to provide a desired sensitivity or specificity value. The Directed Combinatorial Technique described in this paper used the wide field imaging data alone, with a decision line set at 90% sensitivity as an initial screen. The abundant false positives remaining after this screen were reduced in a second step using combined wide field and high resolution imaging data. The selection of 90% sensitivity during the initial screen was made so that most of the true positives would be captured while the number of measurements sites to be measured by the HRME is reduced. While the final result following the second screen did not achieve a 90% sensitivity (impossible unless the second method was able to classify with a 100% sensitivity at a nonzero specificity), the combined result still yields a significant improvement, 7.4% increase in AUC, over the MDM alone. Additionally, the final sensitivity at the Qpoint was higher and more reflective of the initial sensitivity threshold for the Directed Combinatorial Technique compared to the Nondirected (86.1% sensitivity for the Directed compared to 74.4% for the Nondirected). These results compared well to the weighted LOP classification results from the Nondirected Combinatorial Technique, but allows the user to better control the desired prediction efficiency, and in this case required measurement 20.3% fewer sites with the HRME.

In a previous *in vivo* study using the MDM a sensitivity of 100% and specificity of 91.4% was achieved for discriminating neoplastic from non-neoplastic tissue [122].

The MDM performance was significantly worse in this study which yielded a sensitivity of 79.1% and a specificity of 69.2%. These differences may be due to the changes in resected specimens compared to *in vivo* tissue. Qualitative comparisons of the same tissue *in vivo* and *ex vivo* show differences in autofluorescence intensity which may correlate with the cessation of blood flow and other biochemical changes. Quantitative screening tools, such as the combinatorial wide field and high-resolution imaging algorithm presented in the text, offers clinicians an objective means of examining the oral cavity. Since this technique requires minimal input from the user and a carries a very low per-use cost, higher volume and more frequent screening could be implemented, with the goal of discovering neoplastic lesions of the oral cavity at an earlier, more treatable stage. Such early diagnosis would enable more conservative, tissue-sparing treatment options, with a better overall outcome for the patient.

Chapter 6: High-resolution imaging in Barrett's Esophagus: a novel, low-cost endoscopic microscope[4]

6.1 Abstract:

Background: This report describes the clinical evaluation of a novel, low-cost, high-resolution endoscopic microscope for obtaining fluorescent images of the cellular morphology of the epithelium of regions of the esophagus with Barrett's metaplasia. This noninvasive point imaging system offers a method for obtaining real-time histological information during endoscopy.

Objective: The objective of this study is to compare images taken with the fiber-optic endoscopic microscope with standard histopathology.

Design: Feasibility study

Setting: The University of Texas M.D. Anderson Cancer Center Department of Gastroenterology.

Patients, Interventions, and Main Outcome Measurements: The tissue samples studied in this report were obtained by endoscopic resection from patients with previous diagnoses of either high grade dysplasia or esophageal adenocarcinoma.

Results: Three distinct tissue types were observed *ex vivo* with the endoscopic microscope: normal squamous mucosa, Barrett's metaplasia, and high grade dysplasia.

Squamous tissue was identified by bright nuclei surrounded by dark cytoplasm in an ordered pattern. Barrett's metaplasia could be identified by large glandular structures with intact nuclear polarity. High grade dysplasia was visualized as plentiful, irregular glandular structures and loss of nuclear polarity. Standard histopathology of study samples confirmed the results obtained by the endoscopic microscope.

Limitations: The endoscopic microscope probe had to be placed into direct contact with tissue.

Conclusions: It was feasible to obtain high-resolution histopathologic information using the endoscopic microscope device. Future improvement and integration with wide field endoscopic techniques will aid in improving the sensitivity of detection of dysplasia and early cancer development in the esophagus.

6.2 Introduction

Barrett's Esophagus (BE) is characterized by the replacement of the normal squamous epithelium of the esophagus by a specialized, metaplastic columnar mucosa. A result of chronic gastroesophageal reflux disease, BE is significant because of a drastically increased risk for the development of esophageal adenocarcinoma (EAC). Indeed, subjects with BE carry a risk of EAC up to 125 times greater than the average person[127]. EAC itself is one of the most rapidly rising cancers in the United States having undergone a 5 to 10% increase in incidence per year over the last 30 years[128, 129]. Despite increased awareness, survival rates for EAC remain a dismal 10-25%, an outcome largely due to diagnosis at an advanced stage.

In an effort to improve these statistics, much work has been focused on the early detection of EAC, through the diagnosis of high-grade dysplasia or minimally invasive (intramucosal) adenocarcinoma. However, the detection of this early neoplasia is technically challenging. On standard white-light endoscopy, dysplasia and early EAC are often focal, flat and difficult to consistently distinguish from regular metaplasia . Moreover, the current standard of esophagogastroduodenoscopy (EGD) with random, 4-quadrant biopsies has been shown to miss nearly 2/3 of dysplastic lesions[130-132]. Therefore, there is a demand for minimally-invasive techniques which can detect dysplasia or cancer at an early stage. Such early detection will not only improve survival rates, but also facilitate the application of less-morbid alternatives to esophagectomy, such as endoscopic mucosal resection (EMR).

Several recent optical technologies have sought to increase the detection of neoplasia, at both low and high-resolution. Among the lower resolution (so-called 'widefield' technologies), autofluorescence endoscopy (AF) and narrow-band imaging (NBI) have been the best studied to date. While both of these modalities, have been shown to increase the detection of high grade dysplasia and early adenocarcinoma, specificity has not been impressive[133-139]. This is in part due to esophagitis and inflammatory confounders and other reactive epithelial alterations which can increase the number of false-positives.

In order to improve upon current specificity rates among these new endoscopic imaging modalities, the use of complementary high-resolution technologies, capable of subcellular imaging, has been proposed. One of the most promising of these high-resolution techniques is confocal endomicroscopy[140]. Indeed, a recent study by

Kiesslich et al. found high sensitivity and specificity rates for the detection of HGD/intramucosal EAC, when a confocal endoscope was used with fluorescent contrast agents [75, 141]. While use of such a device may be ideal in an academic or tertiary care-setting where the prevalence of neoplasia is high, cost and the necessity for a separate system may preclude its translation to the community. Indeed, in a community-based, average-risk surveillance setting, a low-cost, probe-based device, compatible with any standard endoscope, may be preferable.

In this paper, we describe a novel, low-cost imaging device developed in our laboratory. Our endoscopic microscope is based on the use of a flexible, small-caliber, fiber-optic image guide bundle. This fiber bundle, 1 millimeter in diameter, can be inserted into the biopsy channel of any standard endoscope, and is capable of fluorescence imaging at subcellular resolution[102]. Perhaps most appealing is the fact that the current prototype consists of less than $2500 in components and uses a 1-2 mm outer diameter probe which can be inserted into the biopsy channel of an endoscope, then sterilized and reused. This further reduces the cost of each application of the device, making it an ideal technology for community-based application.

6.3 Patients and methods

6.3.1 Patients

Patients who participated in this study had been previously diagnosed with either high-grade dysplasia or intramucosal adenocarcinoma, and were scheduled for upper endoscopy with either jumbo biopsies or endoscopic mucosal resection (EMR) of the affected areas. The study protocols were approved by both the Rice University

Institutional Review Board and the University of Texas M.D. Anderson Cancer Center

Institutional Review Board, and informed consent was obtained from each patient before

the procedure. Eleven sequential patients with a documented history of Barrett's

esophagus were approached for enrollment. One patient was excluded due to inability to

perform the EMR (non-lifting); the remaining ten were imaged using the endoscopic

microscope and topical acriflavine.

For each patient, there were typically one to two samples obtained, and

approximately 5 to 10 measurement sites on each sample. Images presented in this paper

are typical for high quality specimens.

6.3.2 Methods

For this study, EMR specimens or 4 mm jumbo biopsies were obtained by a

single endoscopist (S.A.) from patients with Barrett's dysplasia or esophageal

adenocarcinoma. Optical images were obtained immediately after application of topical

acriflavine (see Contrast Agent). Following imaging, the EMR samples and biopsies were

submitted to a single expert GI pathologist (D.M.) for interpretation and the optical and

histopathologic images reviewed. Over 100 optical images were obtained and reviewed.

6.3.3 The Fiber Bundle Microscope

The endoscopic microscope used in this study consisted of a 3 meter long image

guide with 30,000 individual fibers. The spacing of the individual fibers largely

determines the spatial resolution of the endoscopic microscope; in this case, the center-to-

center spacing was approximately 4 microns. The field of view of the system depends on

the diameter of the active area of the fiber bundle; in this case, a circular field of view

with a diameter of 750 microns was produced. Images were produced by placing the

distal surface of the fiber bundle into direct contact with the tissue to be interrogated. The

image guide can be easily passed through the biopsy port of a standard endoscope (Figure

6-1). Illumination was provided by a blue LED centered at 455 nm, which produced an

illumination intensity of approximately 1 mW at the distal end of the fiber bundle.

Fluorescent light returning through the bundle was directed to a scientific-grade CCD

camera coupled to a PC. Images are displayed at a typical frame rate of 2 to 4 frames per

second. The images presented in this paper appear as they would to a clinician viewing

the monitor in a real-time setting.

6.3.4 Fluorescent Contrast Agent

Acriflavine hydrochloride was used as a topical contrast agent and was applied to

tissues prior to imaging. Acriflavine has been shown to localize to the nuclei of cells,

with minimal nonspecific cytoplasmic staining. A solution of 0.05% (w/v) acriflavine in

buffered saline was applied with a cotton swab to the mucosa of each EMR specimen or

biopsy prior to imaging. The acriflavine was placed on the specimen for 30 seconds,

which was then rinsed with buffered saline to eliminate any unbound dye. Imaging was

performed immediately following labeling.

6.3.5 Criteria for interpretation of images

The criteria applied to interpret endoscopic microscope images were based on

differential histologic characteristics of tissue. These include well-established features

seen on light microscopy of standard histologic sections and previously published criteria for scanning confocal microscopy[141, 142]. The criteria used for light microscopy and confocal microscopy were utilized to identify the tissue type and evaluate the architectural and cytologic alterations.

c.

d.
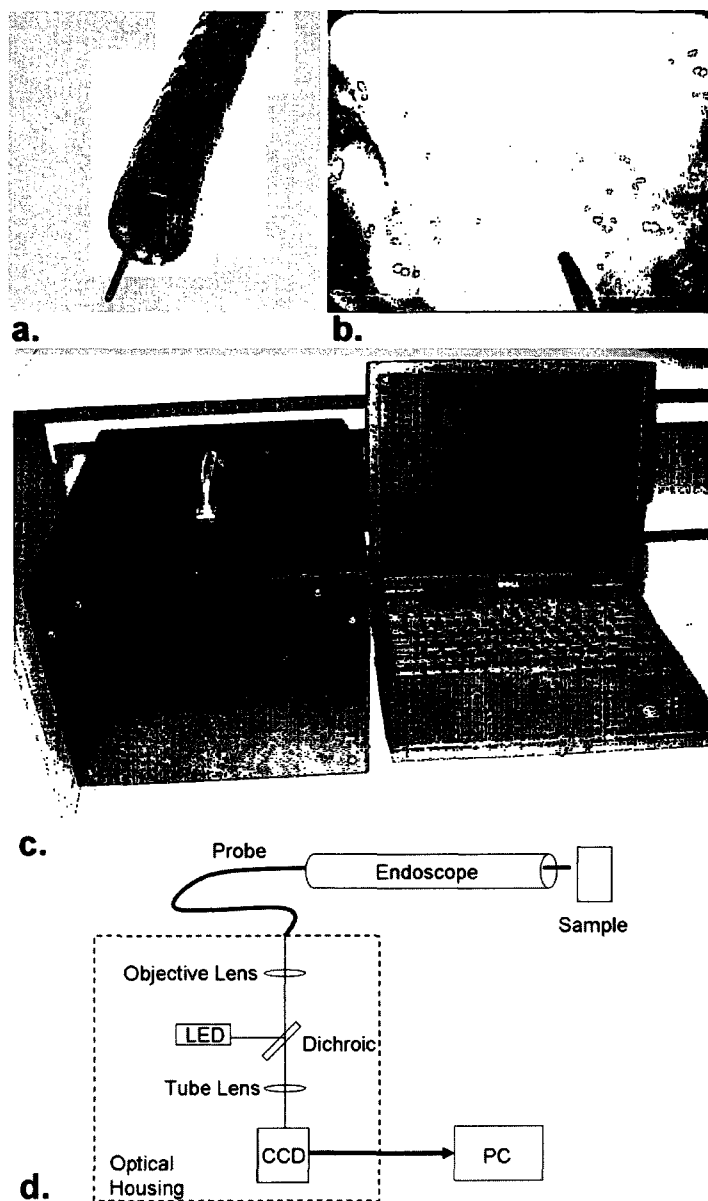
Figure 6-1: Endoscopic Microscope. 6-1a. Image of fiber bundle extending through the biopsy port of a standard white-light endoscope. 6-1b. Image of fiber bundle probe *in vivo*. 6-1c. Image of table-top endoscopic microscope;

fluorescence microscope unit is on the left, data-acquisition PC is on the right.

6-1d. Schematic overview of the system.

The non-neoplastic squamous mucosa is identified on histologic sections by its flat multilayered arrangement with polyhedral cell shapes, well defined cell membranes and centrally situated nuclei with regular internuclear distances. The invaginating lamina propria (papillae) are identified as extensions of lamina propria- composed of loose connective tissue with thin walled blood vessels- into the squamous epithelium at regular intervals. On confocal microscopy the cytologic characteristics of squamous epithelium is essentially identical to histology with polygonal cell shapes with well defined cell membranes and centrally situated nuclei; the latter two identified by their bright color as compared to the darker cytoplasm. Flat multilayering is assessed by the unaltered shape of the epithelial arrangement at progressively deeper optical sections of the mucosa. The papillae are identified as a circular dark area with the presence of scattered small bright structures corresponding to the connective tissue, red blood cells and inflammatory cells. The presence of intraepithelial inflammation is identified by inflammatory cells, which are seen as bright oval to round structures which are haphazardly distributed in the epithelium.

Barrett's esophagus (intestinal metaplasia) is identified on histology by the presence of villiform architecture, columnar enterocytes and goblet cells. The criteria used for confocal microscopy includes the presence of round double layer ring (torus) structures which alter their shapes at different optical thicknesses. At deeper levels the ring-like structures show the classic villiform architecture. The villi are lined by the

columnar enterocytes with bight nuclei and dark cytoplasm. The lamina propria in the core of the villi shows a similar appearance to the squamous papillae with blood vessels and inflammatory cells. At cellular levels the presence of goblet cell is identified by clear to dark blue globules admixed with the columnar enterocytes. The border of the goblet cells is particularly bright in good quality images. In non-dysplastic Barrett's mucosa the intervillous stroma is abundant and identified by the presence of loose connective tissue, inflammatory cells and blood vessels. In highly dysplastic Barrett's mucosa the villous architecture is either effaced or completely lost. In addition, at different optical thicknesses the architecture is uniform with complex back-to-back arrangements of small glandular structures with minimal intervening stroma. The cytologic alterations, like multilayering of the cells, bright nuclear appearance, decreased goblet cells and high nuclear-to-cytoplasmic ratios are also applied to identify high-grade dysplasia. Another feature seen in good quality images is the structural relation of epithelium and subepithelial capillaries. In non dysplastic Barrett's mucosa the capillaries are regular and seen at upper and mid level thicknesses. However, in highly dysplastic mucosa the capillaries are seen only at deeper levels and show variations in size and shape.

. Each image was analyzed independently and in a blinded fashion by both a gastrointestinal pathologist and a gastroenterologist. Endoscopic microscope images were then correlated with the standard histopathologic images, previously interpreted by the GI pathologist.

6.4 Results

Images obtained with the endoscopic microscope were compared to histopathologic interpretation of the same areas. Fluorescence images were evaluated qualitatively, noting nuclear size and density, nuclear-to-cytoplasmic ratio, glandular structure and organization, and intensity of fluorescence. Distinct patterns of fluorescence images were observed for tissues with different histopathologic diagnoses: (1) normal squamous epithelium, (2) Barrett's metaplasia/low grade dysplasia, and (3) Barrett's neoplasia (high grade dysplasia or intramucosal adenocarcinoma).

6.4.1 Normal squamous tissue

Figure 6-2 shows histologic and endoscopic fluorescence microscopy images of normal squamous mucosa obtained from a site which appeared normal on white light endoscopy. The biopsy fragment was also imaged with a commercial fiber optic confocal endoscope (Pentax/Optiscan), and a standard commercial benchtop confocal system (Zeiss LSM 510 Meta). Both the fiber optic confocal system and the benchtop confocal microscope used an excitation wavelength of 488 nm.

Individual cell nuclei are easily visible as discreet bright dots in fluorescence images obtained with the endoscopic microscope and the two confocal systems (Figure 6-2). The field of view of the endoscopic microscope is much larger than the two confocal systems while the spatial resolution is somewhat decreased In addition, the frame rate of the endoscopic microscope (2 to 4 frames per second) is faster than that of the commercially available confocal endoscope (0.8 frames per second). The squamous epithelium is distinguished by its multilayering, polyhedral/polygonal shape and centrally

situated nuclei and well defined cell membrane. Uniform spacing of the nuclei indicates

the intact polarity which distinguishes benign squamous mucosa. This also helps in

differentiating other, more randomly distributed cells (e.g. inflammatory cells) which

might infiltrate the epithelium.
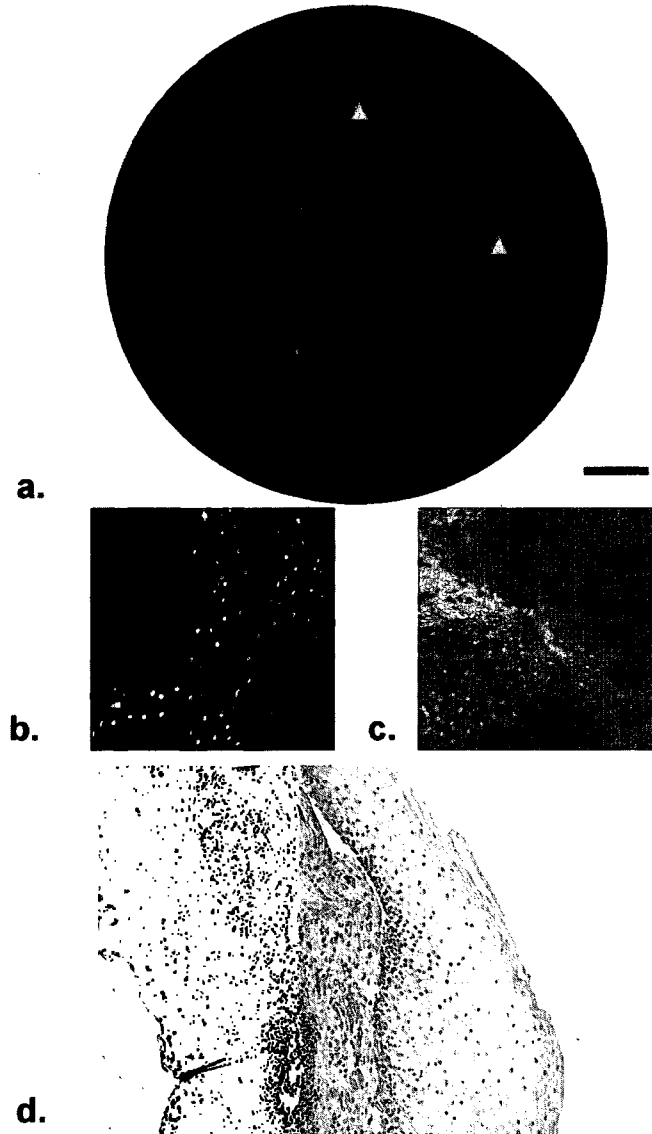
Figure 6-2: Images of normal squamous tissue. 6-2a. Endoscopic microscope image of normal squamous tissue stained with 0.05% acriflavine. 6-2b. Benchtop confocal (Zeiss LSM 510 Meta) image of same tissue. 6-2c. Pentax endoscopic confocal image of same tissue. 6-2a-c show flat arrangement of squamous epithelium with round regularly

spaced nuclei. The round clear spaces surrounded by the epithelium represent the papillae (red arrowhead). The acriflavine in image 6-2a highlights the nuclei. 6-2d. Histopathology of same specimen. Scale bar is 100 microns.

6.4.2 Barrett's metaplasia

Endoscopic microscope imaging was performed at several sites on EMR specimens labeled topically with acriflavine. Two sites are described in this paper (Figure 6-3). The endoscopic microscope image in Figure 6-3a shows glandular epithelium characterized by double ring-like architecture with bright density distributed uniformly along the basement membrane consistent with intact nuclear polarity. In addition, the nuclei are uniformly distributed in the epithelium away from the basement membrane. These features are consistent with non-dysplastic glandular mucosa.

The image in Figure 6-3b shows similar features as Figure 6-3a except for a small area of focal complex architecture, the significance of which is uncertain as the nuclear arrangement is that of non-dysplastic glandular epithelium described in Figure 6-3a This image is also consistent with Barrett's without dysplasia. The hematoxylin-eosin stained section of the same specimen in Figure 6-3c shows distinctive type Barrett's mucosa, histologically defined as intestinal metaplasia. The intestinal metaplasia is characterized by the presence of goblet cells, easily identified by intracytoplasmic clear-to-light blue vacuoles. These features are consistent with Barrett's metaplasia.
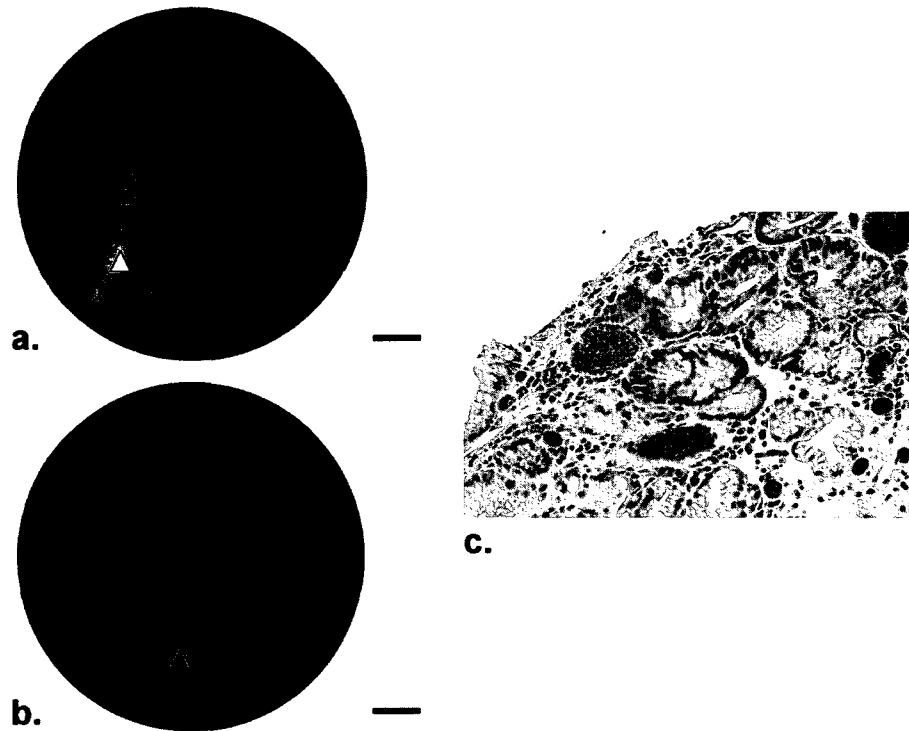
Figure 6-3: Images of Barrett's metaplasia. 6-3a. and b. Endoscopic microscope of Barrett's metaplasia stained with 0.05% acriflavine. Image 6-3a shows broad villous architecture. The bright band at the base of each villous-like structure indicates the high uptake of acriflavine by the nuclei (yellow arrowhead). Image 6-3b shows larger torus-like structures with intervening stroma. Occasional goblet cells are highlighted by a marker (red arrowhead). 6-3c. Histopathology of same sample. Scale bars are 100 microns; all images at the same scale.

6.4.3 High grade dysplasia

Endoscopic microscopy and histopathologic images taken from an EMR specimen with HGD are shown in Figure 6-4a and b, respectively. Figure 6-4a shows a confluent proliferation of small glandular structures with variable size and shape with occasional areas showing a gland-in-gland appearance. High nuclear density along with a large component of cells occupied entirely by nuclei indicate high nuclear-to-cytoplasmic ratio. These features are consistent with high-grade dysplasia.

The hematoxylin-eosin stained section of the specimen shows distinctive type Barrett's mucosa with high-grade dysplasia, consistent with the features observed in the fluorescence image. The high-grade dysplasia is characterized by architecturally complex arrangement of the glands and loss of nuclear polarity, nuclear overcrowding, and nuclei and mitotic figures reaching up to the lumenal surface.

a. — b.
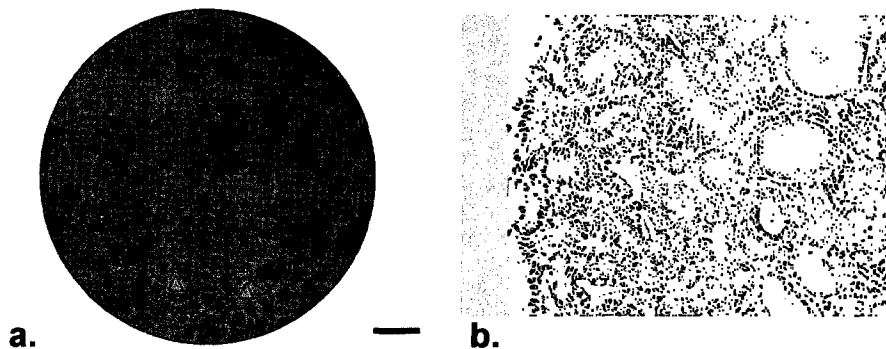
Figure 6-4: Image of high-grade dysplasia. 6-4a. Endoscopic microscope image of high grade dysplasia stained with 0.05% acriflavine. Confluent and haphazard glandular proliferation with back-to-back arrangements and minimal to absent stroma. Foci of high nuclear intensity and high nuclear-to-cytoplasmic ratio are highlighted by markers (red arrowheads).

6-4b. Histopathology of same specimen. Scale bar is 100 microns; all images are at the same scale.

6.5 Discussion

This study demonstrates the ability of an inexpensive (< \$2500) system with a reusable probe to produce high-resolution images of a variety of esophageal tissue types. Such a device can easily be integrated into any standard endoscope to non-invasively yield subcellular-resolution images of the surface histology of a suspected lesion with the use of an appropriate fluorescent dye. Coupled with wide-field imaging devices, this endoscopic microscope system should further enhance specificity for detection of Barrett's neoplasia. This low-cost device has advantages over more complex 'optical biopsy' systems because of its easy application to a wide variety of settings and platforms. The probe itself can be disinfected and reused, further reducing the cost of each use of the device. Moreover, the straightforward optical design is highly robust and requires no scanning mirrors or other moving parts, enabling such technology to disseminate to areas with high levels of support as well as regions with less infrastructure and resources.

Non-invasive visualization of the cellular architecture enables a clinician to more thoroughly inspect the mucosa, and diagnose and treat intraepithelial neoplasia immediately. The strength of our study is the application of well-established, age-old pathologic criteria to interpret the optical images. Ideally, the real-time interpretation of such images will involve close collaboration between a gastroenterologist and GI pathologist. As has been shown with the interpretation of confocal endomicroscopic

images, gastroenterologists can be trained to interpret optical images and distinguish 2 pathologic classifications: Barrett's metaplasia/low grade dysplasia and Barrett's high grade dysplasia/intramucosal adenocarcinoma. A larger study with robust kappa statistics for interobserver reproducibility is planned for validation of this concept with this device. Additionally, work is underway to develop algorithms based on standard pathologic criteria (nuclear:cytoplasmic ratio, etc.) which can be translated into rapid, real-time, image-processing and interpretation software.

From a clinical management standpoint, the diagnosis of Barrett's HGD or intramucosal adenocarcinoma is the most critical distinction. Given the large interobserver variability in the interpretation of low-grade dysplasia and the subtle architectural and morphologic features which characterize LGD, we feel that the identification of LGD may be beyond the capabilities of this technology. However, given the low likelihood of progression of LGD, we do not believe this is significant drawback. To further enhance the sensitivity and specificity of the technology for the detection of HGD/intramucosal cancer, we are currently working on combining high-resolution fluorescence imaging with other molecular-specific techniques (eq. optical contrast agents targeted to epithelial biomarkers).

In order to achieve the high frame rates and good image quality seen in images from this device, selection of a bright, selective fluorescent dye is critical. Acriflavine hydrochloride, previously used as a topical antiseptic, was chosen for its ability to cross cell membranes and label acid molecules, including DNA. Acriflavine has been used in a number of European and Australian *in vivo* imaging studies of the gastrointestinal epithelium, as well as other studies, without any reported adverse effects[32, 75, 143,

144]. While acriflavine displays some affinity for collagen and elastin and some residual staining occurs in the cytoplasmic regions of cells, strong contrast is observed between cell nuclei and the surrounding cytoplasm. This enables qualitative observation of the cellular architecture of squamous and glandular patterns, as well as providing an estimate of nuclear-to-cytoplasmic ratios. Topical acriflavine also stains only the superficial layers of tissue, and has been shown to have limited effect below the lamina propria[75]. Since the contact imaging procedure used in the endoscopic microscope does not perform optical sectioning and does not reject fluorescent light as efficiently as a confocal microscope, superficial labeling improves image detail.

There have been recent advances in the use of molecular-specific contrast agents. These agents consist of an optical reporter conjugated to a monoclonal antibody, aptamer, or other targeting ligand, and have been successfully implemented for the detection of abnormal expression levels of cell surface markers, including epidermal growth factor receptor (EGFR)[62]. These fluorescent contrast agents can be used with existing high-resolution point imaging devices to yield both qualitative and quantitative data about the nature of neoplastic disease. In addition, the response of a particular tumor to a given therapy could be monitored over time in a non-invasive fashion.

In conclusion, we have developed a **low-cost** fiber bundle-based high-resolution imaging system which is capable of visualizing cellular architecture, morphology, and nuclear-to-cytoplasmic ratios. Preliminary *ex vivo* evaluation shows that this system can differentiate between squamous mucosa, Barrett's metaplasia, and Barrett's intraepithelial neoplasia. Through the use of image processing techniques and segmentation of individual cell nuclei in images collected from the endoscopic

microscope, it will be possible to provide a quantitative estimate of nuclear-to-cytoplasmic ratios[102]. Future development and automation of such image processing software will lead to objective surveillance algorithms that can assist the endoscopist in locating dysplastic lesions. The use of such a translatable system in concert with existing and developing wide-field endoscopic technologies may facilitate improved specificity for the detection of Barrett's neoplasia and further clinical evaluation of this technology is forthcoming.

Chapter 7: Detection of esophageal adenocarcinoma and its precursors with a high-resolution microendoscope[5]

7.1 Abstract

Background and study aims: Early detection of dysplasia in patients with Barrett's metaplasia is essential to improved survival. The aim of this study was to evaluate the ability of high-resolution microendoscopic imaging to identify neoplastic lesions in patients with Barrett's esophagus.

Patients and methods: Nine patients with previously diagnosed Barrett's esophagus with and without dysplasia underwent standard screening biopsies or endoscopic mucosal resection. Fresh tissue was imaged with the microendoscopy system; images were analyzed by visual interpretation or by quantitative image analysis to predict whether the imaged sites were non-neoplastic (Barrett's only or Barrett's with low grade dysplasia) or neoplastic (high grade dysplasia or esophageal adenocarcinoma). Predictions were compared to histopathology.

Results: Subjective analysis of the images by a single expert clinician achieved sensitivity and specificity of 83% and 66%, respectively, while the quantitative classification algorithm achieved a sensitivity and specificity of 87% and 85%, respectively, when compared to histopathology.

Conclusions: This pilot study demonstrates that a simple microendoscope device can yield clinically useful, objective information about the presence of neoplasia in patients with Barrett's esophagus.

7.2 Introduction

The incidence of esophageal adenocarcinoma (EAC) has increased six-fold in the United States over the past 30 years [145]. Cancer of the esophagus has one of the poorest overall five-year survival rates of all cancers. Reported five-year survival rates for patients with treatable esophageal adenocarcinoma are 14% and 0% for Stage II and IV disease, respectively [146]. Surgical treatment for locally advanced EAC is often invasive and carries significant risk. Early detection of disease is vital for improving long-term survival rates as well as the overall quality of life of affected patients.

Traditional white light endoscopy does not provide sufficient information to detect the presence of very early dysplasia in regions of Barrett's metaplasia [147]. High-resolution examination of tissue by histopathology is required; the current standard of care for surveillance of the esophagus following a diagnosis of Barrett's metaplasia involves taking four quadrant biopsies per centimeter over the length of the affected area. This sampling however, has been shown to have minimal effect on overall clinical outcome. [131, 132].

Recent advances in endoscopic examination techniques have shown promise in detecting dysplasia in Barrett's metaplasia, before the onset of invasive carcinoma. Wide field imaging techniques have the advantage of surveying large areas of mucosa during a single procedure. Narrow band imaging (NBI) is a technique which uses select regions

of the visible light spectrum which are favorably absorbed by hemoglobin [137, 138]. As a result, glandular and vascular patterns within a region of Barrett's metaplasia can be closely inspected for irregularities suggestive of early dysplasia. Another important new endoscopic imaging modality is autofluorescence (AF) visualization. In this technique, blue excitation light is used to illuminate the tissue, and long wavelength emission light is recorded by the imaging sensor [135, 148]. The autofluorescence signal contains information about the structure and biochemical components of the tissue, and is decreased in regions of dysplasia, allowing the clinician to survey large areas during a single examination.

While these new methods have improved the rate of detection of adenocarcinoma in the gastrointestinal tract, they have demonstrated relatively poor specificity due to inflammation and other confounding factors [149]. To augment these techniques and improve the overall specificity of detection of EAC and its precursors, high-resolution imaging modalities can yield information at the cellular level, allowing the clinician to distinguish between dysplasia and inflammation or other reactive changes [150]. Confocal laser endoscopy (CLE) is an emerging technology which consists of a miniaturized single-fiber confocal microscope embedded in the distal end of a white light endoscope [31, 32]. CLE yields images with submicron resolution of the esophageal mucosa in real-time during an endoscopy procedure. This instantaneous feedback allows the clinician to directly examine in detail those regions that appear abnormal under wide-field inspection.

Complementary CLE with advanced wide field imaging techniques offers potential to improve early detection of dysplasia in Barrett's esophagus. However, at the

present time, this technology is expensive and available primarily in tertiary care centers. In addition, CLE requires subjective interpretation of the images by the endoscopist, which requires extensive training and is subject to intraobserver variability [151-153]. To extend the benefits of high-resolution imaging to a broader patient population, and to create a more objective means of evaluating optical biopsy data, we developed a High-Resolution Microendoscope (HRME) device that is capable of producing images of the esophageal mucosa at sub-cellular resolution without the need for expensive optics or scanning electronics . In a previous study of resected Barrett's tissue, HRME images could distinguish between non-dysplastic glandular architecture and dysplastic regions [103].

The goal of the study presented in this paper was to further explore use of the HRME system to distinguish between neoplastic and non-neoplastic Barrett's. Subjective analysis of HRME image data by expert clinicians was compared to an objective, computer-aided classification algorithm developed to differentiate Barrett's metaplasia from high grade dysplasia and cancer.

7.3 Methods

7.3.1 Patients

Patients over 18 years of age with a previous diagnosis of Barrett's metaplasia of the esophagus and scheduled for surveillance endoscopy were asked to participate in the study. Informed consent was obtained from all study participants, and the study was reviewed and approved by the Institutional Review Boards at the University of Texas M.

D. Anderson Cancer Center and Rice University. Subjects underwent conventional endoscopy with standard four-quadrant biopsy surveillance; a subset of patients underwent endoscopic mucosal resection (EMR). Following resection, the biopsy or EMR specimens were taken to the lab for imaging.

A solution of Proflavine (Sigma-Aldrich) dissolved in water at a concentration of 0.01% (w/v) was prepared prior to performing imaging. The contrast agent solution was directly applied to the epithelial surface of the tissue with a dropper, and imaging with the HRME device was performed immediately. The application of proflavine does not discolor the tissue surface, and is not detectable in tissue slides prepared using standard histopathology processing and H&E staining (Figure 7-1).

After imaging, the tissue was returned for standard histopathology processing, and slides were later reviewed by a board-certified pathologist (D.M.). Each measurement site used in this study was correlated to a histopathology-confirmed diagnostic category; Barrett's metaplasia without dysplasia, Barrett's with low grade dysplasia, Barrett's with high grade dysplasia, or esophageal adenocarcinoma.

7.3.2 Imaging system

The high-resolution microendoscope (HRME) device has been previously described in detail [102]. Briefly, images are acquired with this device by placing the tip of the fiber bundle image guide into direct contact with the epithelial surface of the tissue. Excitation light from a blue LED with a center wavelength of 455 nm is delivered through the fiber bundle. The fluorescence emission from the topically applied fluorescent contrast agent, proflavine, is collected through the fiber bundle, focused onto

a CCD camera, and a digital image is stored for future processing and analysis. The HRME system has a circular field of view with a diameter of 750 microns; the lateral spatial resolution of the system is approximately 4 microns, and images are displayed at 4 frames per second.

7.3.3 HRME Image Analysis

Digital HRME images were reviewed to determine whether the endoscope tip was in contact with the tissue surface or whether the probe tip moved during image acquisition. Images showing such artifacts were discarded and not used in subsequent analyses.

Digital HRME images passing quality control were reviewed by two expert pathologists and two expert gastroenterologists. The reviewers were shown the images from the entire data set following randomization. Each was asked to score the images as either "neoplastic" or "non-neoplastic," where "non-neoplastic" corresponds to a pathologic diagnosis of Barrett's metaplasia or Barrett's metaplasia with low grade dysplasia, and "neoplastic" corresponds to Barrett's metaplasia with high grade dysplasia or EAC. Results of visual image interpretation were compared to the histopathology-confirmed diagnosis at each site, and sensitivity and specificity were calculated for each observer. The kappa statistic was also computed to measure the inter-observer agreement.

In addition to subjective image interpretation, we explored the diagnostic ability of quantitative image analysis. For each image, fifty-nine distinct features were computed (Table 7-1). First order statistical features (variance, entropy, etc.) were calculated directly from the raw pixel values. A gray-level co-occurrence matrix (GLCM) with pixel offsets from 1 to 10 was used to calculate additional textural feature

groups (correlation, contrast, homogeneity, and energy) [108]. Each GLCM feature group contained 10 distinct features, corresponding to each pixel offset. To detect nuclear features, an extended regional maximum transform was applied to the image. Voronoi tessellations were calculated from the centroids of the nuclear features to calculate internuclear distances [85]. A Fourier transform was applied to each image to calculate the power spectrum; this was divided into 10 partitions to represent the frequency components of the image. The contribution of each partition is represented as a fraction of the total power spectrum [109, 110].

A diagnostic algorithm was developed to classify each image as non-neoplastic or neoplastic using these image features as input. Histopathology again was used as the gold standard; sites with a pathologic diagnosis of Barrett's metaplasia or Barrett's metaplasia with low grade dysplasia were considered to be non-neoplastic, while sites with a pathologic diagnosis of Barrett's metaplasia with high grade dysplasia or esophageal adenocarcinoma were considered to be neoplastic. The classifier was based on two-class, linear discriminant analysis; a sequential forward feature-selection algorithm initially was used to select the best performing subset of up to 10 image features to classify the data. Initially, the best performing single feature was identified, and then subsequent features were selected which gave maximum performance when combined with previously selected features. The algorithm was developed using five-fold cross-validation; each measurement site was initially randomly assigned to one of five groups. Four-fifths of the data were then used to train the linear classification algorithm and the remaining one fifth of the data were used to test the algorithm. This cycle was repeated four additional times so that the algorithm is tested using data from each site.

Performance was monitored by calculating the area under the curve (AUC) of the classifier.

Alternatively, a three-class diagnostic algorithm was developed to classify each image as: (1) Barrett's metaplasia or Barrett's metaplasia with low grade dysplasia, (2) Barrett's metaplasia with high-grade dysplasia, and (3) cancer. A categorical tree-based classifier was used. This algorithm was allowed to choose among the entire feature set [111, 112]. The tree-based classifier was pruned to three terminal nodes to avoid overtraining; two features were selected to perform this step. The predicted classification results from each classifier were then compared to the actual histopathology for each site.

7.4 Results

7.4.1 Patients and measurement sites:

Nine subjects enrolled in the study. Images were obtained from 139 unique sites; images from 128 of these sites passed the QC review and were used for further analysis. Of these 128 sites, 6 were histologically confirmed to be Barrett's metaplasia, 53 were Barrett's with low grade dysplasia (LGD), 26 were Barrett's with high grade dysplasia (HGD), and 43 were esophageal adenocarcinoma (EAC). Figure 7-1 shows representative HRME images (top row) and corresponding histopathology (bottom row) of non-neoplastic (LGD), HGD, and EAC, respectively. All images are at the same scale for comparison. Large, well-organized glands can be seen in the non-neoplastic Barrett's case, while smaller glands with disrupted boarders are visible in the HGD case. The

image of EAC shows extreme disruption of glandular organization and crowded,

abnormal cells.

| Barrett's metaplasia with low grade dysplasia | High grade dysplasia | Esophageal adenocarcinoma |
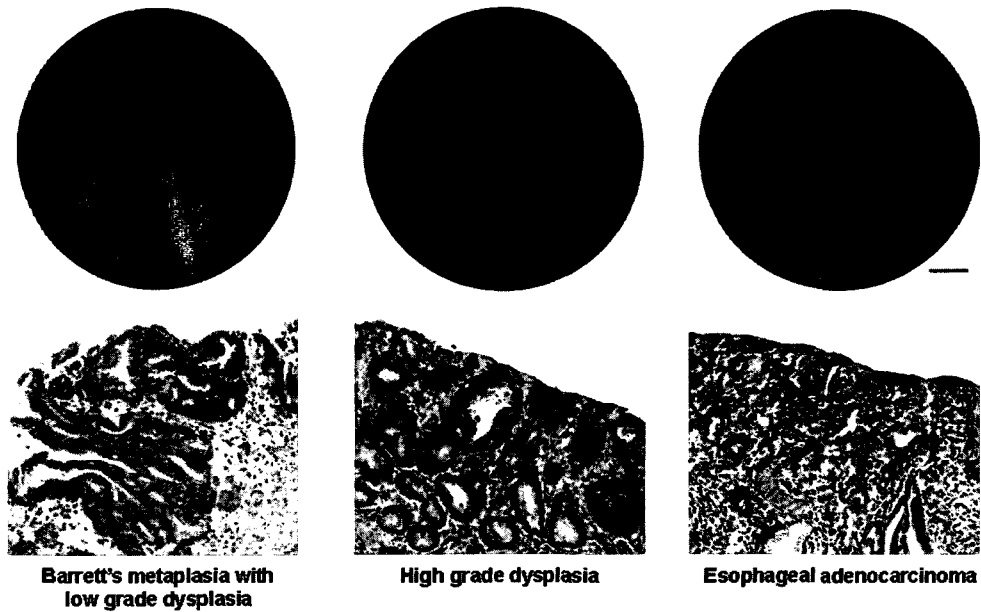
Figure 7-1: Illustration of HRME images (top row) compared to H&E images (bottom row). From right to left, diagnostic categories are: Barrett's metaplasia with low grade dysplasia (LGD), high grade dysplasia (HGD) and esophageal adenocarcinoma (EAC). All images are sized to the same scale; scale bar represents 100 µm.

7.4.2 Subjective image interpretation:

Subjective scoring of the images by an expert gastroenterologist (S.A.) achieved a sensitivity of 83% and specificity of 66%.

7.4.3 Quantitative image feature calculation

Quantitative image features were ranked according to their diagnostic ability. Image features in Table 7-1 are listed in order of descending area under the ROC curve for the single-feature, two-class linear discriminant analysis classifier. The single best performing feature was found to be the GLCM correlation with a pixel offset of 10. Figure 7-2a shows a box plot representing the GLCM correlation values, averaged for each of three major diagnostic categories: Barrett's and LGD, HGD, and EAC. On average, the GLCM correlation level is lower in sites with HGD or EAC when compared to non-neoplastic sites.

Feature	Explanation
Correlation (10 features)	Pixel neighbor correlation over the entire image
Standard Deviation	Standard deviation of grayscale values
Variance	Variance of pixel grayscale values
Energy (10 features)	Sum of squares in gray-level co-occurrence matrix (GLCM)
Frequency (10 features)	Frequency distribution of pixel values
Entropy	Statistical measurement of randomness of grayscale values
Mean Nuclear Separation Distance	Mean nuclear separation as calculated by Voronoi tessellation
Std. Dev. Nuclear Separation Distance	Standard deviation of nuclear separation as calculated by Voronoi tessellation
Nuclei Per Unit Area	Number of nuclei detected divided by area of region of interest
Kurtosis	Measure of the flatness of the pixel value distributions
Skewness	Measure of the symmetry of the pixel value distribution
Contrast (10 features)	Measure of pixel intensity compared to its neighbors over the entire image
Homogeneity (10 features)	Closeness of the distribution of the GLCM elements to the diagonal
Mean Minimum Nuclear Separation Distance	Average minimum nuclear separation as calculated by Voronoi tessellation

Table 7-1: Quantitative image features. The table is in order of performance as roughly estimated by a linear discriminant analysis using one feature and the entire data set for training and testing.

The top performing combination of two features was found to be the GLCM correlation value at an offset of 10 and the frequency contribution at an offset of 6; this is the relative contribution to the total power spectrum coming from the frequencies over the 6th partition from the Fourier transform. Figure 7-2b shows a scatter plot of these two features for each of the 128 sites in the data set. Samples with a pathologic diagnosis of

Barrett's with or without LGD are shown as blue squares, while samples with a pathologic diagnosis of HGD or EAC are shown as red crosses. The decision line calculated using a two-class linear discriminant classifier is shown on the plot.

Figure 7-3a shows the area under the curve as a function of the number of image features selected in the linear discriminant algorithm. The AUC increases from one to two features and reaches a plateau. Figure 7-3b shows a scatter plot of the posterior probability that each site is neoplastic (HGD or EAC) as calculated by the linear classifier; samples are grouped by histopathologic diagnosis. Figure 7-3c shows the ROC curve for the linear discriminant classifier based on these two features. The AUC is 0.92 and the sensitivity and specificity at the Q-point are 87% and 85%, respectively.

The tree-based three-class classifier used automated feature selection. The features chosen by this algorithm were again GLCM correlation and frequency contribution. Table 7-2 summarizes the performance of the three-class algorithm; vertical columns add to 100%, to indicate the proportion of predicted measurements that were placed into the correct category. The tree-based classifier performed very well in distinguishing the non-neoplastic case (93.9%) and when predicting HGD and EAC (73.1% and 75.5%, respectively).
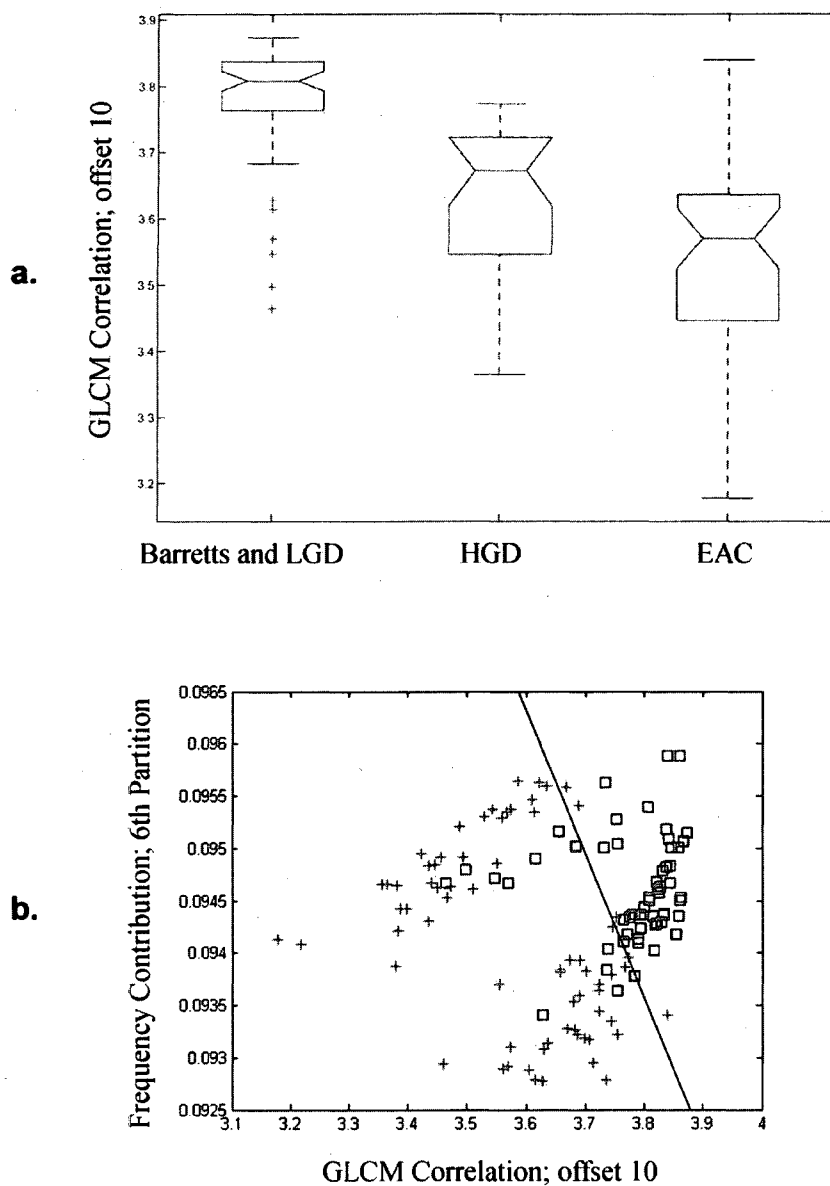
Figure 7-2: Quantitative analysis. 7-2a. Box plot showing the classification utility of GLCM correlation as a single feature. Note the separation between Barrett's metaplasia and LGD compared to HGD and EAC. 7-2b. Measurement sites plotted using two features. Non-neoplastic sites are plotted as blue squares, neoplastic sites are plotted as red crosses. The decision line is shown.

7.5 Discussion

In this study, we demonstrated the use of a simple, low-cost portable microendoscopy system to distinguish between clinically significant classes of intestinal metaplasia, dysplasia and cancer. Subjective image interpretation and an operator-independent image analysis algorithm were both used to differentiate between these categories. Subjective image interpretation demonstrated sensitivity and specificity of 83% and 66%, respectively. The objective classification algorithm was able to distinguish between neoplastic and non-neoplastic cases with a sensitivity of 87% and a specificity of 85%. The results of this pilot study are suggestive that this technique may be useful to regions without highly trained expert personnel or extensive biomedical infrastructure.

Three-Class Tree-Based Classifier Results			
	IM / LGD Predicted	HGD Predicted	EAC Predicted
IM / LGD Actual	**93.9**	**19.2**	**13.2**
HGD Actual	**4.1**	**73.1**	**11.3**
EAC Actual	**2.0**	**7.7**	**75.5**

Table 7-2: Summary of the performance of the tree-based three-class classifier.

As with any small pilot study, a larger sample size will be required to improve the significance of the classification algorithm presented here. Specifically, a large, independent test set should be validated using the algorithm following training on a separate training data set. Such large data set validation will reduce the influence of overfitting of the classification algorithm and yield more reliable performance values.
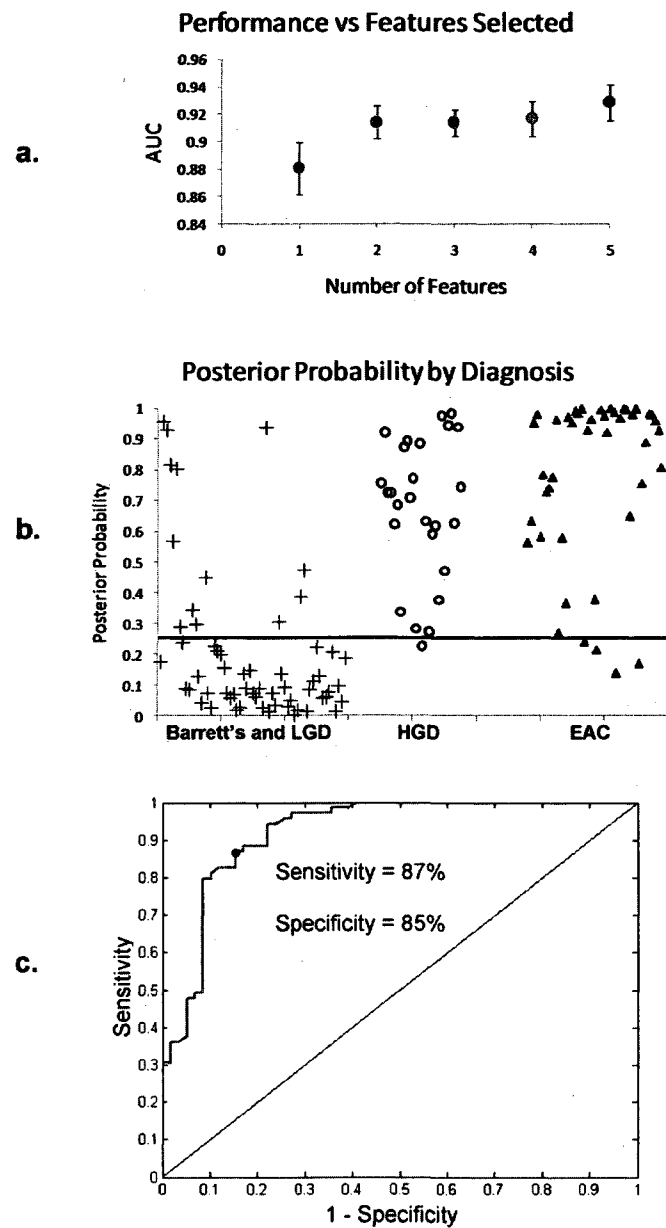
Figure 7-3: Classification performance. 7-3a. Calculated classification performance versus number of features used; note the plateau at two features. 7-3b. Scatter plot of calculated posterior probability generated by a two-feature linear discriminant analysis (LDA) algorithm. The decision

is shown at 0.24. 7-3c. ROC curve of calculated classification performance using the two-class, two-feature LDA. The Q-point is shown corresponding to a sensitivity of 87% and a specificity of 85%.

An additional limitation of this trial is the HRME probe's inability to image subsurface regions. While the incidence of high-risk submucosal or occult EAC is still subject to controversy, inspection of subsurface regions remains an important consideration to clinicians [154]. The current HRME device yields images by placing the tip of the device into direct contact with tissue, limiting its image acquisition to the top layers of epithelium. However, the fiber optic probe is small enough to pass through the lumen of a 16-gauge needle; the needle could be used to physically penetrate into deeper layers of the epithelium, allowing the fiber bundle to image these areas. This technique has been successfully demonstrated in a mouse model.

High-resolution imaging of the gastrointestinal epithelium offers clinicians a means to inspect the histologic features of suspicious lesions and post resection margins in real time during an endoscopic procedure. Such information can be used to guide the selection of sites for biopsy to improve the diagnostic yield during screening endoscopy [155]. Traditional CLE typically requires the endoscopist to interpret images during the procedure. This subjective interpretation is likely highly dependent on clinician training, and is variable by its subjective nature. A more objective means of image interpretation may help guide the endoscopist's decision as to the classification of a lesion. Such objective image analysis has been applied in other high-resolution imaging studies; Becker et al. demonstrated that computer-aided diagnosis of mucosal pit patterns but a

fiber bundle confocal system has been shown to be effective in distinguishing neoplastic from non-neoplastic Barrett's tissue [100].

The image processing techniques presented in this study can uncover features in images that are clinically important, but which may not be apparently to the clinician performing the procedure. In addition, quantitative image analysis and classification techniques require relatively minimal computing time, which is useful in a busy clinical setting. The HRME system and classification algorithm presented in this paper represent a low-cost system that is easily integrated into currently used endoscopy systems and can be operated independent of the clinician's subjective interpretations of images.

Chapter 8: Discussion

8.1 Summary of Findings

The results of the preceding studies have demonstrated that a simple, fiber bundle image guide-based microendoscopy system is capable of employing a number of fluorescent contrast agents in collecting high-quality, high-resolution images of both in vitro cell phantoms, *in vivo* imaging of small animal tissues, and imaging several types of resected human tissue epithelium. Quantitative image processing techniques and objective classification algorithms were also used to help aid in classifying measurement sites in human epithelium as neoplastic or non-neoplastic, a clinically important distinction.

Initial studies presented in Chapter 3 measured the performance of the device, including using a USAF reolution target to verify that the HRME could resolve 4 micron lines. Biological models were then used with the system to demonstrate its flexibility; molecular-specific antibody and quantum dot labeling schemes were successfully used to image cells overexpressing cell surface receptors, including Her-2 and EGFR receptors. A murine tumor xenograft explored the *in vivo* and small animal imaging capabilities of the device, using a hypodermic needle as a guide to place the fiber bundle into the subcutaneous tumor and evaluate its structure at subcellular resolution. Finally, initial imaging results from resected human oral mucosa were presented.

Chapter 4 presents a quantitative means of analyzing microendoscope images of the oral epithelium. Images from resected specimens from 13 patients, comprising 141 independent, histopathology-confirmed measurement sites were analyzed for numerical features. These features included first-order statistics, including pixel gray value variance

and entropy, texture features calculated by a gray-level co-occurrence matrix, frequency

components, and nuclear features, such as inter-nuclear spacing. These features were

used to train and evaluate a linear discriminant algorithm to classify images into

neoplastic (invasive cancer, severe and moderate dysplasia) or non-neoplastic (normal

squamous or mild dysplasia) categories. The sensitivity and specificity performance for

this algorithm was 85% and 78%, respectively. Chapter 5 presents a quantitative

combinatorial method that incorporates HRME data with wide field autofluorescence

imaging data into a classification algorithm, to demonstrate how different imaging

modalities, providing fundamentally different information. Various combination methods

are used to train and validate the classification algorithm, which used both a linear

discriminant analysis as well as a classification tree method. The best-performing

combinatorial method, which involved weighting the contributions from both systems,

yielded a performance gain of better than 10% over the performance of any one system

alone.

Chapter 6 demonstrates that the HRME system can be used on a distinctly

different tissue type. Barrett's metaplasia involves the transformation of the normal

squamous epithelium of the esophagus to a glandular, intestinal type. This change is not

neoplastic in itself, but malignant transformation can occur in a small fraction of cases.

HRME images of this glandular tissue is able to reveal the presence of large, intact glands

in non-neoplastic cases, while neoplastic tissue clearly shows disrupted, overlapping

glands, or loss of glandular structure altogether. Quantitative image analysis, presented in

Chapter 7 and using the same feature analysis tools introduced in Chapter 4, can also

successfully classify images as neoplastic or non-neoplastic. A study of *ex vivo*

esophageal tissue from 9 patients, comprised of 128 independent pathology-confirmed measurement sites yielded a classification performance of 87% sensitivity and 85% specificity.

8.2 Implications

High-resolution imaging for cancer diagnostic applications is an emerging field that has benefitted significantly from recent advances in fiber optic, computer, and microelectromechanical systems (MEMS). Sophisticated endomicroscopy systems allow imaging of epithelial tissue in organ systems that are not readily available, such as the bronchi, esophagus, and colon[31, 32, 100, 101]. These "optical biopsy' techniques yield important structural information at subcellular resolution that was typically only obtained with histopathology and physical removal of the tissue. This is of particular importance in gastrointestinal imaging, where the tissue epithelium is only accessible through a specialized endoscopy system. Providing feedback during such endoscopy procedures could help guide therapeutic applications.

While high-resolution imaging systems have been miniaturized as to directly access the oral cavity, or directly integrated into endoscopy systems, complex scanning electronics and laser illumination systems remain expensive. The development of the HRME presented in this dissertation was motivated by the need to reduce costs and improve reliability so such technology could be more easily disseminated to regions with less sophisticated infrastructure. While this system sacrifices lateral resolution and axial sectioning, as is possible in systems with confocal capabilities, image quality is sufficient to discriminate between clinically significant disease states. Using an appropriate

fluorescence contrast agent that is responsive to changes that occur in dysplasia is essential. Proflavine, a DNA-intercalating dye that crosses the cell membrane without the need for any specialized buffer solutions, yields excellent nuclear contrast. Since many of the hallmark structural changes that occur in dysplasia are visible in the nucleus, proflavine is an ideal contrast agent complement to the HRME system.

Since the images taken by the HRME are digitally stored, quantitative image processing and analysis techniques were of great importance in these studies. Analyses of textural features in the images were of particular use in distinguishing between neoplastic and non-neoplastic measurement sites. This is due in large part to the nuclear localization of the proflavine molecule; since dysplastic changes tend to occur in cell nuclei, and the majority of the fluorescence emission light collected by the HRME was from nuclear-localized proflavine, text image analysis is a logical means to differentiate between these two states. Difficulties in this technique arise when proflavine is sequestered in regions of the epithelium that do not contain cell nuclei, such as a thick keratin layer on the surface of the tissue.

Of particular interest in this study is the use of the HRME device and image classification techniques to study different tissue types- squamous mucosa (oral squamous cancer studies) and columnar mucosa (Barrett's neoplasia studies). Dysplasia of squamous mucosa is characterized by increasing nuclear crowding and nuclear atypia, while dysplasia in columnar epithelium is characterized by crowded and disrupted gland structure. Although the same image features were not selected by the classification algorithm code, textural features again played a large role. The ability to use the same

device and computer-based classification tools in both tissue types demonstrates the flexibility of the technique and its potential as an optical diagnostic tool.

8.3 Future Work

In order to increase the flexibility of the HRME device, and to further explore high-resolution imaging with molecular-specific contrast agents, coupling an additional light source to the system is a logical future project. The blue LED module that is currently used could be retained to enable the continued use of proflavine, perhaps as a nuclear counterstain, but its wide bandwidth would require the additional light source to be in the red region of the spectrum. Reduced cost and portability were original design considerations for the HRME; the availability, low cost, and low power requirements of laser diodes makes them an ideal choice. Organic dyes, such as Alexa-647 (Invitrogen, Carlsbad, CA) have been shown to be easily conjugated to monoclonal antibodies, enabling HRME imaging of cell surface markers with molecular specificity. A laser module with a 633nm line would be capable of exciting this Alexa-647 fluorophore; an appropriate dichroic mirror and long pass filter could be placed as a secondary detection arm in the existing HRME system, while replacing the folding mirror with a dichroic with long-wavelength transmission in the current detection arm.

Due to the promising results of the quantitative oral mucosa and Barrett's metaplasia projects, it would be interesting to perform similar analyses on various other human epithelial tissue. Bronchial tissue, the biliary tree, and other lumenal organs are other important sites that the HRME could image. However, due to the location in the body, reaching some of these sites may prove difficult, though current bronchoscopy and

ERCP systems may offer a means of introducing the fiber optic probe to the regions to be imaged.

As previously mentioned, image artifacts are introduced when non-specific binding of the proflavine contrast agent occurs. Proflavine has some affinity for keratin and collagen, for example, with the former being present in a large subset or oral lesions. To overcome this effect, it would be beneficial for the fiber optic probe to be *mechanically coupled to a hypodermic needle device. While a simple version of this was* demonstrated in Chapter 3 on a murine model, a smaller and more precise system could be developed for human oral epithelium. Beveling the end of the image guide may prove useful for mechanically penetrating tissue, though this would come at a cost of some lateral resolution.

Another significant future project for the HRME device is to collect a large validation set for both of the quantitative imaging studies presented here. These larger-scale studies could benefit from distributing several HRME devices to multiple centers. In addition, recent approval by the Food and Drug Administration of an Investigational New Drug application for proflavine enables the possibility of collected this validation set on *in vivo* tissue. This information would be of great importance in establishing the HRME technology as a useful diagnostic screening tool.

8.4 Conclusion

This dissertation has demonstrated the use of a simple and robust fiber bundle image guide based microendoscopy system. This microendoscope was validated using non-biologic targets as well as in vitro cell culture, including a demonstration of

molecular-specific labeling. The device was also used in small animal and human tissue studies. A quantitative classification algorithm was developed that demonstrating the ability of the device to objectively differentiate between non-neoplastic tissue and clinically significant disease. This technology has the potential to be distributed to a wide range of medical settings, and not limited to tertiary-care centers. Widespread use of the HRME system as a complement to existing screening techniques, or as an intra-operative margin detection tool should aid in earlier detection of neoplastic change in precancerous lesions of human epithelial tissue, improving the number of tissue-sparing treatment modalities and reducing associated morbidity.

References

1.   www.cancer.org. Cancer Facts and Figures 2006. 2006.

2.   www.cancer.org. Surveillance Epidemiology and End Results. 2006.

3.   Robbins S. Robbins Pathologic Basis of Disease. Philadelphia: W.B. Saunders; 1999.

4.   Schaefer NG, Pestalozzi BC, Knuth A, Renner C. Potential use of humanized antibodies in the treatment of breast cancer. Expert Rev Anticancer Ther 2006;6: 1065-74.

5.   Farokhzad OC, Jon S, Khademhosseini A, Tran TN, Lavan DA, Langer R. Nanoparticle-aptamer bioconjugates: a new approach for targeting prostate cancer cells. Cancer Res 2004;64: 7668-72.

6.   LeBlanc JK, Ciaccia D, Al-Assi MT, *et al.* Optimal number of EUS-guided fine needle passes needed to obtain a correct diagnosis. Gastrointest Endosc 2004;59: 475-81.

7.   Erickson RA, Sayage-Rabie L, Beissner RS. Factors predicting the number of EUS-guided fine-needle passes for diagnosis of pancreatic malignancies. Gastrointest Endosc 2000;51: 184-90.

8.   Wu TT, Qu JNY, Cheung TH, Yim SF, Wong YF. Study of dynamic process of acetic acid induced-whitening in epithelial tissues at cellular level. Optics Express 2005;13: 4963-73.

9.   Martin IC, Kerawala CJ, Reed M. The application of toluidine blue as a diagnostic adjunct in the detection of epithelial dysplasia. Oral Surg Oral Med Oral Pathol Oral Radiol Endod 1998;85: 444-6.

10.	D'Ilario L, Martinelli A. Toluidine blue: aggregation properties and structural aspects. Modelling and Simulation in Materials Science and Engineering 2006;14: 581-95.

11.	Zhang L, Williams M, Poh CF, *et al*. Toluidine blue staining identifies high-risk primary oral premalignant lesions with poor outcome. Cancer Res 2005;65: 8017-21.

12.	Epstein JB, Scully C, Spinelli J. Toluidine blue and Lugol's iodine application in the assessment of oral malignant disease and lesions at risk of malignancy. J Oral Pathol Med 1992;21: 160-3.

13.	Greene GW, Jr. Proceedings: Detection and diagnosis of oral malignancies. J Surg Oncol 1974;6: 277-92.

14.	Reddy CR, Ramulu C, Sundareshwar B, Raju MV, Gopal R, Sarma R. Toluidine blue staining of oral cancer and precancerous lesions. Indian J Med Res 1973;61: 1161-4.

15.	Rosenberg D, Cretin S. Use of meta-analysis to evaluate tolonium chloride in oral cancer screening. Oral Surg Oral Med Oral Pathol 1989;67: 621-7.

16.	Silverman S, Jr., Migliorati C. Toluidine blue staining and early detection of oral precancerous and malignant lesions. Iowa Dent J 1992;78: 15-6.

17.	Handlers JP. Diagnosis and management of oral soft-tissue lesions: the use of biopsy, toluidine blue staining, and brush biopsy. J Calif Dent Assoc 2001;29: 602-6.

18.	Bornhop DJ, Contag CH, Licha K, Murphy CJ. Advance in contrast agents, reporters, and detection. Journal of Biomedical Optics 2001;6: 106-10.

19.	Onofre MA, Sposto MR, Navarro CM. Reliability of toluidine blue application in the detection of oral epithelial dysplasia and in situ and invasive squamous cell carcinomas. Oral Surg Oral Med Oral Pathol Oral Radiol Endod 2001;91: 535-40.

20.	Peitz U, Malfertheiner P. Chromoendoscopy: from a research tool to clinical progress. Dig Dis 2002;20: 111-9.

21.   Amano Y, Kushiyama Y, Ishihara S, *et al.* Crystal violet chromoendoscopy with mucosal pit pattern diagnosis is useful for surveillance of short-segment Barrett's esophagus. Am J Gastroenterol 2005;100: 21-6.

22.   Theodossiou T, Hothersall JS, Woods EA, Okkenhaug K, Jacobson J, MacRobert AJ. Firefly luciferin-activated rose bengal: in vitro photodynamic therapy by intracellular chemiluminescence in transgenic NIH 3T3 cells. Cancer Res 2003;63: 1818-21.

23.   Duncan MB, Horwhat JD, Maydonovitch CL, *et al.* Use of methylene blue for detection of specialized intestinal metaplasia in GERD patients presenting for screening upper endoscopy. Dig Dis Sci 2005;50: 389-93.

24.   Zhu X, Zhang SH, Zhang KH, Li BM, Chen J. Value of endoscopic methylene blue and Lugol's iodine double staining and detection of GST-Pi and telomerase in the early diagnosis of esophageal carcinoma. World J Gastroenterol 2005;11: 6090-5.

25.   Kallakury BV, Karikehalli S, Haholu A, Sheehan CE, Azumi N, Ross JS. Increased expression of matrix metalloproteinases 2 and 9 and tissue inhibitors of metalloproteinases 1 and 2 correlate with poor prognostic variables in renal cell carcinoma. Clin Cancer Res 2001;7: 3113-9.

26.   Aaron..J CT, Park SY, Coghlan L, Follen M, Richards-Kortum R, Sokolov K. Plasmon Resonance Coupling of Metal Nanoparticles for Molecular Imaging of Carcinogenesis In Vivo. Nat Med 2005.

27.   Helmchen F, Denk W. Deep tissue two-photon microscopy. Nat Methods 2005;2: 932-40.

28.   Laemmel E, Genet M, Le Goualher G, Perchant A, Le Gargasson JF, Vicaut E. Fibered confocal fluorescence microscopy (Cell-viZio) facilitates extended imaging in the field of microcirculation. A comparison with intravital microscopy. J Vasc Res 2004;41: 400-11.

29.   Flusberg BA, Cocker ED, Piyawattanametha W, Jung JC, Cheung ELM, Schnitzer MJ. Fiber-optic fluorescence imaging. Nature Methods 2005;2: 941-50.

30.   Lichtman JW, Conchello JA. Fluorescence microscopy. Nat Methods 2005;2: 910-9.

31.   Polglase AL, McLaren WJ, Delaney PM. Pentax confocal endomicroscope: a novel imaging device for in vivo histology of the upper and lower gastrointestinal tract. Expert Rev Med Devices 2006;3: 549-56.

32.   Kiesslich R, Burg J, Vieth M, et al. Confocal laser endoscopy for diagnosing intraepithelial neoplasias and colorectal cancer in vivo. Gastroenterology 2004;127: 706-13.

33.   Michalet X, Pinaud FF, Bentolila LA, et al. Quantum dots for live cells, in vivo imaging, and diagnostics. Science 2005;307: 538-44.

34.   Akerman ME, Chan WC, Laakkonen P, Bhatia SN, Ruoslahti E. Nanocrystal targeting in vivo. Proc Natl Acad Sci U S A 2002;99: 12617-21.

35.   Gao X, Cui Y, Levenson RM, Chung LW, Nie S. In vivo cancer targeting and imaging with semiconductor quantum dots. Nat Biotechnol 2004;22: 969-76.

36.   Voura EB, Jaiswal JK, Mattoussi H, Simon SM. Tracking metastatic tumor cell extravasation with quantum dot nanocrystals and fluorescence emission-scanning microscopy. Nat Med 2004;10: 993-8.

37.   Ballou B, Lagerholm BC, Ernst LA, Bruchez MP, Waggoner AS. Noninvasive imaging of quantum dots in mice. Bioconjug Chem 2004;15: 79-86.

38.   Wu X, Liu H, Liu J, et al. Immunofluorescent labeling of cancer marker Her2 and other cellular targets with semiconductor quantum dots. Nat Biotechnol 2003;21: 41-6.

39.   Josephson L, Kircher MF, Mahmood U, Tang Y, Weissleder R. Near-infrared fluorescent nanoparticles as combined MR/optical imaging probes. Bioconjug Chem 2002;13: 554-60.

40.   Brockhoff G, Heiss P, Schlegel J, Hofstaedter F, Knuechel R. Epidermal growth factor receptor, c-erbB2 and c-erbB3 receptor interaction, and related cell cycle kinetics of SK-BR-3 and BT474 breast carcinoma cells. Cytometry 2001;44: 338-48.

41.   Conchello JA, Lichtman JW. Optical sectioning microscopy. Nat Methods 2005;2: 920-31.

42.   Collier T, Lacy A, Richards-Kortum R, Malpica A, Follen M. Near Real-Time Confocal Microscopy of Amelanotic Tissue: Detection of Dysplasia in ex Vivo Cervical Tissue. Acad Radiol 2002;9: 504-12.

43.   Collier T, Follen M, Malpica A, Richards-Kortum R. Sources of scattering in cervical tissue: determination of the scattering coefficient by confocal microscopy. Appl Opt 2005;44: 2072-81.

44.   Kiesslich R, Goetz M, Burg J, et al. Diagnosing Helicobacter pylori in vivo by confocal laser endoscopy. Gastroenterology 2005;128: 2119-23.

45.   Beechey-Newman N, Kulkarni D, Kothari A, et al. Breast duct microendoscopy in nipple discharge: microbrush improves cytology. Surg Endosc 2005;19: 1648-51.

46.   Jung JC, Mehta AD, Aksay E, Stepnoski R, Schnitzer MJ. In vivo mammalian brain imaging using one- and two-photon fluorescence microendoscopy. J Neurophysiol 2004;92: 3121-33.

47.   Hirano M, Yamashita Y, Miyakawa A. In vivo visualization of hippocampal cells and dynamics of Ca2+ concentration during anoxia: feasibility of a fiber-optic plate microscope system for in vivo experiments. Brain Res 1996;732: 61-8.

48.   Monfared A, Blevins NH, Cheung EL, Jung JC, Popelka G, Schnitzer MJ. In vivo imaging of mammalian cochlear blood flow using fluorescence microendoscopy. Otol Neurotol 2006;27: 144-52.

49.   Levene MJ, Dombeck DA, Kasischke KA, Molloy RP, Webb WW. In vivo multiphoton microscopy of deep brain tissue. J Neurophysiol 2004;91: 1908-12.

50.   Poe GR, Rector DM, Harper RM. Hippocampal reflected optical patterns during sleep and waking states in the freely behaving cat. J Neurosci 1994;14: 2933-42.

51.   J.D. Kraus DAF. Electromagnetics with Applications. Singapore: McGraw-Hill; 1999.

52.   White DJ, Stoddart PR. Nanostructured optical fiber with surface-enhanced Raman scattering functionality. Optics Letters 2005;30: 598-600.

53.   Sumetsky M. How thin can a microfiber be and still guide light? Optics Letters 2006;31.

54.   Y. Chigusa KF, Y. Hattori, Y. Matsuda. Properties of silica glass image fiber and its application. Optoelectronics 1986;1: 203-16.

55.   Chovin A, Garrigue P, Vinatier P, Sojic N. Development of an ordered array of optoelectrochemical individually readable sensors with submicrometer dimensions: Application to remote electrochemiluminescence imaging. Analytical Chemistry 2004;76: 357-64.

56.   Iizuka K. Engineering Optics. Berlin: Springer-Verlag; 1985.

57.   Utzinger U, Richards-Kortum RR. Fiber optic probes for biomedical optical spectroscopy. Journal of Biomedical Optics 2003;8: 121-47.

58.   Ghaemi HF, Li Y, Thio T, Wang T. Fiber image guide with subwavelength resolution. Applied Physics Letters 1998;72: 1137-9.

59.   Gmitro AF, Aziz DJ. Confocal Microscopy through a Fiber-Optic Imaging Bundle. Optics Letters 1993;18: 565-7.

60.   A. Gmitro AR, A. Kano. In vivo fluorescence confocal microendoscopy. IEEE 2002: 277-9.

61.   Weissleder R, Tung CH, Mahmood U, Bogdanov A, Jr. In vivo imaging of tumors with protease-activated near-infrared fluorescent probes. Nat Biotechnol 1999;17: 375-8.

62.   Ke S, Wen X, Gurfinkel M, et al. Near-infrared optical imaging of epidermal growth factor receptor in breast cancer xenografts. Cancer Res 2003;63: 7870-5.

63.   Becker A, Hessenius C, Licha K, et al. Receptor-targeted optical imaging of tumors with near-infrared fluorescent ligands. Nat Biotechnol 2001;19: 327-31.

64.   Jaffer FA, Weissleder R. Molecular imaging in the clinical arena. JAMA 2005;293: 855-62.

65.   Massoud TF, Gambhir SS. Integrating noninvasive molecular imaging into molecular medicine: an evolving paradigm. Trends Mol Med 2007;13: 183-91.

66.   Kimura S, Wilson T. Confocal Scanning Optical Microscope using Single-Mode Fiber for Signal Detection. Applied Optics 1991;30: 2143-50.

67.   Giniunas L, Juškaitis R, Shatalin SV. Scanning Fibre-Optic Microscope. Electronics Letters 1991;27: 724-6.

68.   Delaney PM, Harris MR, King RG. Fiberoptic Laser-Scanning Confocal Microscope Suitable for Fluorescence Imaging. Applied Optics 1994;33: 573-7.

69.   Dickensheets DL, Kino GS. Micromachined scanning confocal optical microscope. Optics Letters 1996;21: 764-6.

70.   Liu JTC, Mandella MJ, Ra H, et al. Miniature near-infrared dual-axes confocal microscope utilizing a two-dimensional microelectromechanical systems scanner. Optics Letters 2007;32: 256-8.

71.   Shin HJ, Pierce MC, Lee D, Ra H, Solgaard O, Richards-Kortum R. Fiber-optic confocal microscope using a MEMS scanner and miniature objective lens. Optics Express 2007;15: 9113-22.

72.   Seibel E, Smithwick Q. Unique features of scanning fiber optical endoscopy. Annals of Biomedical Engineering 2000;28: S-40.

73.   Yelin D, Rizvi I, White WM, *et al.* Three-dimensional miniature endoscopy. Nature 2006;443: 765.

74.   Harris MR,UK Patent; GB 2 340 332 B. UK. 2001.

75.   Polglase AL, McLaren WJ, Skinner SA, Kiesslich R, Neurath MF, Delaney PM. A fluorescence confocal endomicroscope for in vivo microscopy of the upper- and the lower-GI tract. Gastrointest Endosc 2005;62: 686-95.

76.   Kiesslich R, Goetz M, Vieth M, Galle PR, Neurath MF. Technology insight: confocal laser endoscopy for in vivo diagnosis of colorectal cancer. Nat Clin Pract Oncol 2007;4: 480-90.

77.   Juskaitis R, Wilson T, Watson TF. Real-time white light reflection confocal microsocpy using a fiber-optic bundle. Scanning 1997;19: 15-9.

78.   Liang C, Descour MR, Sung KB, Richards-Kortum R. Fiber confocal reflectance microscope (FCRM) for in-vivo imaging. Optics Express 2001;9: 821-30.

79.   Dubaj V, Mazzolini A, Wood A, Harris M. Optic fibre bundle contact imaging probe employing a laser scanning confocal microscope. J Microsc 2002;207: 108-17.

80.   Jean F, Bourg-Heckly G, Viellerobe B. Fibered confocal spectroscopy and multicolor imaging system for in vivo fluorescence analysis. Optics Express 2007;15: 4008-17.

81.   Sabharwal YS, Rouse AR, Donaldson L, Hopkins MF, Gmitro AF. Slit-Scanning Confocal Microendoscope for High-Resolution *In Vivo* Imaging. Applied Optics 1999;38: 7133-44.

82.   Rouse AR, Gmitro AF. Multispectral imaging with a confocal microendoscope. Optics Letters 2000;25: 1708-10.

83.   Delaney PM, Harris MR. Fiber Optics in Confocal Microscope. In: Pawley JB, editor. Handbook of Confocal Microscopy. 2nd ed. New York: Plenum Press; 1995. p. 515-23.

84.   Steinman RR. Pharmacologic control of dentinal fluid movement and dental caries in rats. J Dent Res 1968;47: 720-4.

85.   Collier T, Guillaud M, Follen M, Malpica A, Richards-Kortum R. Real-time reflectance confocal microscopy: comparison of two-dimensional images and three-dimensional image stacks for detection of cervical precancer. J Biomed Opt 2007;12: 024021.

86.   Sung KB, Richards-Kortum R, Follen M, Malpica A, Liang C, Descour MR. Fiber optic confocal reflectance microscopy: a new real-time technique to view nuclear morphology in cervical squamous epithelium in vivo. Optics Express 2003;11: 3171-81.

87.   Rouse AR, Kano A, Udovich JA, Kroto SM, Gmitro AF. Design and demonstration of a miniature catheter for a confocal microendoscope. Applied Optics 2004;43: 5763-71.

88.   Ferlay J, Bray F, Pisani P, Parkin DM. GLOBOCAN 2002: cancer incidence, mortality and prevalence worldwide: IARC Press, Lyon; 2004.

89.   Moore SR, Johnson NW, Pierce AM, Wilson DF. The epidemiology of mouth cancer: A review of global incidence. Oral Dis 2000;6: 65-74.

90.   Blair EA, Callender DL. Head and neck cancer. The problem. Clin Plast Surg 1994;21: 1-7.

91.   Georgakoudi I, Jacobson BC, Muller MG, et al. NAD(P)H and collagen as in vivo quantitative fluorescent biomarkers of epithelial precancerous changes. Cancer Res 2002;62: 682-7.

92.   Bouma BE, Tearney GJ. Clinical imaging with optical coherence tomography. Acad Radiol 2002;9: 942-53.

93.   Lane PM, Gilhuly T, Whitehead P, *et al.* Simple device for the direct visualization of oral-cavity tissue fluorescence. J Biomed Opt 2006;11: 024006.

94.   Roblyer D, Richards-Kortum R, Kurachi C, *et al.* A multispectral optical imaging device for in vivo detection of oral neoplasia. Journal of Biomedical Optics 2008;in press.

95.   Nori S, Rius-Diaz F, Cuevas J, *et al.* Sensitivity and specificity of reflectance-mode confocal microscopy for in vivo diagnosis of basal cell carcinoma: a multicenter study. J Am Acad Dermatol 2004;51: 923-30.

96.   Rajadhyaksha M, Anderson RR, Webb RH. Video-rate Confocal Scanning Laser Microscope for Imaging Human Tissues In Vivo. Applied Optics 1999;38: 2105-15.

97.   White WM, Rajadhyaksha M, Gonzalez S, Fabian RL, Anderson RR. Noninvasive Imaging of Human Oral Mucosa *In Vivo* by Confocal Reflectance Microscopy. Laryngoscope 1999;109: 1709-17.

98.   Clark A, Collier T, Lacy A, *et al.* Detection of dysplasia with near real time confocal microscopy. Biomed Sci Instrum 2002;38: 393-8.

99.   Thong PSP, Olivo M, Kho KW, *et al.* Laser confocal endomicroscopy as a novel technique for fluorescence diagnostic imaging of the oral cavity. Journal of Biomedical Optics 2007;12: -.

100.   Becker V, Vieth M, Bajbouj M, Schmid RM, Meining A. Confocal laser scanning fluorescence microscopy for in vivo determination of microvessel density in Barrett's esophagus. Endoscopy 2008;40: 888-91.

101.   Thiberville L, Moreno-Swirc S, Vercauteren T, Peltier E, Cave C, Heckly GB. In vivo imaging of the bronchial wall microstructure using fibered confocal fluorescence microscopy. American Journal of Respiratory and Critical Care Medicine 2007;175: 22-31.

102. Muldoon T, Pierce MC, Nida D, Williams MD, Gillenwater A, Richards-Kortum R. Subcellular resolution molecular imaging within living tissue by fiber microendoscopy. Optics Express 2007;15: 16413-23.

103. Muldoon TJ, Anandasabapathy S, Maru D, Richards-Kortum R. High-Resolution Imaging in Barrett's Esophagus: A Novel, Low- Cost Endoscopic Microscope Gastrointest Endosc 2008;in press.

104. Ferguson LR, Denny WA. Genotoxicity of non-covalent interactions: DNA intercalators. Mutation Research-Fundamental and Molecular Mechanisms of Mutagenesis 2007;623: 14-23.

105. Ulitzur S, Weiser I. Acridine dyes and other DNA-intercalating agents induce the luminescence system of luminous bacteria and their dark variants. Proc Natl Acad Sci U S A 1981;78: 3338-42.

106. Janssen PA, Selwood BL, Dobson SR, Peacock D, Thiessen PN. To dye or not to dye: a randomized, clinical trial of a triple dye/alcohol regime versus dry cord care. Pediatrics 2003;111: 15-20.

107. Polglase AL, McLaren WJ, Skinner SA, Kiesslich R, Neurath MF, Delaney PM. A fluorescence confocal endomicroscope for in vivo microscopy of the upper- and the lower-GI tract. Gastrointest Endosc 2005;62: 686-95.

108. Argenti F, Alparone L, Benelli G. Fast Algorithms for Texture Analysis Using Cooccurrence Matrices. Iee Proceedings-F Radar and Signal Processing 1990;137: 443-8.

109. Gossage KW, Tkaczyk TS, Rodriguez JJ, Barton JK. Texture, analysis of optical coherence tomography images: feasibility for tissue classification. Journal of Biomedical Optics 2003;8: 570-5.

110. Srivastava S, Rodriguez JJ, Rouse AR, Brewer MA, Gmitro AF. Computer-aided identification of ovarian cancer in confocal microendoscope images. J Biomed Opt 2008;13: 024021.

111. Lingley-Papadopoulos CA, Loew MH, Manyak MJ, Zara JM. Computer recognition of cancer in the urinary bladder using optical coherence tomography and texture analysis. Journal of Biomedical Optics 2008;13: -.

112. Breiman L, Friedman, J. H., Olshen, R. A., and Stone, C. J. Classification and Regression Trees. Belmont, California: Wadsworth International Group; 1984.

113. Dwyer PJ, DiMarzio CA, Rajadhyaksha M. Confocal theta line-scanning microscope for imaging human tissues. Applied Optics 2007;46: 1843-51.

114. Carlson K, Chidley M, Sung KB, *et al.* In vivo fiber-optic confocal reflectance microscope with an injection-molded plastic miniature objective lens. Appl Opt 2005;44: 1792-7.

115. Sutton DN, Brown JS, Rogers SN, Vaughan ED, Woolgar JA. The prognostic implications of the surgical margin in oral squamous cell carcinoma. Int J Oral Maxillofac Surg 2003;32: 30-4.

116. Ord RA, Aisner S. Accuracy of frozen sections in assessing margins in oral cancer resection. J Oral Maxillofac Surg 1997;55: 663-9; discussion 9-71.

117. Patel YG, Nehal KS, Aranda I, Li YB, Halpern AC, Rajadhyaksha M. Confocal reflectance mosaicing of basal cell carcinomas in Mohs surgical skin excisions. Journal of Biomedical Optics 2007;12: -.

118. Pavlova I, Williams M, El-Naggar A, Richards-Kortum R, Gillenwater A. Understanding the biological basis of autofluorescence imaging for oral cancer detection: High-resolution fluorescence microscopy in viable tissue. Clinical Cancer Research 2008;14: 2396-404.

119. Society AC. *Cancer Facts & Figures 2008*. Atlanta: American Cancer Society; 2008.

120. Poh CF, Ng SP, Williams PM, *et al.* Direct fluorescence visualization of clinically occult high-risk oral premalignant disease using a simple hand-held device. Head & neck 2007;29: 71-6.

121. Pavlova I, Williams M, El-Naggar A, Richards-Kortum R, Gillenwater A. Understanding the biological basis of autofluorescence imaging for oral cancer detection: high-resolution fluorescence microscopy in viable tissue. Clin Cancer Res 2008;14: 2396-404.

122. Roblyer D, Kurachi C, Stepanek V, *et al.* Objective Detection and Delineation of Oral Neoplasia Using Autofluorescence Imaging. Cancer Prevention Research 2009;in press.

123. Tearney GJ, Brezinski ME, Bouma BE, *et al. In Vivo* Endoscopic Optical Biopsy with Optical Coherence Tomography. Science 1997;276: 2037-9.

124. Roblyer D, Kurachi C, Stepanek V, *et al.* Computer Aided Diagnosis of Oral Cancer and Precancer Using Multispectral Widefield Optical Imaging. IEEE Trans Med Imaging 2009 planned submission.

125. Albert A, Harris EK. Multivariate interpretation of clinical laboratory data. New York: Marcel Dekker inc.; 1987.

126. Benediktsson JA, Sveinsson JR, Swain PH. Hybrid consensus theoretic classification. Ieee Transactions on Geoscience and Remote Sensing 1997;35: 833-43.

127. Williamson WA, Ellis FH, Jr., Gibb SP, *et al.* Barrett's esophagus. Prevalence and incidence of adenocarcinoma. Arch Intern Med 1991;151: 2212-6.

128. DeVault KR. Epidemiology and significance of Barrett's esophagus. Dig Dis 2000;18: 195-202.

129. Cameron AJ. Epidemiology of Barrett's esophagus and adenocarcinoma. Dis Esophagus 2002;15: 106-8.

130. Thomson BNJ, Cade RJ. Oesophagectomy for early adenocarcinoma and dysplasia arising in Barrett's oesophagus. Anz Journal of Surgery 2003;73: 121-4.

131. Dellon ES, Shaheen NJ. Does screening for Barrett's esophagus and adenocarcinoma of the esophagus prolong survival? Journal of Clinical Oncology 2005;23: 4478-82.

132. van Sandick JW, van Lanschot JJB, Kuiken BW, Tytgat GNJ, Offerhaus GJA, Obertop H. Impact of endoscopic biopsy surveillance of Barrett's oesophagus on pathological stage and clinical outcome of Barrett's carcinoma. Gut 1998;43: 216-22.

133. Egger K, Werner M, Meining A, et al. Biopsy surveillance is still necessary in patients with Barrett's oesophagus despite new endoscopic imaging techniques. Gut 2003;52: 18-23.

134. Curvers WL, Wong LM, Song K, et al. Endoscopic tri-modal imaging (ETMI) for the detection of dysplastic lesions in Barrett's Esophagus. Gastroenterology 2006;130: A642-a.

135. Kara M, DaCosta RS, Wilson BC, Marcon NE, Bergman J. Autofluorescence-based detection of early neoplasia in patients with Barrett's esophagus. Digestive Diseases 2004;22: 134-41.

136. Kara M, Ennahachi M, Fockens P, Peters F, ten Kate F, Bergman J. Narrow-band imaging (NBI) in Barrett's esophagus (BE): What features are relevant for the detection of high-grade dysplasia (HGD) and early cancer (EC)? Gastroenterology 2004;126: A50-a.

137. Hamamoto Y, Endo T, Nosho K, Arimura Y, Sato M, Imai K. Usefulness of narrow-band imaging endoscopy for diagnosis of Barrett's esophagus. J Gastroenterol 2004;39: 14-20.

138. Ross AS, Noffsinger A, Waxman I. Narrow band imaging directed EMR for Barrett's esophagus with high-grade dysplasia. Gastrointest Endosc 2007;65: 166-9.

139. Niepsuj K, Niepsuj G, Cebula W, et al. Autofluorescence endoscopy for detection of high-grade dysplasia in short-segment Barrett's esophagus. Gastrointest Endosc 2003;58: 715-9.

140. Yoshida S, Tanaka S, Hirata M, *et al.* Optical biopsy of GI lesions by reflectance-type laser-scanning confocal microscopy. Gastrointest Endosc 2007;66: 144-9.

141. Kiesslich R, Gossner L, Goetz M, *et al.* In vivo histology of Barrett's esophagus and associated neoplasia by confocal laser endomicroscopy. Clin Gastroenterol Hepatol 2006;4: 979-87.

142. Inoue H, Cho JY, Satodate H, *et al.* Development of Virtual Histology and Virtual Biopsy Using Laser-scanning Confocal Microscopy. Scandinavian Journal of Gastroenterology 2003;38: 37 - 9.

143. Pitten FA, Kramer A. Antimicrobial efficacy of antiseptic mouthrinse solutions. Eur J Clin Pharmacol 1999;55: 95-100.

144. Mathe G. The failure of HAART to cure the HIV-1/AIDS complex. Suggestions to add integrase inhibitors as complementary virostatics, and to replace their continuous long combination applications by short sequences differing by drug rotations. Biomed Pharmacother 2001;55: 295-300.

145. Pohl H, Welch HG. The role of overdiagnosis and reclassification in the marked increase of esophageal adenocarcinoma incidence. J Natl Cancer Inst 2005;97: 142-6.

146. Portale G, Hagen JA, Peters JH, *et al.* Modern 5-year survival of resectable esophageal adenocarcinoma: single institution experience with 263 patients. J Am Coll Surg 2006;202: 588-96; discussion 96-8.

147. Curvers WL, Bergman JJ. Multimodality imaging in Barrett's esophagus: looking longer, seeing better, and recognizing more. Gastroenterology 2008;135: 297-9.

148. Borovicka J, Fischer J, Neuweiler J, *et al.* Autofluorescence endoscopy in surveillance of Barrett's esophagus: a multicenter randomized trial on diagnostic efficacy. Endoscopy 2006;38: 867-72.

149. Kato M, Kaise M, Yonezawa J, Yoshida Y, Tajiri H. Autofluorescence endoscopy versus conventional white light endoscopy for the detection of superficial gastric neoplasia: a prospective comparative study. Endoscopy 2007;39: 937-41.

150. Wong Kee Song L-M, Wilson BC. Optical Detection of High-Grade Dysplasia in Barrett's Esophagus. Techniques in Gastrointestinal Endoscopy 2005;7: 78-88.

151. Vieth M, Kiesslich R. Distinction of high-grade intraepithelial neoplasia and invasive Barrett's adenocarcinoma. Esophagus 2006;3: 171-6.

152. Guo YT, Li YQ, Yu T, *et al.* Diagnosis of gastric intestinal metaplasia with confocal laser endomicroscopy in vivo: a prospective study. Endoscopy 2008;40: 547-53.

153. Kiesslich R, Anagnostopoulos GK, Axon A, *et al.* Interobserver Variation and Standardized Training for Confocal Laser Endomicroscopy Image Interpretation in the Upper and Lower GI Tract. Gastrointest Endosc 2007;65: AB354-AB.

154. Wang VS, Hornick JL, Sepulveda JA, Mauer R, Poneros JM. Low prevalence of submucosal invasive carcinoma at esophagectomy for high-grade dysplasia or intramucosal adenocarcinoma in Barrett's esophagus: a 20-year experience. Gastrointest Endosc 2009.

155. Kiesslich R, Goetz M, Lammersdorf K, *et al.* Chromoscopy-guided endomicroscopy increases the diagnostic yield of intraepithelial neoplasia in ulcerative colitis. Gastroenterology 2007;132: 874-82.